Polymeric Photonic Crystals

by

Yoel Fink

B.Sc. Chemical Engineering, B. A. Physics
Israel Institute of Technology 1994
Submitted to the Department of Materials Science and Engineering
in Partial Fulfillment of the Requirements for the Degree of

Doctor of Philosophy in Materials Science
at the
MASSACHUSETTS INSTITUTE OF TECHNOLOGY
February 2000

Signature of Author...
Department of Materials Science and Engineering
January 7, 2000

Certified by...
Edwin L. Thomas
Morris Cohen Professor of Materials Science and Engineering
Thesis Supervisor

Certified by...
John D. Joannopoulos
Francis Wright Davis Professor of Physics
Thesis Supervisor

Certified by...
Chiping Chen
Principal Research Scientist
Thesis Supervisor

Accepted by...
Linn W. Hobbs
Professor of Materials Science
Chair, Departmental Committee on Graduate Students

Polymeric Photonic Crystals

by

Yoel Fink

Submitted to the Department of Materials Science and Engineering
on January 7, 2000 in Partial Fulfillment of the Requirements for the Degree of
Doctor of Philosophy in Materials Science
at the
MASSACHUSETTS INSTITUTE OF TECHNOLOGY
February 2000

Abstract

Two novel and practical methods for controlling the propagation of light are presented: First. a design criterion[1] that permits truly omnidirectional reflectivity for all polarizations of incident light over a wide selectable range of frequencies is derived and used in fabricating an all-dielectric omnidirectional reflector consisting of multilayer films. Because the omnidirectionality criterion is general, it can be used to design omnidirectional reflectors in many frequency ranges of interest. Potential uses depend on the geometry of the system. For example, coating of an enclosure will result in an optical cavity. A hollow tube will produce a low-loss, broadband waveguide, planar film could be used as an efficient radiative heat barrier or collector in thermoelectric devices.

A comprehensive framework[2] for creating one, two and three dimensional photonic crystals out of self-assembling block copolymers has been formulated.

In order to form useful band gaps in the visible regime, periodic dielectric structures made of typical block copolymers need to be modified to obtain appropriate characteristic distances and dielectric constants. Moreover, the absorption and defect concentration must also be controlled. This affords the opportunity to tap into the large structural repertoire, the flexibility and intrinsic tunability that these self-assembled block copolymer systems offer.

A block copolymer was used to achieve a self assembled photonic band gap in the visible regime. By swelling the diblock copolymer with lower molecular weight constituents control over the location of the stop band across the visible regime is achieved. One and three-dimensional crystals have been formed by changing the volume fraction of the swelling media. Methods for incorporating defects of prescribed dimensions into the self-assembled structures have been explored leading to the construction of a self assembled microcavity light-emitting device.

Thesis Supervisor: Edwin L. Thomas
Title: Morris Cohen Professor of Materials Science and Engineering
Thesis Supervisor: John D. Joannopoulos
Title: Francis Wright Davis Professor of Physics
Thesis Supervisor: Chiping Chen
Title: Principal Research Scientist

---

[1] Original disclosure date: 1-28-98

[2] Original disclosure date: 2-11-97

Acknowledgment

During my second year as an undergraduate in the department of chemical engineering at the Technion I decided to change my major from Chem E to physics. Professor Ishi Talmon then my academic advisor convinced me not to quit my studies in the Chem E department. He presented me with a research problem, from this initial encounter the FT-CEVS was developed. Prof. Talmon was the first to introduce me to the world of scientific research. I am very grateful to Ishi for the many years of mentoring and friendship.

I would like to express my deep gratitude to Dr. Chiping Chen, for his continuous support, patience, kindness, and generosity. I began working for Chiping in the summer of 95 on a project which involved understanding the dynamics of charged particle beams in periodic solenoidal focussing fields. It was through this project that I first learned about the effects of periodic potentials, Chiping through many patient hours of tutoring and education strengthened my confidence and taught me how to approach problems analytically. Chiping was very supportive of my eventual work on photonic band gap materials and it was his generosity that enabled me to succeed.

It was with Ned that I first started working on the idea of block copolymer self-assembled photonic crystals. Ned has been to me a role model of a great scientist and visionary. He has given me virtually unlimited credit which I probably did not deserve. His early recognition and continuous support made my experience at MIT exciting and stimulating. I thank him greatly for the wonderful time I had at MIT.

My last advisor was Prof. John Joannopoulos, John has influenced my life greatly and I am deeply indebted to him. John is caring and passionate for his work but cares even more for his "kids" the graduate students. He has been to me a teacher, inspiration and a friend.

I feel greatly privileged to have worked for Ishi, Chiping, Ned and John, without them I would not have reached the successful completion of my thesis. They have all contributed to making the experience I had here at MIT one which I will not forget.

I would also like to express my gratitude to my committee member Prof. Moungi Bawendi, who early on generously opened his lab and knowledge to me. Moungi has since been to me a great teacher and a generous human being. I would like to thank my committee member Prof. Lionel Kimerling for his kindness and for his instrumental part in the extraordinary HIDE experience. I would like to thank George Kenney for many interesting discussions and for his important contribution to the success of the HIDE project. I am indebted to many other individuals who have generously provided me with friendship and invaluable advice and time: Dr. Rick Temkin and Prof. Bob Rose who have both advised me on many occasions. Len Radzilowski, Vanessa Chan, Augustine Urbas, Jean DeAngelis, Wing Woo, Catherine Letherdale, Hans Eisler, Josh Winn and Shanhui Fan. Libby Shaw and Tim McClure from the analytical lab many thanks for helping and forgiving all of my mistakes. I wish to thank my office mate Mark Hess for the great time together and many interesting discussions. I would like to thank my wife Zohar for her love and help. My friends, Ori and Limor, Luis and Adriana, Juan-Carlos and Maria-Soledad, Amy and John, Stephane, Ariel and Ronit, Teresa, Ami and Gali. Last I would like to thank my mother and father Irene and Ze'ev and my sisters Elisheva, Efrat, and Miriam, my brothers Michael and Yair.

Table of Contents

List of Figures

List of Tables

Chapter 1: Introduction

In recent years a new class of materials has emerged which holds the promise of controlling the flow of light in matter in novel ways. The optical properties of these materials follow from the Bloch wave solutions to Maxwell's equations in periodic media. Under certain conditions a complete photonic band gap is formed which is a range of electromagnetic frequencies forbidden to exist in the material. Many similarities exist between the electronic band structures of semiconductors and the photonic band structures of PBG materials as well as some striking differences. Understanding the similarities and appreciating the differences between the photonic and electronic interactions allows one to design and optimize structures and fabrication methods for producing novel photonic band gap materials.

The ability to manipulate the propagation of light in materials has been the focus of an intense world wide research effort. The intense activity has generated genuine interest and intriguing results but has yet to impact society, the main reason being the challenging issues related to the formation of complex periodic structures at optical length scales. The consensual fabrication approach today involves the use of lithographic and other semiconductor processing methods or the assembling of colloidal spheres. These approaches are both costly and structurally restrictive and do not utilize the robustness of the photonic band gap to noise and variations in the periodicity.

Many of the interesting properties of photonic band gap materials necessitate the formation of a strong dielectric 'potential' in the material, large spatial variations in the dielectric function increase the width of the photonic gap and its overlap in the Brillouin zone. In the absence of a large contrast, narrow photonic gaps occur near the edges of the

Brillouin zone. The penetration depth of the evanescent 'in gap' modes is inversely related to the width of the band gap. In practice, large dielectric contrast results in stronger confinement and smaller number of structural periods for a given reflectivity value. In strongly confined systems the effects of absorption is mitigated because of the shallow penetration depth. It is thus of considerable importance to enhance the dielectric function to the maximal attainable value. However very few materials are both transparent and have high dielectric constants in the visible portion of the spectrum. The usefulness and impact that photonic crystals will have will be greatly enhanced if these structures could be made to interact with visible light. The development of new high dielectric materials for use in photonic crystals for the visible and UV portions of the spectrum is thus of substantial importance.

Most of the current research and fabrication efforts into creating two and three-dimensional photonic crystals have utilized conventional semiconductor processing techniques or colloidal assemblies of spheres. An alternative methodology for creating photonic crystals out of self-assembling block copolymers has been formulated. By enhancing the dielectric contrast between the block copolymer domains one can create overlapping photonic band gaps which will inhibit the propagation of certain electromagnetic frequencies in the material. These in turn can be used as frequency selective reflectors that can be deposited on arbitrarily shaped surfaces for confining or reflecting light. The usefulness of these materials would be greatly enhanced if one could control the locality and the dimensionality of imperfections in the structures. Imperfections in a photonic band structure could lead to localized electromagnetic states, such that a point defect could act as a microcavity, a line defect like a waveguide.

surface defects can occur during the transformation from the homogeneous disordered state to the microphase-separated state. Understanding how to control the defects in block copolymer based photonic structures is critical for creating a new class of self-assembling optical materials. It is possible that dielectric enhanced block copolymers will be to photonic crystals what silicon has been to semiconductors - namely a materials platform from which one can tailor many types of devices. In this case the self assembling features will tend to shift the emphasis from processing to synthesis. I expect self assembling optical components to become available in the near to medium future and envision many opportunities in this unexplored area.

Much of the effort in the field has been directed towards the fabrication of optoelectronic devices, many other opportunities for utilizing photonic band gap materials exist in the larger context of optical properties, these opportunities have so far been largely overlooked. In particular the possibility of incorporating optical components in biological systems which may lead interesting applications such as new mechanisms for drug release (Fink *et al*, Provisional patent application).

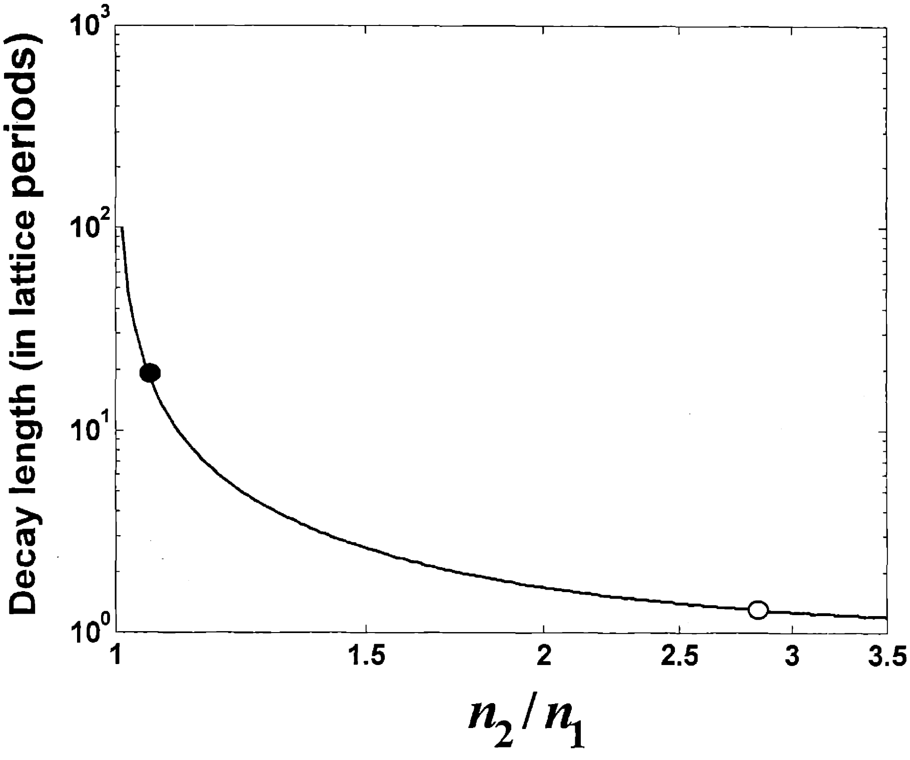

Figure 1.1 Decay length (in periods) of the electric field of an evanescent mode in a multilayer structure as a function of the relative index of refraction (quarter wave optical thickness). For a low index ratio systems such as polystyrene-polyisoprene ($(n_2/n_1)|_{\lambda=633} = 1.05$, filled circle) the decay length is about 19 periods, while for a high contrast system such as tellurium-polystyrene ($(n_2/n_1)|_{\lambda=10\mu m} \cong 2.9$, empty circle) the decay length is less than 2!

This thesis explores the formation and characteristics of photonic band gaps in two seemingly distinct dielectric potential regimes. The strong potential regime is analyzed in the second chapter leading to the construction of the omnidirectional reflector[1] concept. The material choice and fabrication technique both take advantage of the shallow penetration depth in this structure. The weak potential regime results in a large penetration depth of the evanescent electric-magnetic field into the structure, (upper left of Fig. 1.1). A substantial rejection of an electromagnetic wave can only be achieved by assembling many periods of the dielectric media. Chapter three presents a novel approach for the self-assembly of one, two and three-dimensional structures from block copolymers and discusses methods to enhance the potential in these systems. In chapters four and five future possible applications of the two enabling approaches are discussed. These examples include the Omniguide, a novel waveguide which guides light in air. And a first attempt at constructing self assembled microcavities where the optical confinement is provided by a self assembled 1D photonic crystal. These examples build on the unique capabilities which these approaches offer to solve problems which involve the confinement and manipulation of light.

---

[1] It turns out that omnidirectional reflectors can exist in weak potential regimes as well providing both indices are large! (see Fig. 2.3)

Chapter 2: The Omnidirectional Reflector

2.1 Introduction

Mirrors are probably the most prevalent of optical devices. Known to the ancients and used by them as objects of worship and beauty, mirrors are currently employed for imaging, solar energy collection and in laser cavities. Their intriguing optical properties have captured the imagination of scientists as well as artists and writers (Dodgson, C. L 1871).

One can distinguish between two types of mirrors, the age-old metallic, and more recent dielectric. Metallic mirrors reflect light over a broad range of frequencies incident from arbitrary angles (i.e. omnidirectional reflectance). However, at infrared and optical frequencies a few percent of the incident power is typically lost due to absorption. Multilayer dielectric mirrors are used primarily to reflect a narrow range of frequencies incident from a particular angle or particular angular range. Unlike their metallic counterparts, dielectric reflectors can be extremely low loss. The ability to reflect light of arbitrary angle of incidence for all-dielectric structures has been associated with the existence of a complete photonic bandgap (Yablonovitch E., PRL 1987, John S., PRL 1987), which can exist only a system with a dielectric function that is periodic along three orthogonal directions. Our recent theoretical analysis predicts that a sufficient condition for the achievement of omnidirectional reflection in a periodic system with an interface is the existence of an overlapping bandgap regime in phase space above the light cone of the ambient media (Winn J. N., Fink Y. *et al* 1998). We have extended the theoretical analysis and provided experimental realization of a multilayer omnidirectional reflector operable in infrared frequencies. The structure is made of thin layers of materials with different dielectric constants (polystyrene and tellurium) and combines characteristic features of both the metallic and dielectric mirrors. It offers metallic-like omnidirectional reflectivity together with frequency selectivity and low-loss behavior typical of multilayer dielectrics.

2.2 Theoretical analysis

The system we are considering is made of an array of alternating dielectric layers coupled to a homogeneous medium - characterized by n_0 (such as air with $n_0 = 1$) at the interfaces. Electromagnetic waves are incident upon the multilayer film from the homogeneous medium. While such a system has been analyzed extensively in the literature (Abeles F., 1950, Born M., Wolf E., 1953, Yeh, P., Yariv A., et al 1977) the possibility of omnidirectional reflectivity is not recognized until this thesis work.

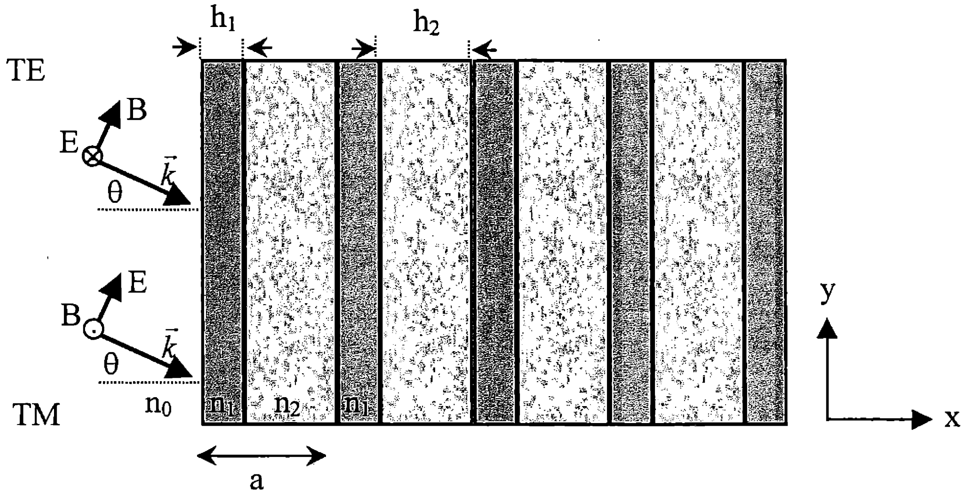

Figure 2.1 Schematic of the multilayer system showing the layer parameters (n_α, h_α – index of refraction and thickness of layer α), the incident wave vector $\vec{k}$ and the electromagnetic mode convention.

The generic system is described by the index of refraction profile in Fig. 2.1, where h_1 and h_2 are the layer thickness, and n_1 and n_2 are the indices of refraction of the respective layers. The incident wave has a wave vector $\vec{k} = k_x\hat{e}_x + k_y\hat{e}_y$ and frequency of $\omega = c|k|$. The wave vector together with the normal to the layers defines a mirror plane of symmetry which allows us to distinguish between two independent electromagnetic modes: transverse electric (TE) modes and transverse magnetic (TM) modes. For the TE mode the electric field is perpendicular to the plane, as is the magnetic field for the TM mode. The distribution of the electric field of the TE mode (or the magnetic field in the TM mode) in a particular layer within the stratified structure can be written as a sum of two plane waves traveling in opposite directions. The amplitudes of the two plane waves in a particular layer α of one cell are related to the amplitudes in the same layer of an adjacent cell by a unitary 2x2 translation matrix (Yeh, P., Yariv A. *et al* 1977).

General features of the transport properties of the finite structure can be understood when the properties of the infinite structure are elucidated. In a structure with infinite number of layers, translational symmetry along the direction perpendicular to the layers leads to Bloch wave solutions of the form

$$E_K(x,y) = E_K(x)e^{iKx}e^{ik_yy}, \tag{2.1}$$

where $E_K(x)$ is periodic, with a period of length a, and K is the Bloch wave number given by

$$K = \frac{i}{a}\ln\left(\frac{1}{2}Tr\left(U^{(\alpha)}\right) \pm \left(\frac{1}{4}\left(Tr\left(U^{(\alpha)}\right)\right)^2 - 1\right)^{1/2}\right). \tag{2.2}$$

Solutions of the infinite system can be propagating or evanescent, corresponding to real or imaginary Bloch wave numbers, respectively. The solution of Eq. (2.2) defines the band structure for the infinite system, $\omega(K,k_y)$. It is convenient to display the solutions of the infinite structure by projecting the $\omega(K,k_y)$ function onto the $\omega-k_y$ plane,

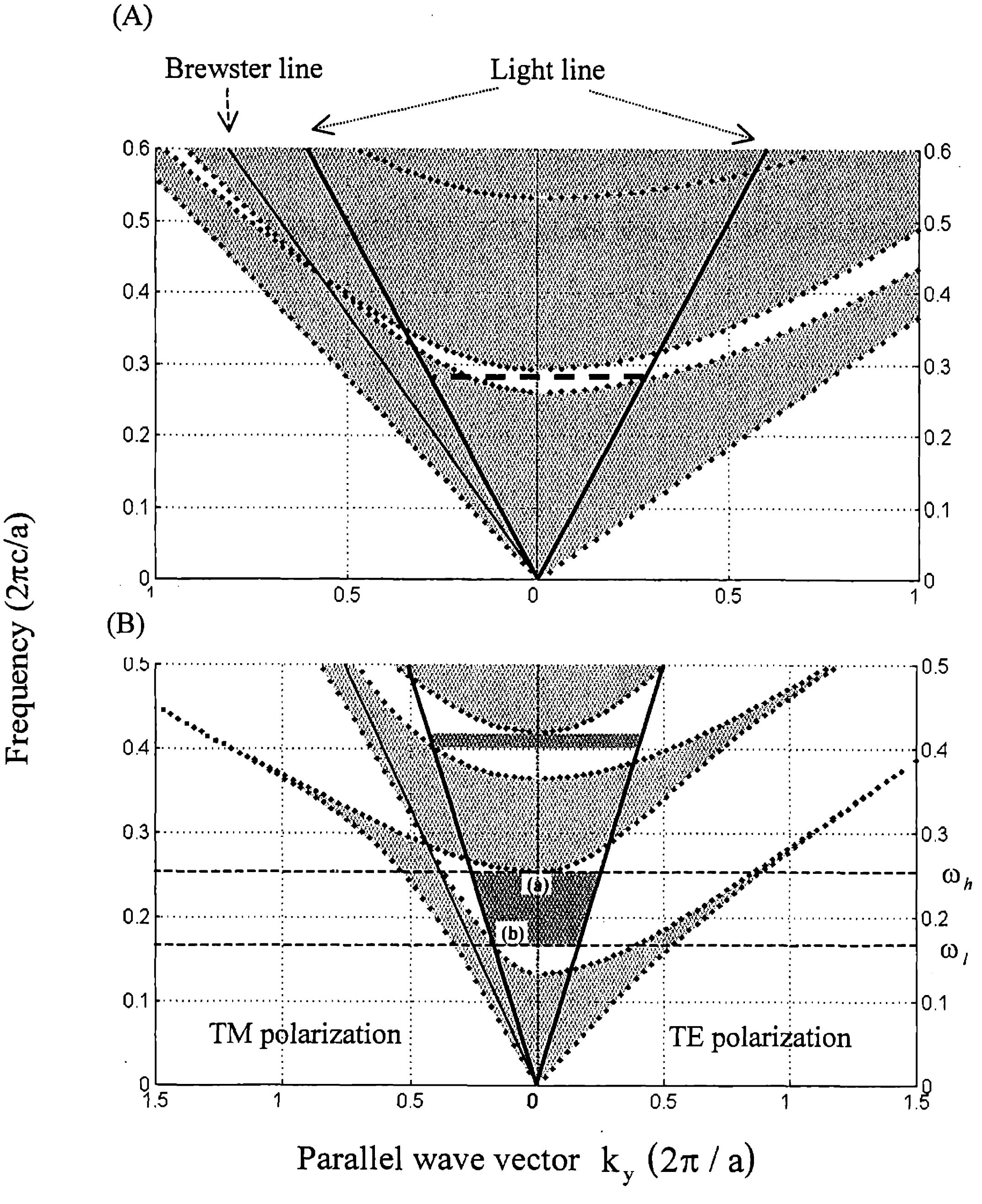

Figure 2.2 (A). Projected band structure of a multilayer film with the light line and Brewster line, exhibiting a reflectivity range of limited angular acceptance with ($n_1 = 2.2 \; and \; n_2 = 1.7$ and a thickness ratio of $h_2 / h_1 = 2.2 / 1.7$). (B) Projected band structure of a multilayer film together with the light line and Brewster line, showing an omnidirectional reflectance range at the first and second harmonic (propagating states – light gray, evanescent states – white, omnidirectional reflectance range – dark gray). The

film parameters are $n_1 = 4.6$ and $n_2 = 1.6$ with a thickness ratio of $h_2 / h_1 = 1.6 / 0.8$. These parameters are the same as the actual polymer-tellurium film parameters measured in the experiment.

Fig. 2.2(A) and Fig. 2.2(B) are examples of such projected structures. The gray areas highlight phase space where K is strictly real, that is, regions of propagating states, while the white areas represent regions containing evanescent states. The shape of the projected band structures for the multilayer film can be understood intuitively. At $k_y = 0$ the bandgap for waves travelling normal to the layers is recovered. For $k_y > 0$, the bands curve upward in frequency. As $k_y \to \infty$, the modes become largely confined to the slabs with the high index of refraction and do not couple between layers (and are therefore independent of k_x).

For a finite structure, the translational symmetry in the directions parallel to the layers is preserved, hence k_y remains a conserved quantity. In the direction perpendicular to the layers, the translational symmetry no longer exists. Nevertheless, the K-number, as defined in Eq. 2, is still relevant, because it is determined purely by the dielectric and structural property of a single bilayer. In regions where K is imaginary, the electromagnetic field is strongly attenuated. As the number of layers is increased, the transmission coefficient decreases exponentially, while the reflectivity approaches to unity.

Since we are primarily interested in waves originating from the homogeneous medium external to the periodic structure, we will focus only on the portion of phase space lying above the light line. Waves originating from the homogeneous medium satisfy the condition $\omega \geq ck_y / n_0$, where n_0 is the refractive index of the homogeneous medium, and therefore they must reside above the light line. States of the homogeneous medium with $k_y = 0$ are normal incident, and those lying on the $\omega = ck_y / n_0$ line with $k_x = 0$ are incident at an angle of 90°.

The states in Fig. 2(A), that are lying in the restricted phase space defined by the light line and that have a (ω, k_y) corresponding to the propagating solutions (gray areas) of the crystal can propagate in both the homogeneous medium and in the structure. These waves will partially or entirely transmit through the film. Those with (ω, k_y) in the evanescent regions (white areas) can propagate in the homogeneous medium but will decay in the crystal – waves corresponding to this portion of phase space will be reflected off the structure.

The multilayer system leading to Fig. 2.2(A) represents a structure with a limited reflectivity cone since for any frequency one can always find a k_y vector for which a wave at that frequency can propagate in the crystal – and hence transmit through the film. For example, a wave with $\omega = 0.285\ 2\pi c/a$ (dashed horizontal line in Fig 2a) will be reflected for a range of k_y values ranging from 0 (normal incidence) to $0.285\ 2\pi/a$ (90° incidence) in the TE mode, while in the TM mode it begins to transmit at a value of $k_y = 0.187\ 2\pi/\mathrm{a}$ (~41° incidence). The necessary and sufficient criterion for omnidirectional reflectivity at a given frequency is that there exist no transmitting state of the structure inside the light cone – this criterion is satisfied by frequency ranges marked in dark gray in Fig. 2(B). In fact, the system leading to Fig. 2(B) exhibits two omnidirectional reflectivity ranges.

The omnidirectional range is defined from above by the normal incidence band edge $\omega_h\left(k_x = \pi / a,\ k_y = 0\right)$ (point a in Fig. 2(B)) and below by the intersection of the top of the TM allowed band edge with the light line $\omega_l\left(k_x = \pi / a,\ k_y = \omega_l / c\right)$(point b in Fig. 2(B)).

The exact expression for the band edges is

$$\frac{1+\Lambda}{2} cos\left(k_x^{(1)} h_1 + k_x^{(2)} h_2\right) + \frac{1-\Lambda}{2} cos\left(k_x^{(1)} h_1 - k_x^{(2)} h_2\right) + 1 = 0, \qquad (2.3)$$

where $k_x^{(\alpha)} = \sqrt{\left(\omega n_\alpha / c\right)^2 - k_y^2}$ $(\alpha = 1,\ 2)$ and

$$\Lambda \equiv \begin{cases} \frac{1}{2}\left(\frac{k_x^{(2)}}{k_x^{(1)}} + \frac{k_x^{(1)}}{k_x^{(2)}}\right) & TE, \\ \frac{1}{2}\left(\frac{n_1^2 k_x^{(2)}}{n_2^2 k_x^{(1)}} + \frac{n_2^2 k_x^{(1)}}{n_1^2 k_x^{(2)}}\right) & TM. \end{cases} \qquad (2.4)$$

A dimensionless parameter used to quantify the extent of the omnidirectional range is the range to midrange ratio defined as $\left(\omega_h - \omega_l\right) / \frac{1}{2}\left(\omega_h + \omega_l\right)$.

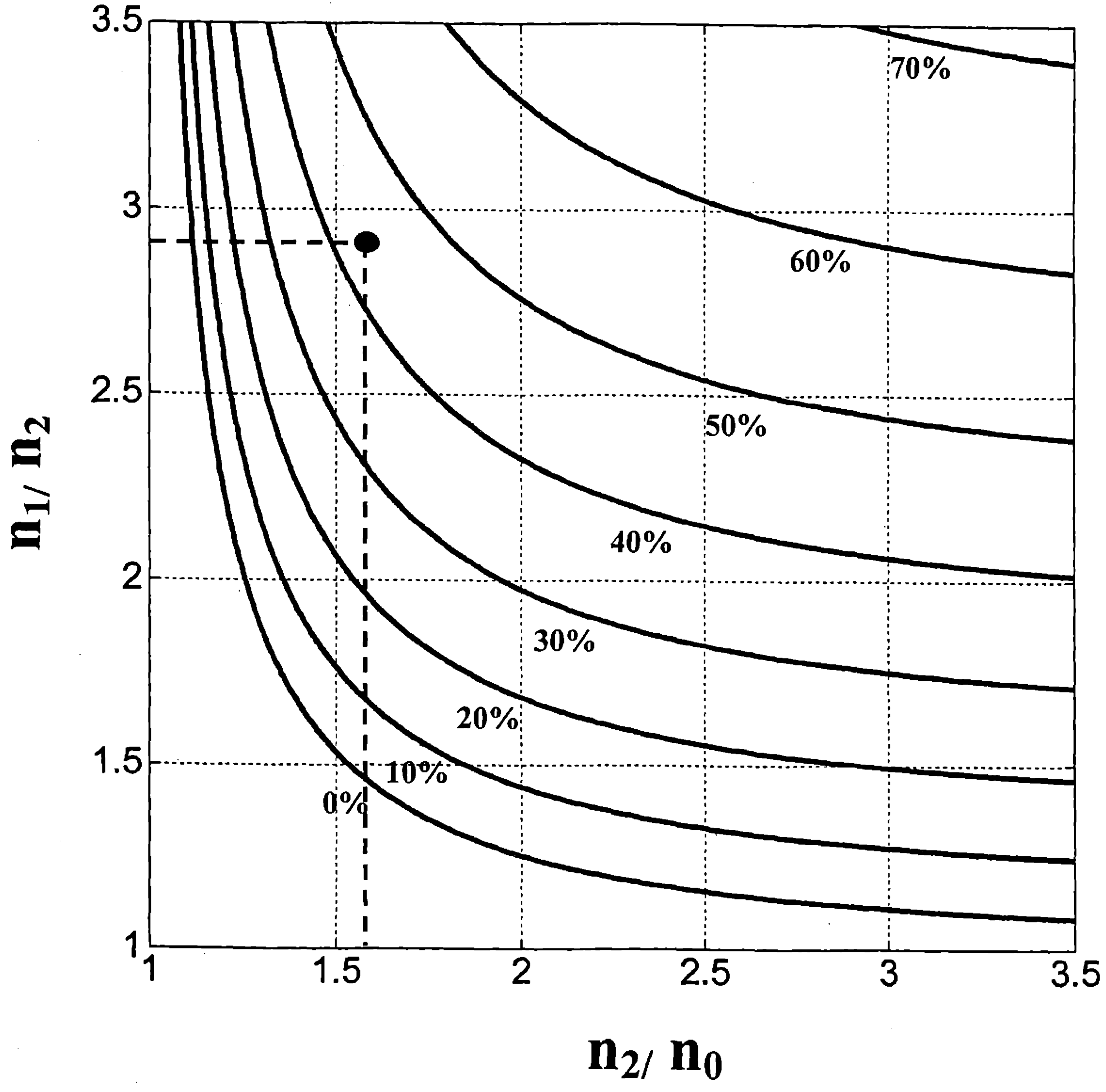

Figure 2.3 The range to midrange ratio $(\omega_h - \omega_l)/\frac{1}{2}(\omega_h + \omega_l)$, for the fundamental frequency range of omnidirectional reflection, plotted as contours. Here, the layers were set to quarter wave thickness and $n_1 > n_2$. The ratio for our materials is approximately 45%. ($n_1 / n_2 = 2.875$, $n_2 / n_0 = 1.6$) it is located at the intersection of the dashed lines (black dot).

Fig. 2.3 is a plot of this ratio as a function of n_2 / n_1 and n_1 / n_0 where ω_h and ω_l are determined by solutions of Eq. (2.3) with quarter wave layer thickness. The contours in this figure represent various equi-omnidirectional ranges for different material index parameters and could be useful for design purposes.

It may also be useful to have an approximate analytical expression for the extent of the gap. This can be obtained by setting $cos\left(k_x^{(1)}h_1 - k_x^{(2)}h_2\right) \cong 1$ in Eq. 2.3. We find that for a given incident angle θ_0, the approximate width in frequency is

$$\Delta\omega\left(\theta_0\right) = \frac{2c}{h_1\sqrt{n_1^2 - n_0^2\,sin^2\theta_0} + h_2\sqrt{n_2^2 - n_0^2\,sin^2\theta_0}}\left[cos^{-1}\left(-\sqrt{\frac{\Lambda-1}{\Lambda+1}}\right) - cos^{-1}\left(\sqrt{\frac{\Lambda-1}{\Lambda+1}}\right)\right]. \tag{2.5}$$

At normal incidence there is no distinction between TM and TE modes. At increasingly oblique angles the gap of the TE mode increases, whereas the gap of the TM mode decreases. In addition the center of the gap shifts to higher frequencies. Therefore the criterion for the existence of omnidirectional reflectivity can be restated as the occurrence of a frequency overlap between the gap at normal incidence and the gap of the TM mode at 90°. Analytical expressions for the high and low frequencies of an omnidirectional band gap are

$$\begin{aligned}
\omega_h &= \frac{2c}{h_2 n_2 + h_1 n_1}\cos^{-1}\left(-\left|\frac{n_1 - n_2}{n_1 + n_2}\right|\right), \\
\omega_l &= \frac{2c}{h_2\sqrt{n_2^2 - n_0^2} + h_1\sqrt{n_1^2 - n_0^2}}\cos^{-1}\left(\left|\frac{n_1^2\sqrt{n_2^2 - n_0^2} - n_2^2\sqrt{n_1^2 - n_0^2}}{n_1^2\sqrt{n_2^2 - n_0^2} + n_2^2\sqrt{n_1^2 - n_0^2}}\right|\right).
\end{aligned} \tag{2.6}$$

In general the TM mode defines the lower frequency edge of the omnidirectional range an example can be seen in Fig. 2.2(B) for a particular choice of the indices of refraction. This can be proven by showing that

$$\left.\frac{\partial\omega}{\partial k_y}\right|_{TM} \geq \left.\frac{\partial\omega}{\partial k_y}\right|_{TE} . \tag{2.7}$$

in the region that resides inside the light line. The physical reason for Eq. (2.7) lies in the vectorial nature of the electric field. In the upper portion of the first band the electric field concentrates its energy in the high dielectric regions. Away from normal incidence the electric field in the TM mode has a component in the direction of periodicity, this component forces a larger portion of the electric field into the low dielectric regions. The group velocity of the TM mode is therefore enhanced. In contrast, the electric field of the TE mode is always perpendicular to the direction of periodicity and can concentrate its energy primarily in the high dielectric region.

2.3 Design and fabrication

A polystyrene-tellurium (PS-Te) material system was chosen to demonstrate omnidirectional reflectivity. Tellurium has a high index of refraction and low loss characteristics in the frequency range of interest. In addition, its relatively low latent heat of condensation together with the high glass transition temperature of the PS minimizes diffusion of Te into the polymer layer. The choice of PS, which has a series of absorption peaks in the measurement range (Pouchert, Charles J., 1985), demonstrates the competition between reflectivity and absorption that occurs when an absorption peak is located in the evanescent state region. The Te(0.8μm) and PS (1.65μm) films were deposited (Appendix A) sequentially to create a nine-layer film starting with the tellurium layer.

The optical response of this particular multilayer film was designed to have a high reflectivity region in the 10 to 15μm range for any angle of incidence (in the experiment we measured from 0° to 80°). The optical response at oblique angles of incidence was measured using a Fourier Transform Infrared Spectrometer (Nicolet 860) fitted with a polarizer (ZnS SpectraTech) and an angular reflectivity stage (VeeMax by SpectraTech). At normal incidence, the reflectivity was measured using a Nicolet Infrared Microscope. A freshly evaporated aluminum mirror was used as a background for the reflectance measurements.

2.4 Measurements

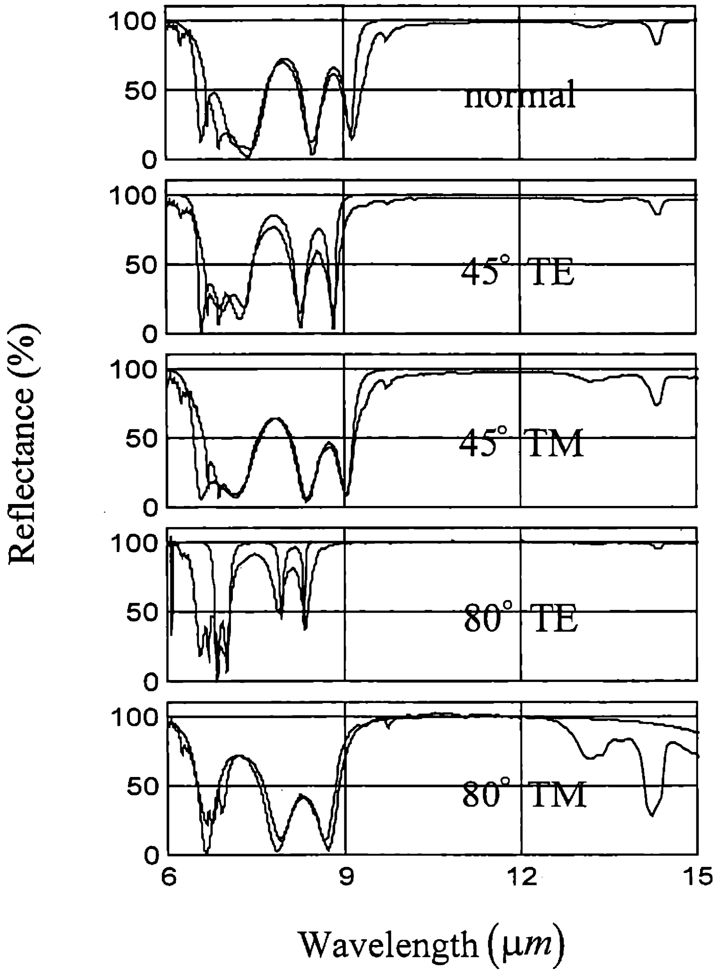

Figure. 2.4 Calculated (solid line) and measured (dashed line) reflectance (%) as a function of wavelength for TM and TE modes at normal, 45°, and 80° angles of incidence, showing an omnidirectional reflectivity band.

Fig. 2.4 shows good agreement between the calculated and measured reflectance spectra at normal, 45° and 80° incidence for the TM and TE modes. The regimes of high reflectivity at the different angles of incidence overlap thus forming a reflective range of frequencies for light of any angle of incidence. The frequency location of the omnidirectional range is determined by the layer thickness and can be tuned to meet specifications. The range is calculated from Eq. (2.6) to be 5.6μm and the center wavelength is 12.4μm corresponding to a 45% range to midrange ratio shown in dashed lines in Fig 2.3 for the experimental index of refraction parameters. These values are in agreement with the measured data[1]. The calculations are for lossless media and therefore do not predict the PS absorption band at ~ 13 and 14 microns. The PS absorption peak is seen to increase at larger angles of incidence for the TM mode, and decrease for the TE mode. The physical basis for this phenomena lies in the relation between the penetration depth and the amount of absorption. The penetration length is

$$\xi \propto Im(1/K), \tag{2.8}$$

with K the Bloch wave number. A detailed analytic expression of the decay length is derived in Appendix C.

It can be shown that ξ is a monotonically increasing function of the incident angle for the TM mode of an omnidirectional reflector and is relatively constant for the TE mode. Thus, the TM mode penetrates deeper into the structure at increasing angles of incidence (Table 1) and is more readily absorbed. The magnitude of the imaginary part of the Bloch wave number for a mode lying in the gap is related to its distance from the band edges. This distance increases in the TE mode due to the widening of the gap at increasing angles of incidence and decreases in the TM mode due to the shrinking of the gap.

---

[1] The absolute reflectivity at 45° measured with a CO_2 laser was higher than 98.5%.

Angle of incidence (degrees)	ξ_{TM} (μm)	ξ_{TE} (μm)
0	2.51	2.51
45	3.05	2.43
80	4.60	2.39

Table 1. Penetration depth (μm) at different angles of incidence for the TE and TM modes.

2.5 Summary and Discussion

A design criterion that permits truly omnidirectional reflectivity for all polarizations of incident light over a wide selectable range of frequencies was derived and used in fabricating an all-dielectric omnidirectional reflector consisting of multilayer films. The reflector was constructed as a stack of nine alternating micrometer-thick layers of polystyrene and tellurium and demonstrates omnidirectional reflection over the wavelength range from 10 to 15 micrometers. The materials and processes were chosen for their low cost and applicability to large area coverage. In addition to omnidirectionality, the measurements show that a polymer, while lossy in the infrared, can still be used for reflection applications without a considerable sacrifice of performance. Because the omnidirectionality criterion is general, it can be used to design omnidirectional reflectors in many frequency ranges of interest. Potential uses depend on the geometry of the system. For example, coating of an enclosure will result in an optical cavity. A hollow tube will produce a low-loss, broadband waveguide which will be discussed later in chapter 4, planar film could be used as an efficient radiative heat barrier or collector in thermoelectric devices.

Chapter 3: Self Assembled Block Copolymer Photonic Crystals

3.1 Introduction

A conceptual framework for constructing photonic crystals from self-assembling block copolymers is presented in this chapter. In order to form useful band gaps in the visible regime, periodic dielectric structures made of typical block copolymers need to be modified to obtain appropriate characteristic distances and dielectric constants. Moreover, the absorption and defect concentration must also be controlled. This affords the opportunity to tap into the large structural repertoire, the flexibility and intrinsic tunability that these self-assembled block copolymer systems offer.

A symmetric poly(styrene-b-isoprene) (~400k MW) block copolymer was used to achieve a photonic band gap in the visible regime. By swelling the diblock copolymer with lower molecular weight constituents control over the location of the stop band across the visible regime is demonstrated. One and three-dimensional crystals have been formed by changing the volume fraction of the swelling media.

Block copolymers (BCP) consist of chemically different macromolecules, or blocks, joined at their endpoints to form a chain. Due to the positive free energy of mixing of the A and B species, the respective blocks tend to segregate. Being restricted by their connectivity, block copolymers microphase separate into microdomains that are on the length-scales of the respective blocks.

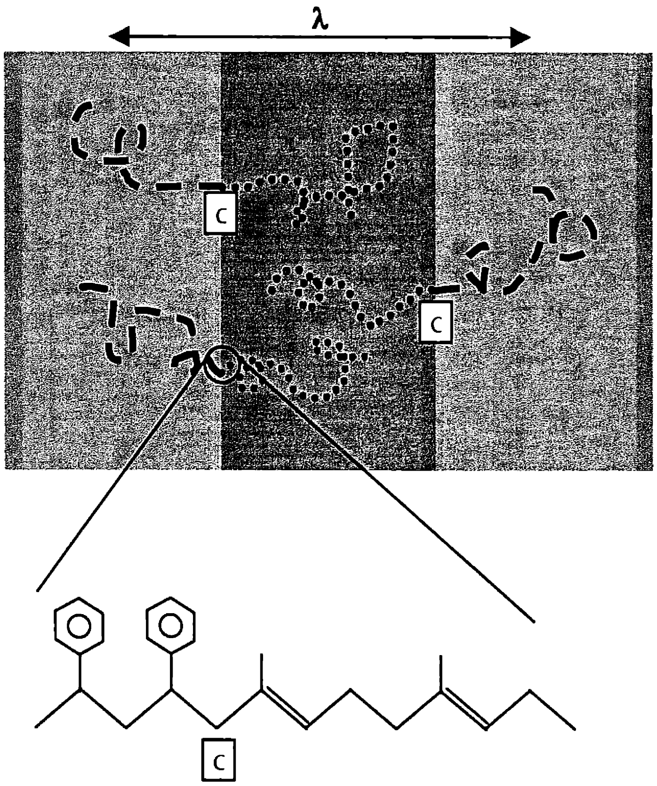

Figure 3.1 Schematic of a diblock copolymer microphase separated into a lamellar structure of period λ. The two blocks are covalentaly connected at point c. The locus of the junction points is called the intermaterial dividing surface. On the bottom is the chemical structure of the junction region for a styrene isoprene diblock.

Fig. 3.1 depicts an A/B diblock copolymer which has microphase-separated into a layered structure. Each layer is comprised of a different block. The interface between the layers is called the intermaterial dividing surface (IMDS) and is the location of the junctions which connect the different blocks. The block length is determined by the number of repeat units, N_A connected repeat units of type A in block A while block B has N_B repeat units of type B.

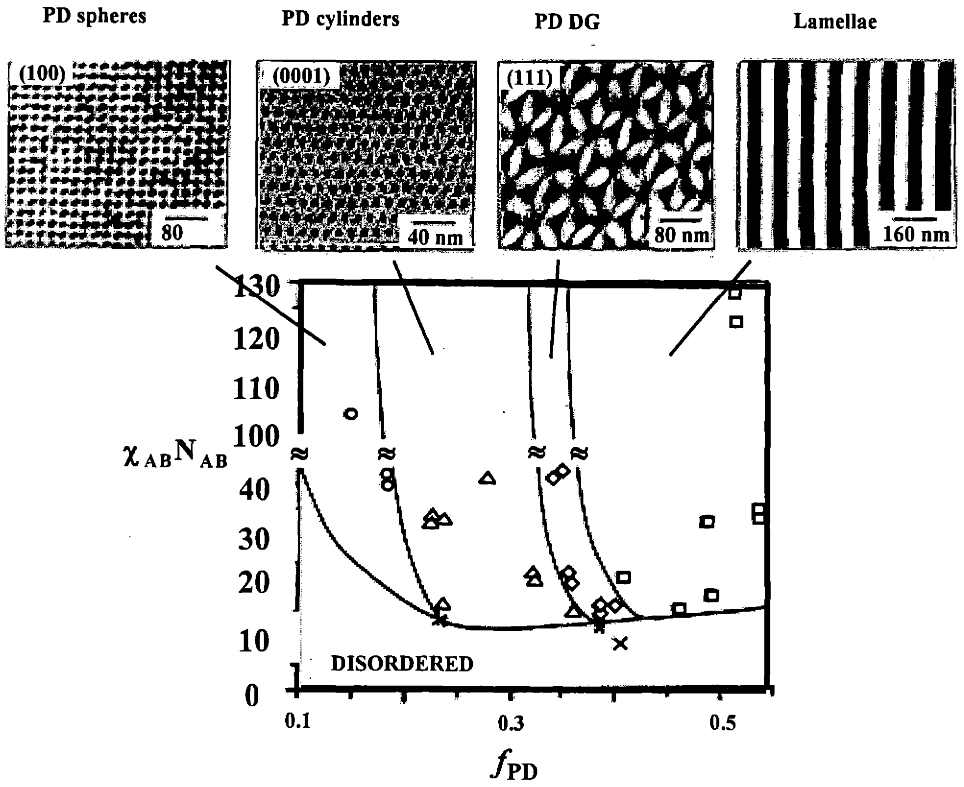

Figure 3.2 Experimental morphology diagram depicting the periodic microphases observed in the polystyrene-polydiene (PS-PD) diblock copolymer systems disordered homogenous (x), BCC spheres (o), hexagonally packed cylinders (△), double gyroid(◇), lamellae (□) The PS phase appears light, and the PD phase appears dark due to staining with OsO_4. χ_{AB} - is the Flory-Huggins parameter, N_{AB} =(N_A + N_B) - number of statistical segments in the copolymer (Thomas E. L., Lescanec R. L. 1994).

The morphology diagram for a linear A/B diblock copolymer is presented in Fig. 3.2. The regimes of the different phases are mapped as a function of the volume fraction of the two blocks - f and the product of the segment-segment interaction parameter χ_{AB} and the total number of segments N_{AB}. At a given value of $N_{AB}\chi_{AB}$ as the volume fraction is changed various periodic structures are encountered: spheres on a body centered cubic lattice, hexagonally packed cylinders, double gyroid cubic and lamellae. A graphic rendering of the different equilibrium phases at increasing volume fraction of the minority component is presented in Fig. 3.3.

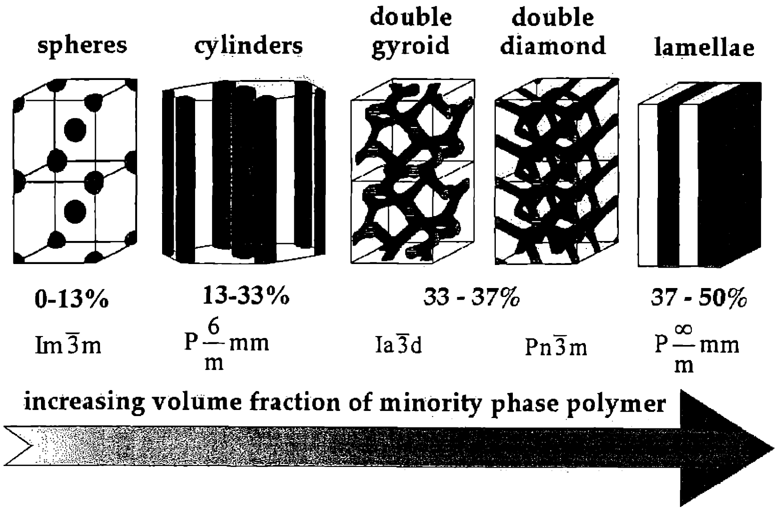

Figure 3.3 Graphic rendering of the equilibrium phases in linear diblock copolymer at increasing volume fraction of minority phase.

Deviating from the simple diblock by adding more blocks, choosing different chemical monomers, and varying the architecture of the chain leads in some cases to the formation of other two and three dimensional periodic structures. For example, an ABC terpolymer can have three chemically distinct blocks connected in a linear fashion with two junctions per molecule or have the three blocks connected at a single junction resulting in a mixed arm star polymer One particularly striking example is the so called “knitting pattern” (Breiner U., Krappe U. *et al* 1998) which forms from a linear ABC tercopolymer comprised of polystyrene, poly(ethylene-co-butylene) and polymethylmethacrylate (PS-PEB-PMMA) with 0.35:0.27:0.38 volume fractions. A micrograph as well as a graphic rendering of the structure are presented in Fig. 3.4. The “knitting pattern” structure is two-dimensional periodic and corresponds to the c2mm plane group. A calculation of the photonic band structure of the knitting pattern is presented in Appendix B.

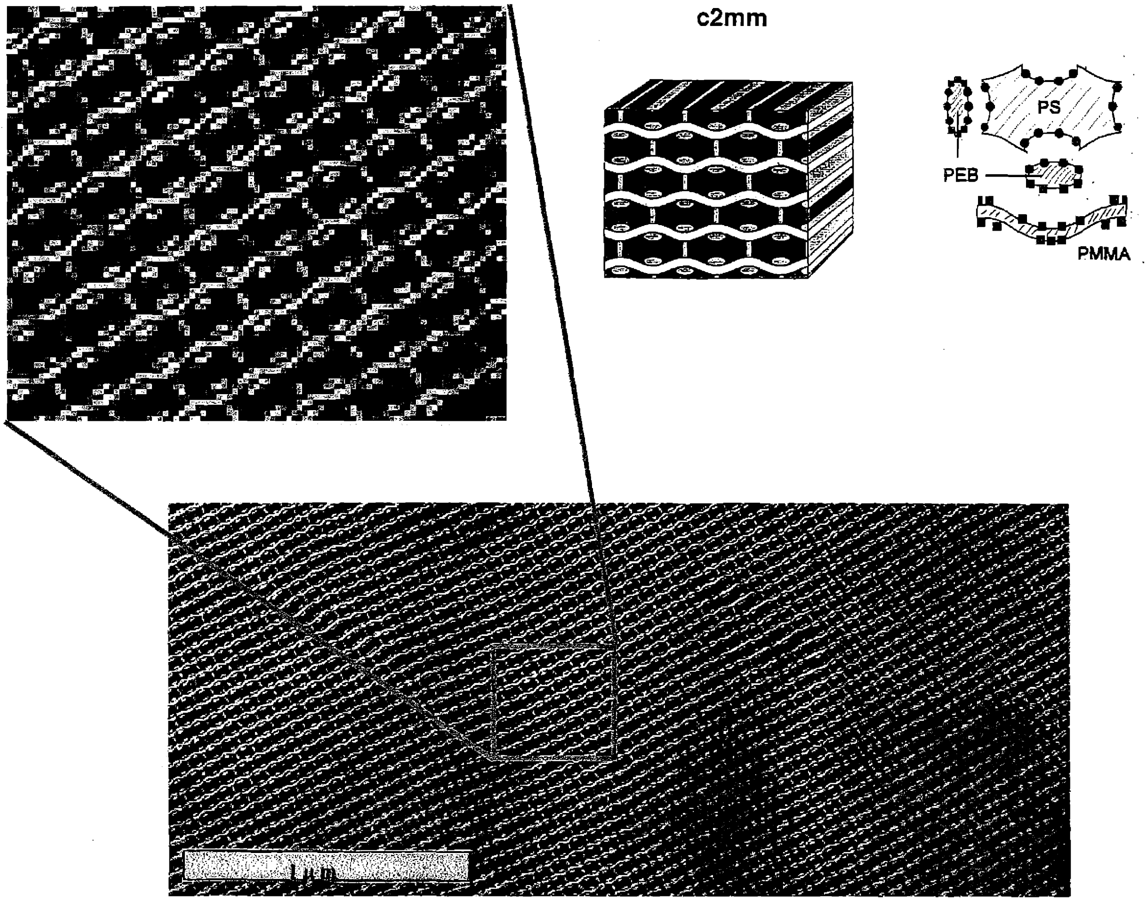

Fig. 3.4 Micrograph of knitting pattern in PS-PEB-PMMA triblock terpolymer (Breiner U., Krappe U. *et al* 1998).

3.2 Layout of the problem, the four D's

The simplest A/B diblock copolymers self assemble into equilibrium phases consisting of alternating layers, complex topologically connected cubics, cylinders on hexagonal lattices, and spheres on a body centered lattice. The lattice spacing of these structures is related to the overall molecular weight and is typically on mesoscopic length scales (10-50nm).

The small intrinsic dielectric contrast between typical block copolymer microdomains gives rise to small photonic gaps around the edges of the Brillouin zone. This in turn, results in a deep penetration depth for the evanescent waves, necessitating large numbers of layers and low absorption losses as essential in this type of structure in order to achieve high values of reflectivity . A dimensionless number can be defined which can be used to compare the relative strengths of the reflectivity vs. absorption,

$$\rho\alpha(\lambda,\theta)=\frac{\lambda\kappa(\lambda,\theta)}{2\pi k}, \tag{3.1}$$

The competition between reflectivity and absorption for a particular structure and at a particular wavelength λ and angle of incidence - θ and, can be gauged by the magnitude of the dimensionless parameter ρα, which is a ratio of the imaginary part of the Bloch wave number - κ and the imaginary part of the index of refraction – k . Values of ρα much greater than unity indicate a reflectivity dominated structure while values that are smaller than unity correspond to an absorption dominated structure.

Depending on the spectral region different mechanisms will contribute to absorption in polymers. At high frequencies (UV) bond dissociation (and oxidation if oxygen is present) are important while in the IR spectral regime rotation, and vibrational degrees of freedom can exhibit sharp absorption lines or broad absorption ranges. Because of the substantial UV absorption one needs to increase the period length such that the reflectivity dominated range is at longer wavelengths than the absorption dominated regime.

To obtain substantial rejection of the E-M wave in the strong absorption regimes one needs to increase the dielectric contrast which will increase ρα as well as the overlap between the photonic gaps in different directions.

The objectives of this study are to create self assembled structures made of block copolymers which have observable photonic band gaps.

To this end four key points need to be addressed (the 4 **D**'s):

1. **Distance** - The period length which is typically on the order of 20-40nm needs to be increased to >100nm in order for the structure to be in the reflectivity dominated regime.
2. **Dielectric contrast** – In general, the extent of the photonic band gap in a particular direction in frequency is an increasing function of the dielectric contrast (defined for a simple two component system as $\varepsilon_{structure} / \varepsilon_{matrix}$). The larger the contrast, the larger the gap overlap between the different directions will be. Also larger gaps are associated with shallow penetration depth for the evanescent wave.
3. **Dissipation** – The control of dissipation is extremely important, and depending on the application, different levels and dissipation characteristics can be tolerated. When very high confinement is required one usually would like to operate well within the reflectivity dominated regime, in which case dissipation should be minimized. In other cases absorption can be tolerated or even used to an advantage (to bring out color effects or to remove certain "lossy modes").
4. **Defects** – Defects of various types will invariably appear in self assembled systems. The these in turn can couple to modes in the gap region and alter the band structure of the crystal. One would want to minimize the density of defects such that their impact could be mitigated. Defects could also be engineered to create localized states in their vicinity, in this case one would like to introduce in a controlled manner defects of

specific dimensionality, size, symmetry and dielectric constant in order to achieve localization of light.

3.3 Controlling the period length in block copolymers

The usefulness of BCP PBG materials would be greater if they exhibited band gaps in the visible region of the spectrum (Jenekhe S. A., Chen X. L., 1999). Structures will begin to exhibit band gaps in the visible portion of the spectrum if the characteristic domain size is on the order or greater than 400/4n nm where n is the index of refraction of the material in that domain. The domain sizes of typical block copolymers are usually 10-50nm, although distances much larger than these are made possible by employing rigid, extended chain blocks, very high molecular weight flexible chain blocks (Chen J. T., Thomas E. L. *et al, 1996*) as well as swelling the domains by the addition of low molecular weight components[1] (Winney, K., I., Thomas E. L. *et al*, 1991). In the strong segregation regime the scaling of domain size with molecular weight is proportional to $N^{2/3}$ where N is the total number of segments. In rigid rod block copolymers the scaling is N^1 which forms larger periods with lower chain lengths. Another technique involves applying a force field to stretch the polymer chains thereby increasing the period length.

3.4 Methods for refractive index enhancement

To increase the photonic band overlap for BCP mesocrystals of typical composition one needs to increase the intrinsic dielectric contrast between the phases. In virtually all BCP

---

[1] The validity of this approach in achieving control over the domain spacing at optical length scales has recently been demonstrated with a styrene isoprene block copolymer of molecular weight 194kg/mol and 197kg/mol swollen with homopolymer styrene (13k), homopolymer isoprene (13k) and a solvent resulting in a visible spectrum reflector (see 3.6).

systems the dielectric contrast (taken as the ratio of the high index to low index of refraction) is typically on the order of 1.1 (e.g polystyrene/ polyisoprene 1.59/1.51=1.05). This contrast is sufficient only for narrow band openings near the edges of the Brillouin zone. In order to achieve larger gaps one needs to enhance the dielectric contrast, this can be done in a variety of ways. For example, it is possible to preferentially sequester optically transparent nanocrystals (Murray C. B., Norris D. J. *et al,* 1993) of one or more high dielectric constant material into one or more of the block copolymer microdomains (Fogg D., Radzilowski L. H., 1997). The nanocrystals are tailored to have a strong affinity to one of the phases. This can be achieved for example by grafting a surfactant molecule, which has a chemical structure similar to that of the target phase onto the surface of the nanocrystal.

Nanocrystals are particularly suitable for refractive index enhancement in self asssembling BCP systems. First their small size minimizes the hinderence to the ordering process. In addition the electronic band gap is inversely related to the cluster size this causes a blue shift in the absorption band and permits the use of materials in spectral regimes where they absorb in the bulk. An example is CdSe which has a bulk absorption band at 1.77eV. A 3nm CdSe nanocrystallite has a gap at approximately 2.48eV which means that it is transparent through most of the visible spectrum.

The BCP PBG material is produced by adding the surfactant-nanocrystals to a solution of the block copolymer where upon removal of the solvent sequester into the targeted microdomains. The result is an increase in the dielectric constant of that microphase.

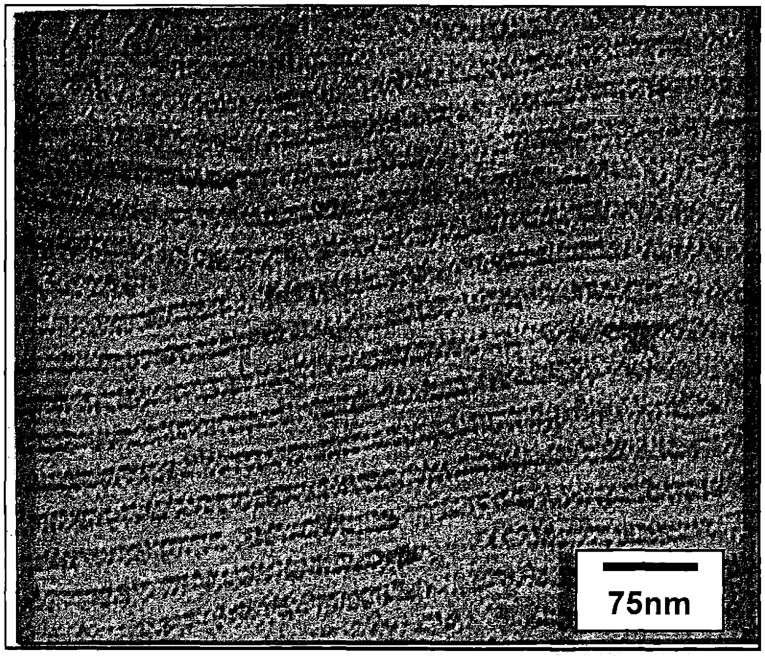

Figure 3.5 One-dimensional self-assembled dielectric lattice made of PS-PI-P2VP triblock polymer with TOPO coated CdSe nanocrystals sequestered in the P2VP phase.

Fig. 3.5 is a bright field TEM image of a self assembled layered dielectric lattice made by the selective incorporation of high index CdSe nanocrystals to the poly(2-vinyl pyridine) (P2VP) microdomains of a poly(styrene-b-isoprene-b-2-vinylpyridine) triblock terpolymer. The contrast in this figure is due to the sequestration of the nanocrystals into the 2VP phase. The affinity of the CdSe nanoparticles to the 2VP phase is due probably to the Lewis base character of the 2VP which coordinates to the polar surface of the crystallite. The volume fraction of CdSe in the sample above is estimated to be ~10% which would lead to an effective index of refraction of 1.71 of the 2VP phase. (Based on a refractive index of ~2.7 for CdSe). By adding different types of surfactant molecules (see appendix D), one can sequester the nanocrystallites into other polymers, for example thiol terminated polystyrene chains were used to sequester the dots into polystyrene domains; as well an amine terminated polystyrene had a similar effect.

Another possible approach to enhance the dielectric contrast involves the selective etching of one of the microphases. For example a recently developed (Chan V. Z-H, Hoffman, J., *et al*, 1999) technique involving the removal by ultra-violet irradiation and subsequent ozonolysis of the isoprene phase in a silicon containing block copolymer.

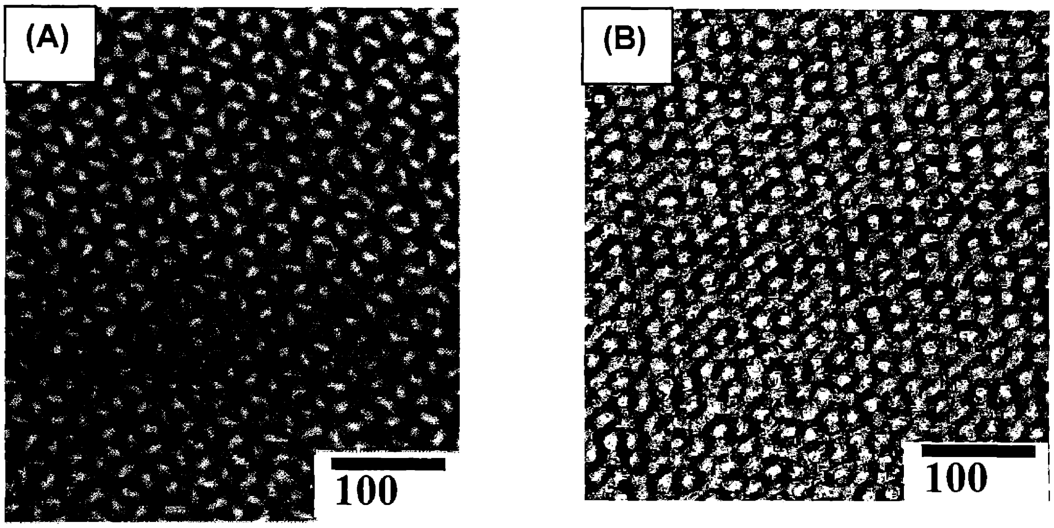

Figure 3.6 Three dimensional topologically connected double gyroid structure (A) PI channels (dark) in a P(PMDSS) matrix. (B) air channels in a siliconoxycarbide matrix (Chan V. Z-H., Thomas E. L. *et al*, 1999).

Fig. 3.6. is a bright field TEM image of poly(pentamethyldisilyl-styrene)-b-polyisoprene which forms the double gyroid morphology in the bulk. The sample was cast from toluene, annealed at 120C for two weeks, cryo-microtomed and the polyisoprene preferentially stained with osmium tetroxide. As shown in Fig. 3.6(a), the PI channels appear dark in a matrix of P(PMDSS). An unstained microtomed section was also exposed to an atmosphere of 2 wt% ozone in oxygen for 45 minutes and then soaked in

deionized water for 12 hours. As seen in Fig. 3.6(B), the PI has been preferentially removed, leaving behind air channels which results in the inversion of the image contrast as compared to Fig. 6(A). In addition, upon exposure to oxidation, (PMDSS) converts to siliconoxycarbide. The contrast in the micrograph is due entirely to the difference in electron density between the air and ceramic phases. The dielectric contrast in this material is approximately 2 (Chan V. Z-H., Thomas E. L. *et al*, 1999). The air channels could also be backfilled with a high index material (such tetra-propoxy titane, a TiO_2 precursor) and calcinated to achieve a high index dielectric network (J. Wijnhoven, W. L. Vos 1998).

The practical short wavelength limit for the use of polymers is probably around a wavelength of 300nm due to their strong absorption in the ultra violet regime.

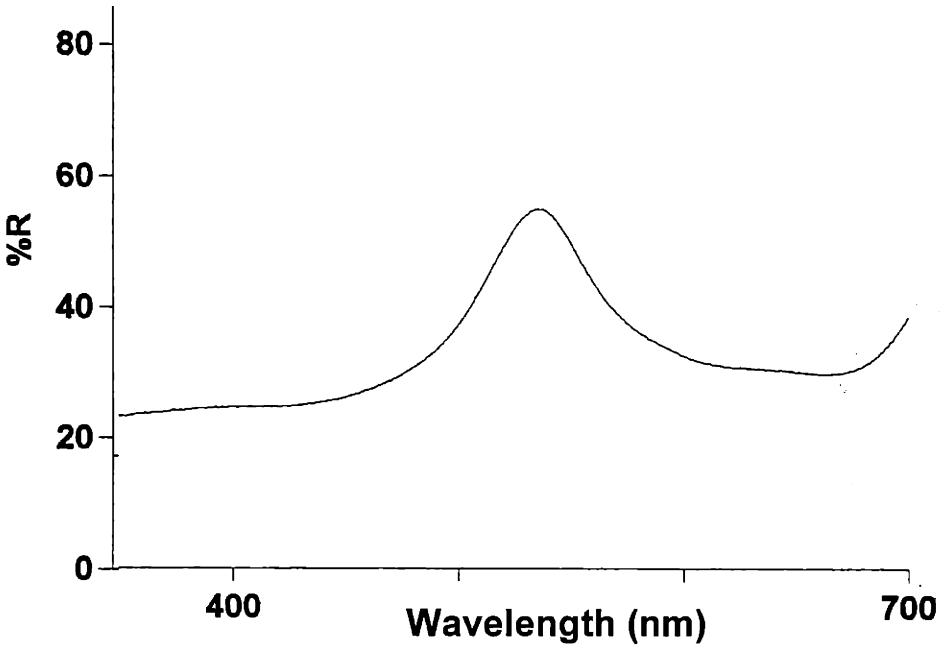

Figure 3.7 Reflectivity of a self assembled layered dielectric. The system consists of a blend of poly(styrene-b-isoprene) diblock copolymer with 20 weight % thiol terminated polystyrene oligomer grafted to 3nm CdSe nanocrystals and 20 weight % PI homopolymer. The CdSe nanocrystallites sequester into the polystyrene phase, which enhances the index of refraction contrast between the layers.

Fig. 3.7 is a reflectivity spectra taken from a styrene-isoprene (poly(styrene-b-isoprene) (PS-PI) block copolymer (MW 194kg/mol:197kg/mol, PDI=1.02, synthesized anionically by Maria Xenidou, Exxon Research, NJ) where the domains have been swollen by the addition of an isoprene homopolymer (20% by weight, MW 13kg/mol, PDI=1.06 Pressure Chemical Co.) and a thiol terminated polystyrene (20% by weight, MW 1.3kg/mol L. Fetters Exxon research). The refractive index contrast between the domains was enhanced by the addition of CdSe nanoparticles. The sample was prepared by dissolving all of the components in toluene and subsequent casting on a glass microscope cover slide, the total film thickness is approximately 50 microns. The particles sequester into the polystyrene domains because of their affinity to the thiol group. The reflectivity was measured on a Cary Spectrophotometer fitted with an integrating sphere. The maximal reflectivity peak is observed at 540nm. The sample begins to reflect visible light after the solvent evaporates (which could take a few minutes if air is blown over the sample). The equilibrium structure for a symmetric diblock swollen with the respective homopolymers consists of alternating lamellae of polystyrene and isoprene with an approximate layer thickness of 85nm for each layer.

3.5 Methods for producing globally oriented dielectric lattices

3.5.1 Methods

The rejection potential of a finite dielectric lattice depends on the index contrast and on the number of lattice periods; lower contrast requires an increased number of periods for a given rejection value. In addition since the wave penetrates deeply into the structure imperfections become more important. It is therefore essential to achieve a high degree of control over defect formation in block copolymer systems. Quiescent casting leads to a small grain size with many grain boundary defects. Nearly single-crystal BCP's can be formed by having the disorder to order transition occur in the present of a biasing force field.

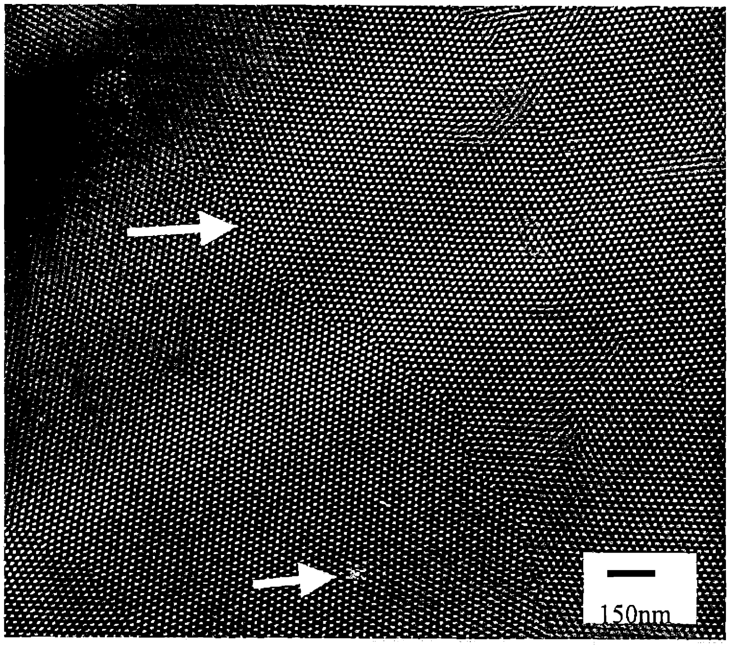

Figure 3.8 Triangular array of PS cylinders in a PI matrix showing near single crystal qualities (Honeker C. C., Thomas E. L. 1996), low angle grain boundaries and point defects are evident.

Fig. 3.8. is an example of cylinders on an hexagonal array, where the excellent long range order in this sample was achieved by the roll casting technique. In this method the polymer solution evaporates under the influence of a complex flow field created by a pair of counter rotating cylinders (Albalak, R. J., Thomas E. L. 1993). The disorder to order transition takes place in the presence of the flow field leading to a global orientation of the microdomains. BCP's can also be made to form single crystals by application of other force fields such as electric fields, and substrate fields. For example, to achieve a particular orientation and location of the mesocrystal with respect to a substrate, one can introduce a chemically patterned surface which has an affinity to one of the microphases(Fasolka M., Harris D. J. *et al* 1997). This, in turn, can lead to epitaxial relations between the surface and the polymer crystal (De Rosa, C., *et al* to be published 2000)

3.5.2 Flow field aligned dielectric lattice – fabrication procedure

The following procedure was used to obtain highly ordered arrays of block copolymer – CdSe nanocrystal composites:

(a) A solution of the nanocrystals in a solvent which dissolves the two blocks of the polymer was prepared, and if needed, an end-functionalized oligomer was added to enhance the sequestration of the nanocrystals.

(b) The block copolymer was added to the solution and stirred well to form a viscous solution (~1g/2ml of solvent for a 100k BCP).

(c) The solvent was removed in the presence of a flow field in a roll casting apparatus.

(d) The solvent is allowed to further evaporate and the film is subsequently annealed.

3.5.3 A 1D self assembled dielectric crystal with CdSe nanocrystals

A solution of CdSe nanocrystals in tetrahodrofuran was prepared at a concentration of 0.078mol/l. A poly(styrene-b-isoprene-b-2vinylpyridine) (23k:54k:23k synthesized by L. Fetters, Exxon Research and Engineering) triblock terpolymer was added to the solution (0.6g/2.4ml) and allowed to dissolve for 12h – to obtain a clear red solution. Approximately 0.7ml of the solvent was allowed to evaporate to increase viscosity into a range appropriate for roll casting. The solution was roll at 40RPM and removed with ethanol after 15 minutes of drying. Finally the oriented film was annealed for 7 days at 120C to improve the long range order.

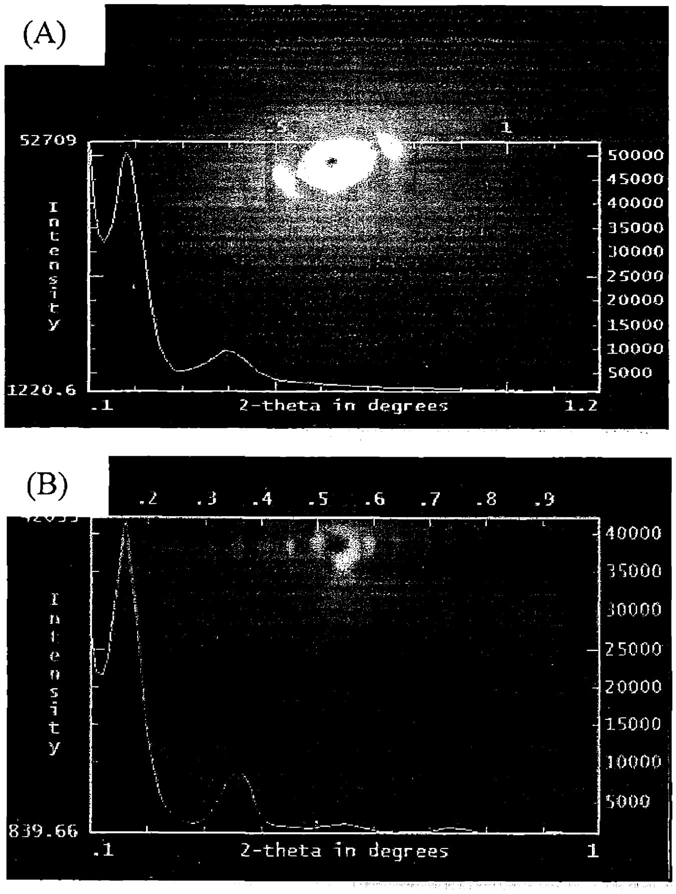

Figure 3.9 Two dimensional small angle x-ray patterns of a roll cast 1D dielectric lattice made of a triblock terpolymer (PS-PI-P2VP) loaded with CdSe nanocrystals prior to (A)

and after (B) annealing. Superposed is 1D plot of the intensity as a function of 2 theta along the direction parallel to the layer normal.

Transmission electron microscopy of the resulting structure (Fig. 3.5) shows that the CdSe nanocrystals sequester into the P2VP phase in fact at this concentration (~5 volume %) they appear to sequester at the interface between the isoprene and the 2VP which was stained with iodine for 60 seconds and thus appears light gray. The two x-ray diffraction patterns shown in Fig. 3.9 were taken right after the roll casting (A) and after a 7 day anneal at 120°C (B). The anneal leads to a substantial increase in the long range order which explains the larger number of diffraction peaks (5 vs. 2). (the exposure time was longer for the unannealed sample ~18h vs. 10h). One dimensional intensity vs. scattering angle taken along the horizontal direction yields q_n / q_1 ratios of 1:2:3 indicative of a two layer structure.

3.5.4 A 2D self assembled dielectric crystal with CdSe nanocrystals

The sequestering of nanocrystals in a polymer system where none of the blocks have a natural affinity to the nanocrystals such as the PS-PI system, is achieved through the use of a compatibilizing amphiphilic molecule. Here an amine terminated polystyrene (in one case) was used which has a head group (amine) capable of attaching itself to the nanocrystal and a long tail (PS) soluble in only one of the blocks (PS).

A 2D dielectric crystal of cylinders on an hexagonal lattice was prepared using the following procedure. 0.7g of poly(styrene-b-isoprene-b-styrene) (Vector 4211D Dexco 13.5k-63k-13.5k, PDI<1.05) triblock copolymer with 0.05g amine terminated polystyrene (Mn=2600, P62NH2 Polymer Source) were dissolved in 2ml of toluene and stirred for

15h. A solution of CdSe nanocrystals in toluene was prepared at a concentration of approximately 0.248mol/l. 0.5 ml of this solution was added to the polymer solution and mixed for 24h. An additional 0.5 ml of toluene was then added and the solution was sonicated for 3 minutes to remove traces of cloudiness. The solution was then roll cast at 40RPM, and the resultant oriented film was removed from the steel roller with ethanol after 15 minutes of drying. To further increase the long range order and remove traces of solvent, the film was annealed for 72h at 120C. Fig. 3.10(A) is a bright field transmission electron microscope image of the unstained block copolymer, the contrast in the image is due to the sequestration of the electron dense CdSe nanocrystals into the PS cylinders. The SAXS pattern in Fig 3.10(B) was taken with the incident beam perpendicular to the axis of the cylinders. The pattern shows 5 diffraction peaks indicating long range order in the sample. The position of the q_n / q_1 peaks occur at $\sqrt{1}$, $\sqrt{3}$, $\sqrt{4}$, $\sqrt{7}$ corresponding to an hexagonally packed cylindrical morphology. The halo observed at larger q is an indication of the good dispersion of the dots (this peak corresponds to the first maximum of the single dot form factor). The incorporation of the nanocrystals selectively into the PS domains is due to the compatibilizing effect of the amine terminated polystyrene oligomer which should be contrasted to the situation in Appendix D, Fig. D.1 showing large scale aggregation in the absence of the end functionalized oligomer.

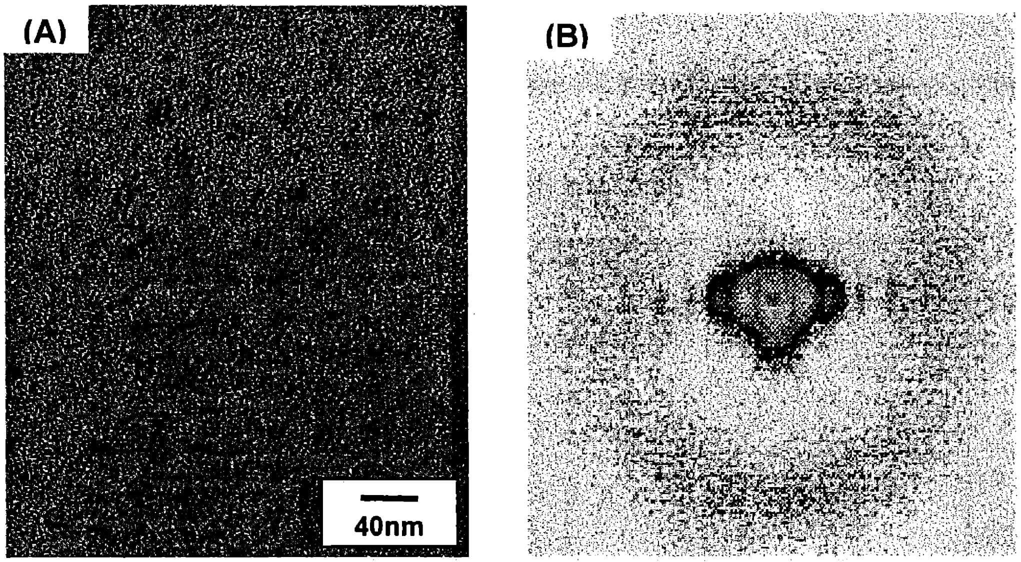

Figure 3.10 (A) Bright field TEM image of an hexagonal array of PS cylinders in a PI matrix. The contrast in this image is due to the sequestering of the CdSe nanocrystals into the PS cylinders. (B) SAXS pattern of the above structure showing high orientation and long range order. The broad halo results from the form factor peak of the CdSe nanocrystals having a radius of 3nm.

3.6 A 1D self-assembled block copolymer photonic crystal

In this section the concepts and methodology described above were applied to a particular block copolymer system made of PS-PI (194k:197k). By enhancing the domain spacing through the use of lower molecular weight components a self assembled multilayer structure is formed. Thus demonstrating the feasibility of forming a self assembled photonic crystal corresponding to the visible portion of the spectrum.

3.6.1 Band calculations for the 1D PS/PI system.

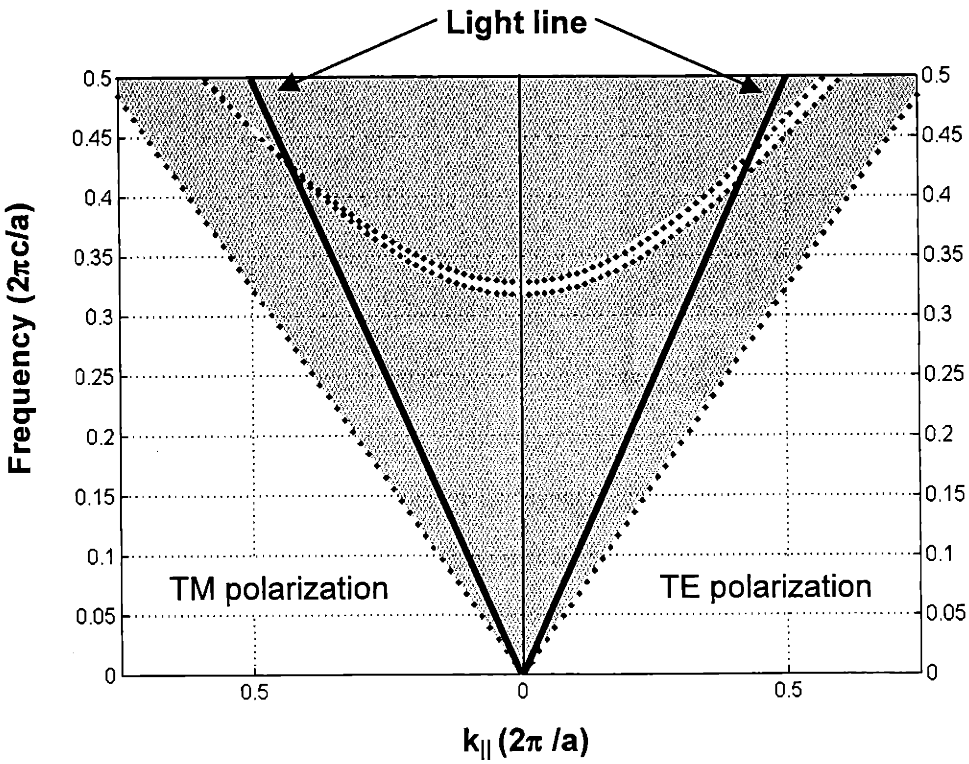

Figure 3.11 Band frequency vs. parallel wave vector for a periodic layered structure (period=a) calculated with the PS-PI optical parameters, for both independent TM and TE polarizations. The light line is superposed on the band structure.

Fig. 3.11 represents a band diagram for a periodic multilayer system with indices of refraction of 1.51 and 1.59 and equal optical thickness. The bands are projected onto the $k_{II} - \omega$ plane. The mirror symmetry about the plane of incidence (defined by the normal to the layers and the k vector) implies the classification of solutions to either transverse electric (TE, electric field perpendicular to the plane of incidence) or transverse magnetic (TM, electric field in the plane of incidence). The propagating modes of the system are shown in gray and the forbidden modes in white. Also on the figure is the light line. The small extent of the band gap (~4%) and the substantial (~30% for the TE mode) increase of its center frequency as a function of increasing k_{II} from its initial position at $k_{II} = 0$, $\omega_{midgap}(k_{II} = 0) = 0.325$ to a value of $\omega_{midgap}(k_{II} = 0.425) = 0.425$ at the crossing of the band with the light line implies a large angular sensitivity of the reflectivity band. This behavior is typical of systems with small refractive index contrast and is very different from the behavior of the system described in Fig. 2.2 (B) which exhibits a substantial angular insensitive set of frequencies in the band gap regime.

3.6.2 Fabrication

A self assembled 1D photonic crystal with a gap in the visible portion of the spectrum, made of a poly(styrene-b-isoprene) (PS-PI) symmetric diblock copolymer (197kg/mol for the isoprene and 194kg/mol for the styrene) was constructed. 0.090g of a 10.0% by volume solution of the diblock in styrene was cast onto a 25mm diameter polished silicon wafer (Silicon Inc.). The solvent was allowed to evaporate for 15 minutes and then covered with a 25mm glass cover slide (VWR #2, 83% solvent content by volume when covered). The weight of the sample as well as the normal incidence reflectivity as a function of radial distance were monitored every 12h.

As the solvent evaporated, an intense concentric ring pattern of colors developed. The first detectable blue color ring appeared at the outer perimeter of the sample after 2-3h and subsequently the blue ring moved inward and encompassed a larger radial thickness, eventually the blue region encompassed the center and the area near the perimeter appeared less reflective because of surface defects.

3.6.3 Morphology

A cross sectioned SEM micrograph (JEOL 6320) imaged in secondary electron scattering mode (accelerating voltage of 4.5kV) of the structure is presented in Figs. 3. 12 (A) and (B) at x7,500 and x13,000 magnifications. The cross section was prepared by immersing the sample in liquid N_2 for 10 minutes then fracturing along a prescribed line while in the cryogenic liquid. The sample was subsequently stained in OsO_4 for 20 minutes and sputter coated with approximately 50nm of Au-Pd. The light stripes in the micrograph are the osmium stained polyisoprene layers which appear bright due to the enhanced generation of secondary electrons by the osmium, while the dark regimes are polystyrene layers. The structure shown in Fig 3.12 is lamellar with the layers preferentially lying parallel to the glass substrate (the glass is shown in white at the left boundary). Edge dislocations as well as waviness are clearly evident in the x13k magnification. The total thickness of the film was approximately 20μm with a period of approximately 110nm.

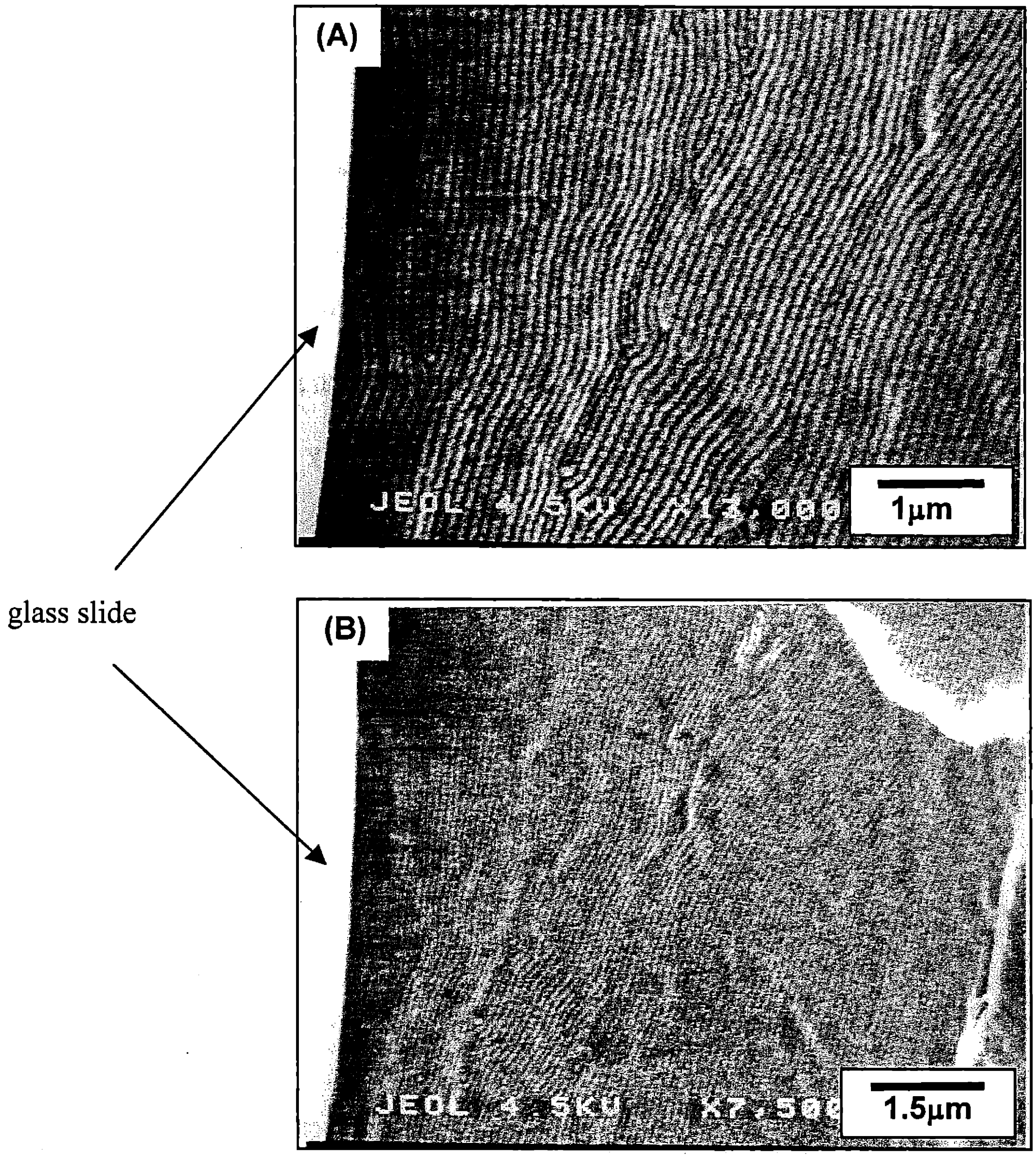

Figure 3.12 SEM micrographs at x13,000 magnification (A) and 7,500 magnification (B) of a near top surface cross section of the SI structure showing alternating layers of styrene (light) and isoprene (dark) the isoprene phase is stained with osmium tetroxide for 20 minutes. Total film thickness is approximately 15µm.

3.6.3 Optical response

The reflectivity of the sample was measured using a Cary 5E spectrophotometer equipped with a diffuse reflectance accessory. The background measurement was a reflectance standard (Labsphere SRS.90.010) calibrated against a NIST standard to have >98.5% reflectivity from 350nm – 700nm with a standard deviation < 0.05%. A 4mm diameter aperture was used for both the sample and the reference. Both were placed at equal distances from the detector by inserting a glass cover slide on the reference sample similar to the one used to cover the sample. Values of reflectivity vs. wavelength at different radial positions on the sample are presented in Fig. 3.13. The measurement was taken 62 hours after casting.

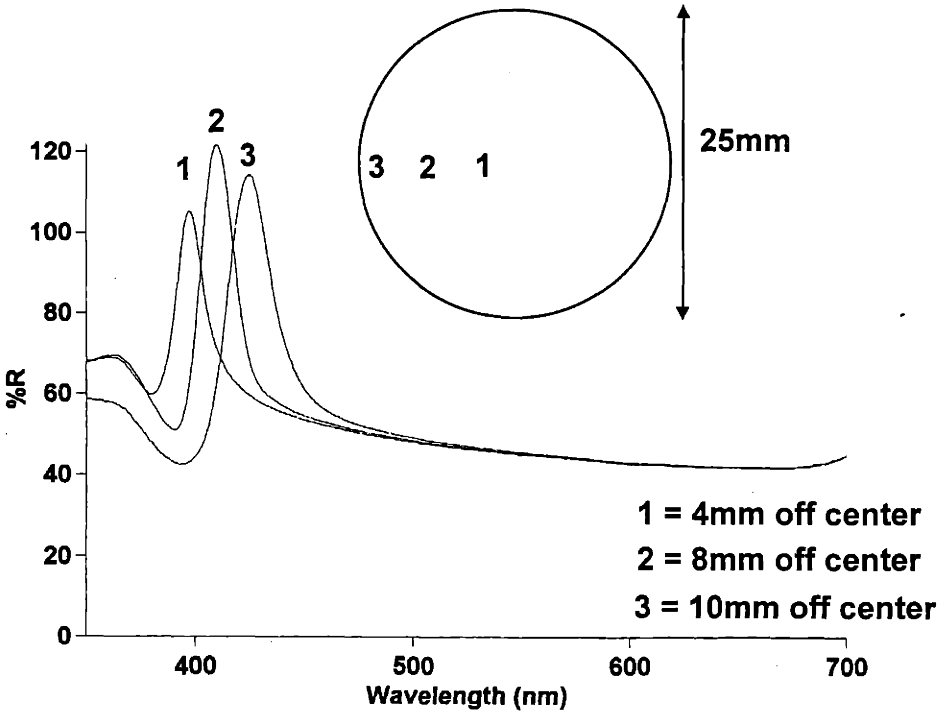

Figure 3.13 Near normal reflectivity as a function of wavelength for an PS-PI multilayer mirror at three different radial positions. A schematic of the sample shows the regimes used to record the spectra.

The maximum reflectivity value is achieved at a position located 4mm off the center (this maximum is the maximum value achieved for any point at all times). The reflectivity shifts to shorter wavelengths as the center is approached. The average solvent content (in volume %) in the sample at 62h is 30% while the value from simulations at the center is ~65% (see Fig. 3.16).

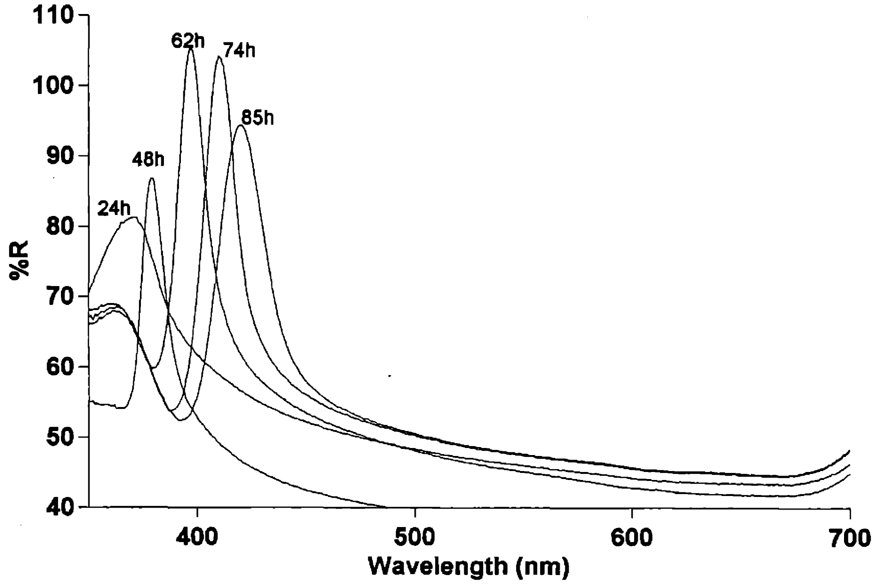

Figure 3.14 Center reflectivity as a function of wavelength for a PS-PI multilayer mirror at 24h 48h, 62h, 74h, and 85h after casting showing a maximum in reflectivity at 62h.

The reflectivity of the sample center as a function of time after casting is presented in Fig 3.14. The maximum reflectivity value and its wavelength both increase as a function of time until 62h, while the FWHM over peak wavelength decreases. After that time, the reflectivity begins to drop and the FWHM over peak wavelength increases.

Time (hours)	0 h	12 h	22 h	37 h	48 h	62 h	74 h	85 h
Measured average solvent concentration (volume %)	83%	65%	57%	46%	36%	30%	26%	22%

Table 3.1 Measured average solvent volume concentration at different times.

It is useful to distinguish between the macroscopic and microscopic behavior of the system. Macroscopically, the system undergoes a transition from a state where the two glass plates are held together by the surface tension of a low concentration polymer (initially 17% polymer concentration Table 3.1) solution to a state where the glass plates are essentially glued together by the polymer (78% polymer concentration). The polymer concentration in the binding layer increases as a function of radial distance and time. It is expected that the force binding the two glass plates will increase in a similar fashion since as the outer polymer dries the shrinkage will exert a large force. Over time, this drying force leads to an increase in the pressure inside the sample due to the larger force and larger area over which the force is applied. Microscopically, the system transitions from a disordered solution confined between two glass plates to an ordered layered system with the layers preferentially parallel to the glass surfaces.

Microscopic behavior at short times (1-12h):

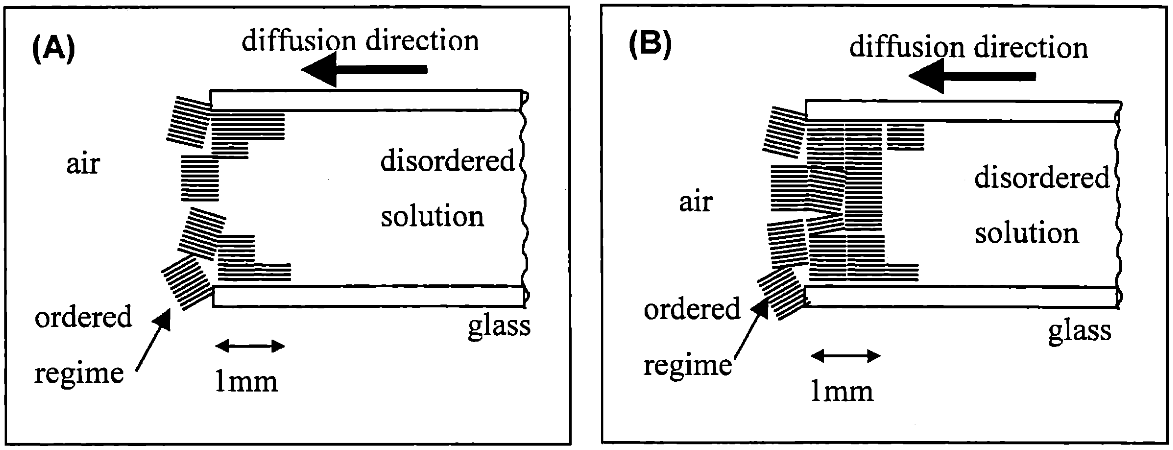

Figure 3.15 Schematic of sample edge region (A) 1h after casting and (B) 12h after casting (B).

In all of the discussion it is assumed that styrene is a non-preferential solvent with respect to the two blocks and is therefore equally distributed between the phases (Skoulios, A.E., 1972). As the styrene monomer ($n_{styrene} = 1.54$) evaporates, the index contrast and the effective interaction parameter χ of the different micro-separated phases both increase. The outer perimeter of the sample is in contact with the air and thus has the lowest solvent concentration at every given moment. Thus it is expected that this region will undergo ordering first, indeed an intensely blue ring develops at the sample perimeter approximately 1h after the sample is cast as shown in Fig. 3.15 (A) indicating that the polymer concentration is above the disorder to order transition. During this time frame there is little reflectivity from the sample center indicating that the sample center did not yet undergo the ordering transition. As the solvent concentration decreases the order-disorder concentration front moves radially inward encompassing a larger radial extent Fig 3.15 (B).

Intermediate time behavior (12-62h):

The layers nucleated at the perimeter grow inward as a function of time due to continual solvent diffusion and the gradual transition from disorder to order which explains the inward movement with time of the initially outer blue ring. The magnitude of reflectivity goes through a maximum at any given location on the sample. This indicates the presence of two competing effects: one leading to an increase in reflectivity which grows in time and the other which tends to diminish the reflectivity as a function of time. The increase in reflectivity is probably effected by the increase in the index of refraction contrast between the layers with the loss of styrene monomer but is due primarily to an increase in the ordering of the layers between the two glass plates. The scaling of the reflectivity cannot however simply be accounted for by assuming a fixed number of layers and varying the index in accordance with the prediction based on the average concentration. The reflectivity should vary with index ratio according to:

$$\ln n = \frac{1}{2N}\ln\left(\frac{1-R^{1/2}}{1+R^{1/2}}\right)-\frac{\ln\alpha}{2N}, \tag{3.2}$$

where R is the reflectivity, n is the ratio of indices of refraction[1], N is the number of periods and α is the index ratio of the ambient and substrate. What is observed is an increase in reflectivity which exceeds the amount due merely to index increase which implies an increase in the number of ordered layers at a given radial distance.

---

[1] $n_{PS} = 1.59,\ n_{PI} = 1.51,\ n_{styrene} = 1.54$

To account for the radial and temporal dependence of the reflectivity, a detailed study of the morphology evolution and solvent distribution is required. In the absence of the detailed model a number of observations will be made based on the current state of measurements. Taken in context of a simplified solvent distribution model will provide a plausible framework for explaining the observed data.

Modelling the solvent loss:

A schematic of the system is shown in Fig. 3.16,

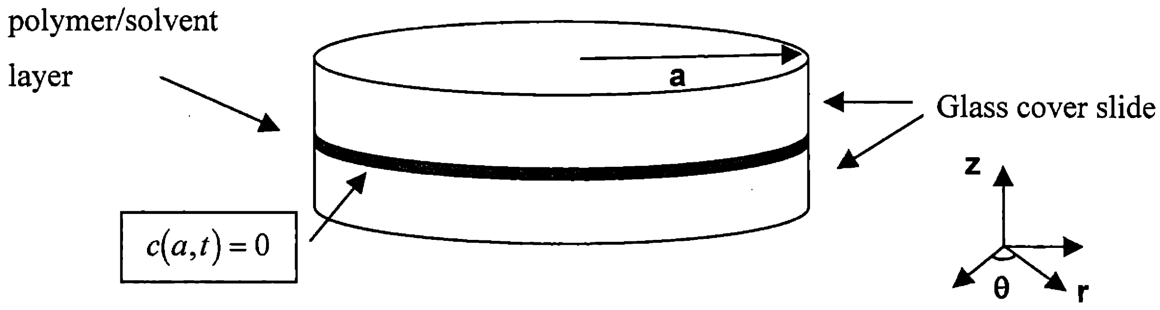

Figure 3.16 Schematic of the system, showing the solvent containing polymer layer between two glass cover slides of radius a.

To estimate the concentration at the sample center as a function of time the non-steady state diffusion equation was solved in cylindrical coordinates. The thickness of the organic layer (polymer with solvent) is much smaller (~100μm) than its lateral dimension (~10mm) and is confined from above and below by impermeable glass boundaries (zero flux conditions at the boundaries). It is reasonable therefore to assume that there is no z dependence of the concentration. The cylindrical symmetry implies a θ independence of the concentration,

$$\frac{\partial c(r,t)}{\partial t} = D\nabla^2 c(r,t) \qquad (3.3)$$

subject to the conditions,

$$\begin{aligned} c(a,t) &= 0 \\ c(r,0) &= c_0 \end{aligned}, \tag{3.4}$$

The solutions of the Laplacian in cylindrical coordinates in the absence a θ dependence are Bessel functions of the first kind,

$$c(r,t) = c_0 \sum_{n=1}^{\infty} \frac{2}{\alpha_n J_1(\alpha_n)} J_0(\alpha_n r) e^{-D\alpha_n^2 t} \tag{3.5}$$

where r is the normalized radial coordinate, α_n is the nth zero of the Bessel function and D is the diffusion constant[1].

The mean diffusion constant is found by calculating the flux at the boundary (r=a) as a function of time and integrating from t=0 to the time of weight measurement.

The flux is obtained by calculating the gradient of the concentration and using the known properties of the differentials of Bessel functions (Abromowitz and Stegun 1972).

$$J_{\hat{r}}(1,t) = -D \frac{d}{dr} c(r,t) \Big|_{r=1} \tag{3.6}$$

$$J_{\hat{r}}(r,t) = -Dc_0 \sum_{n=1}^{\infty} \frac{1}{J_1(\alpha_n)} \left[J_{-1}(\alpha_n r) - J_1(\alpha_n r) \right] \Big|_{r=1} e^{-D\alpha_n^2 t}, \tag{3.7}$$

which can be simplified to yield the following form,

$$J_{\hat{r}}(1,t) = Dc_0 \sum_{n=1}^{\infty} J_1(\alpha_n) e^{-D\alpha_n^2 t}, \tag{3.8}$$

The total volume loss is obtained by integrating the flux expression,

---

[1] It is assumed that D is concentration independent, clearly a wrong assumption. What is calculated therefore is a mean diffusion constant which is the answer to the following question: given a measured weight loss until time t what is the constant D that will yield an identical loss value for the same time frame. This assumption gives a lower bound to the diffusion constant.

$$m = 2\pi \int_0^t J_{\hat{r}}(1,t)dt = 2\pi c_0 \sum_{n=1}^{\infty} \frac{1}{\alpha_n^2} J_1(\alpha_n)\left(1 - e^{-D\alpha_n^2 t}\right) , \qquad (3.9)$$

Before these equations can be solved, the diffusion constant needs to be calculated. Integrating Eq. 3.5 over the sample volume yields the average concentration at time t, with the only unknown being the effective diffusion constant – D (since the concentration was measured as a function of time). The calculation was carried out numerically using the first 50 harmonics of the J_0 function.

The calculated values of the effective diffusion constant are summarized in table 3.2 and graphically in Fig. 3.17

Time(hours)	12h	22h	37h	48h	62h	74h	85h
Diffusion constant $\times 10^{-3}\left[h^{-1}\right]$	0.935	1.09	1.36	1.85	1.90	1.95	2.0

Table 3.2 Effective diffusion constant calculated by integrating to different times.

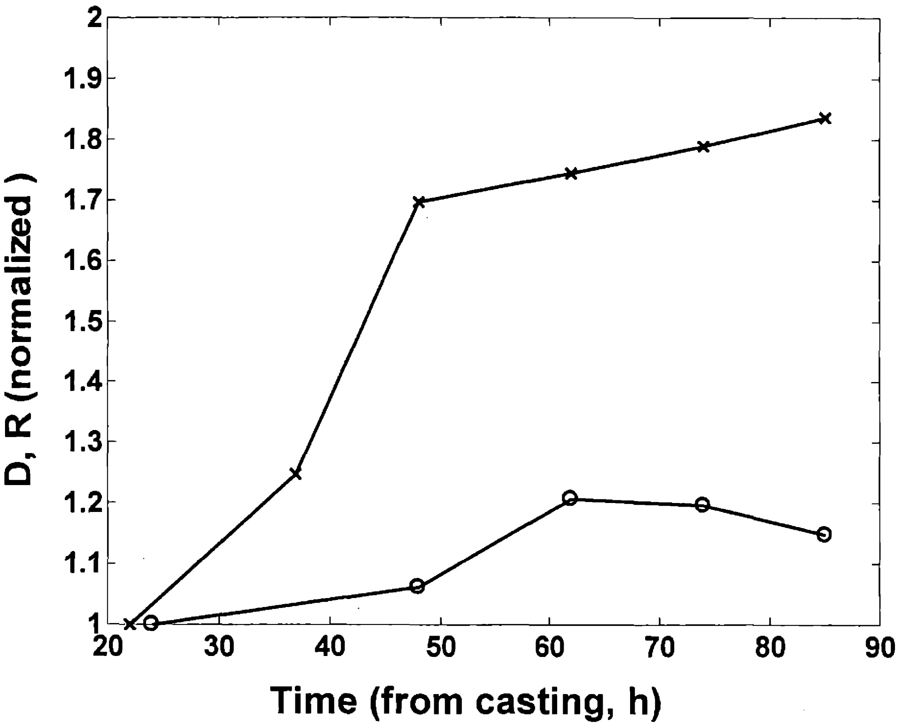

Figure 3.17 Effective diffusion constant (x) and magnitude of reflectivity (o) (at the sample center) as a function of time.

Shown in Fig. 3.17 are the peak reflectivities at the sample center and the mean diffusion constant calculated by integrating the flux to different times. The values were normalized (for comparison) to the lowest value. The mean diffusion constant increases monotonically as a function of time, the rate at which the diffusion constant increases reaches a maximum somewhere between 40-50h. The reflectivity reaches a maximum at 62h[1] and then begins to decrease.

---

[1] The reflectivity at the sample edge peaks at 62h as well.

It is quite surprising that the effective diffusion constant increases with decreasing amount of solvent since as the solvent evaporates, the polystyrene will eventually go through its glass transition. This decrease in chain mobility will then lead to a decrease in the diffusion constant. The increase in the effective diffusion constant serves as an indication of the presence of a force field which as mentioned above is exerted by the drying polymer on the glass slides; the initial force which the dilute polymer exerts on the glass slides is small. As the polymer concentration increases, the force increases as well as the area over which the force is applied both increase leading to an increase in pressure as a function of time. This provides a plausible explanation for the observed increase in the effective diffusion constant.

The estimated concentration profiles are plotted in Fig. 3.18. On the left is a typical short time concentration profile calculated at 12h (an initial concentration of 0.83 was assumed). and on the right is the estimated profile at 62h (intermediate times).

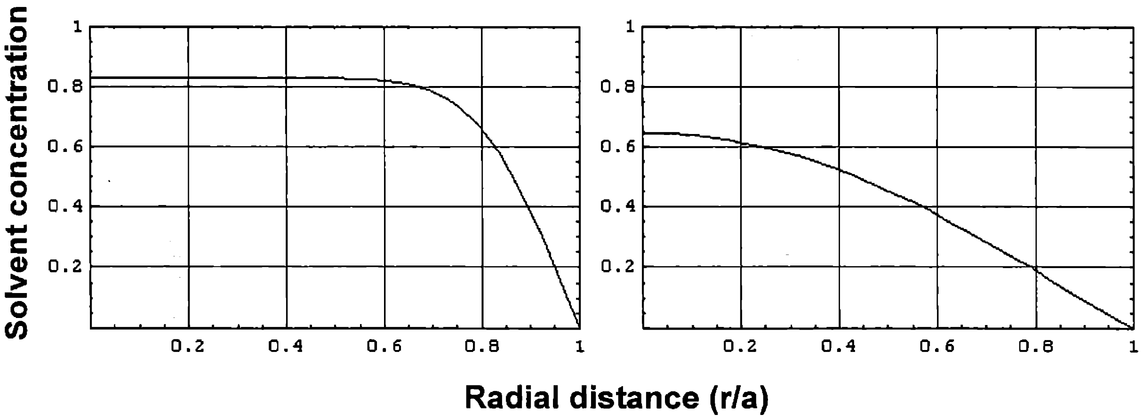

Fig 3.18 The concentration profile at 12h (left) 62h (right) as a function of radial distance.

The diffusion constant at 12h and 62h (Table 3.2) was used to calculate the corresponding solvent concentration as a function of the radial distance (normalized to the radius) shown in Fig. 3.18. At 12h the concentration up to r=07 is relatively unchanged which explains the initial absence of reflectance at the sample center.

Fig. 3.14 shows an increase in the peak wavelength corresponding to an increase in the domain spacing with increased polymer concentration. As the solvent evaporates the repulsive interaction between the blocks which was screened in the presence of the solvent increases (difference between the interaction parameter $\chi = z/kT(\varepsilon_{AB} - 1/2(\varepsilon_{AA} + \varepsilon_{BB}))$,of the blocks increases) leading to an increased segregation tendency. The interpenetration of the dissimilar blocks is minimized and the overall end to end of the chain distance increases. The decrease in conformational entropy is balanced by the reduction in mixing free energy[1]. A similar observation of the domain size increase with increase polymer concentration was made by Shibayama (Shibayama M., *et al* 1983). There, as in our case a neutral solvent was used. In Shibayama's experiments, the period spacing regardless of the solvent concentration was less then the equilibrium spacing of the polymer. In our case the periods of the solvent-polymer appear to be above the equilibrium spacing of the pure diblock. As drying proceeds, the chains are stretched due to the constraint imposed by the glass plates. As the Tg of the PS passes through room temperature due to the loss of the solvent at the periphery of the discs, the plate separation becomes fixed. Since the junctions are no

---

[1] Shibayama documents and explains the increase in spacing with decrease of solvent content in a symmetric PS-PI block copolymer with a neutral solvent, though the maximal length approached in his case was the equilibrium length. In our case the domain spacings that are far above the equilibrium layer spacing and are strongly influenced by the spacing between the rigid glass slides.

longer able to move laterally to allow the chains to reduce their end-to-end distance. Thus the structure assumes a non equilibrium spacing which is above that of an unconstrained system.

The last issue to be addressed is the increase in reflectivity to a maximal value in time as shown in Figures 3.14 and 3.15. As stated above the maximum at intermediate times indicates the presence of two competing effects, the increase is due to the increase in order which is caused by solvent evaporation and the increase in number of layers and removal of bulk defects. As the chains continue to stretch and apply a force on the glass plates partial de-wetting occurs and surface defects form which tend to diminish the reflectivity.

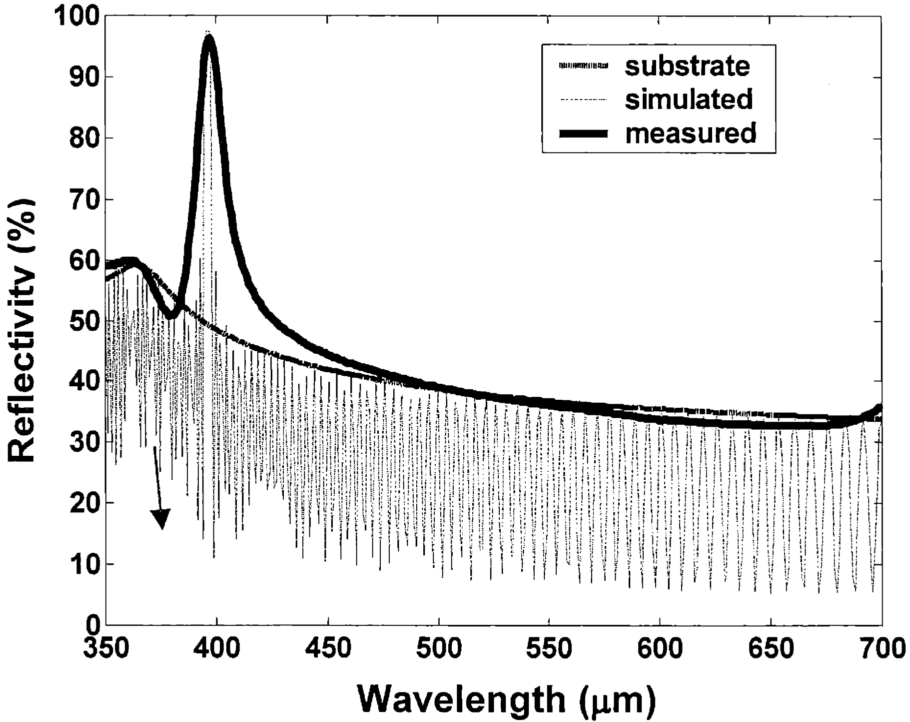

Figure 3.19 Measured (thick line) and simulated (thin line) reflectivity. The simulation is for a 75 period multilayer system, with sinusoidal index function and a period of 128.2nm. A value of 64.8% solvent content equally distributed between the phases was used in the simulations. Superposed is the simulated reflectivity of the silicon substrate (dotted).

The measured reflectivity[1] is compared in Figure 3.19 to a simulation using a 75 period sinusoidal index function. Since the calculated solvent concentration at the sample center is high (64.8%) as shown in Fig. 3.18 the PS-PI blocks are expected to be weakly segregated resulting in interpenetrating chains that will induce a variation in the index of refraction function which is approximately sinusoidal. The period distance was taken to be 128.2nm[2]. The index of refraction used in the simulation was determined by the values of the respective polymers ($n_{PS} = 1.59\,, n_{PI} = 1.59$) and by the polymer concentration at the sample center (64.8%) at the time of measurement as calculated by Eq. (3.5) using the calculated diffusion constant from Table 3.2. The silicon substrate was modeled using published values for real and imaginary part of the index of refraction (Palik, E. D., 1998). The measured value was taken from the center measurement at 62h (Fig 3.15) and normalized to the simulated value.

The position and magnitude of the center peak correlates well with position of the simulated peak for the number of periods chosen and the index contrast. FWHM of the measured peak is 14nm and that of the simulated peak is 3.5nm. The experimental peak broadening is most likely due to the variations in solvent concentration and corresponding thickness variation across the measured area (~4mm). In the simulated data, high frequency oscillations appear in the out-of-gap regimes which are due to the

---

[1] When compared to the reference a reflectivity value of >100% was measured. This indicates a reflectivity value that is probably very close to the reference (>98.5%). To compare with simulation the measured value was scaled down arbitrarily to 96%.

[2] The position of the center peak has a sub nanometer sensitivity a shift in 0.5nm in layer thickness will induce a (0.5/64)*400=3.1nm shift in the peak center position this is considerablyy above the 1nm resolution of the Cary 5E!.

finite nature of the dielectric crystal. The number of the oscillations is related to the number of periods, while their magnitude is a function of the gradient of the dielectric function at the boundary between the structure and the substrate. Gradual transitions of the dielectric function at the boundary result in the removal of the oscillations[1]. The absence of these oscillations in the measured data is due to the frequency of oscillation, which is high and difficult to detect. In addition these oscillations are very sensitive to the exact position of the interfaces unlike the band gap which is primarily determined by the average interfacial spacing. Any fluctuation in the thickness of the periods mitigates the oscillations.

3.6.4 Tailoring the period by varying the homopolymer content

Blending a lower molecular weight component miscible in one or both of the phases can control the domain spacing of a block copolymer and its corresponding photonic band gap. The PS-PI (194k:197k, PDI=1.02) block copolymer mentioned above was blended with homopolymer styrene (13k PDI =1.04) and homopolymer isoprene (13k, PDI=1.06) using solutions of 0.1g/ml in styrene. The samples were prepared by adding equal amounts of homopolymer styrene and homopolymer isoprene while varying the total volume fraction of homopolymer with respect to the diblock copolymer. Four samples were prepared following the procedure outlined in the previous section. The first sample was pure diblock copolymer (0% homopolymer), the others had 19%, 32, 45% homopolymer content. The reflectivity at the sample's center after 62h from casting is presented in Fig. 3.20.

---

[1] A quintic refractive index profile is used to reduce Fresnel reflection losses by providing a ramp matching of the dielectric function of the structure to that of the substrate.

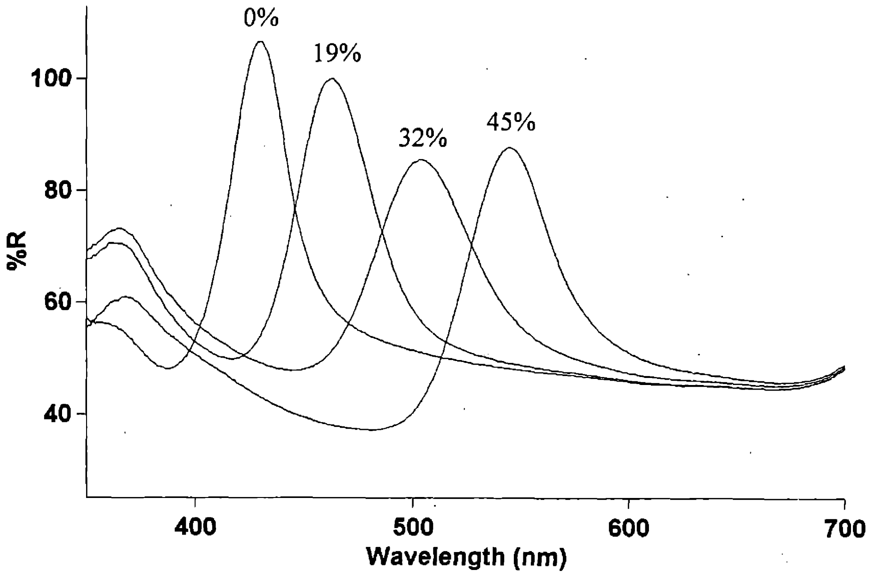

Figure 3.20 Reflectivity vs. wavelength for diblock copolymer swollen with equal amounts of homopolymer styrene and homopolymer isoprene, the different peaks correspond to different volume fractions of homopolymer content.

The position of the maximum reflectivity peak increases in wavelength as the amount of homopolymer is increased, indicating the swelling of the block copolymer phases. The magnitude of the maximum reflectivity value decreases as a function of homopolymer content and a broadening of the peak is observed[1] due probably to the formation of defects (homopolymer pooling).

3.6.5 Angular measurements

The photonic band structure of a multilayer system with small indices of refraction predicts a high degree of angular sensitivity of the band gap, as the angle of incidence increases the position of the band gap shifts to higher frequencies.

A multilayer PS-PI sample was prepared as outlined in the previous section with a total of 45% homopolymer content. The reflectivity as a function of angle was measured after 80h from casting using the Cary 5E fitted with a variable angle specular reflectance accessory (VASRA by Varian Inc), and a polarizer (TE modes probed). Results of the measurement at 20°, 40°, 50°, 60°, 65° and 70°, as well as a simulation for the corresponding angles are presented in Fig. 3.21.

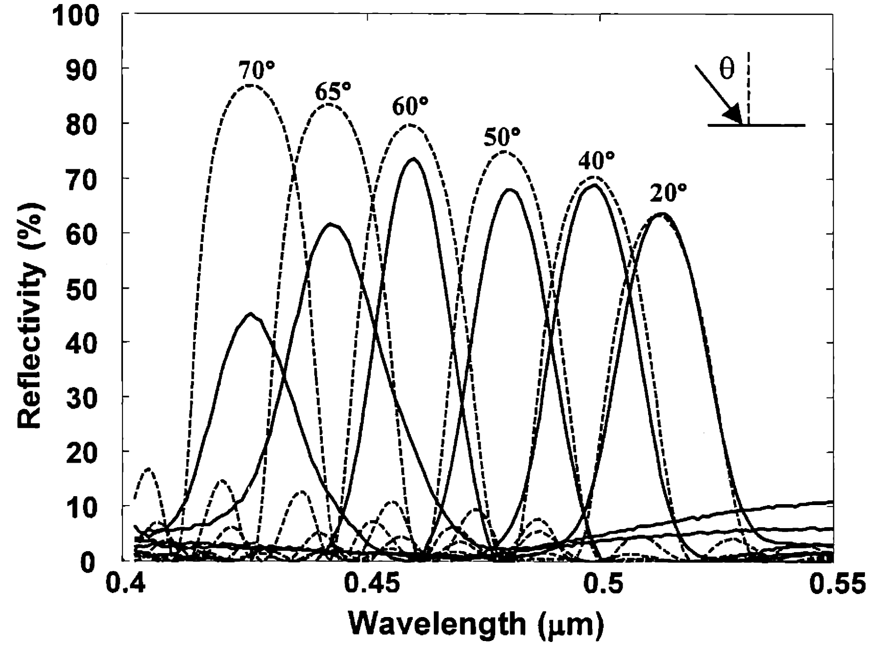

Figure 3.21 Measured (dotted curves) and calculated (solid curves) TE reflectivity as a function of wavelength at various angles of incidence for a PS-PI/hPI/hPS blend at a ratio of 6/2.5/2.6 taken 8mm from the center with the Varian VASRA 80h after casting. The simulations assume 27 layers and a solvent content of 30% equally distributed between the phases.

The shift in the position of maximum reflectivity with angle of incidence nicely matches the prediction. The magnitude of the reflectivity is expected increase for this polarization

---

[1] Above the broadening that is expected as wavelength increases determined by the constant value of the gap over midgap ratio.

(TE) the measurements indicate this at low angles of incidence. The decrease in measured reflectivity at higher values of incidence is due to the spread of the measurement beam and the radial variation in the sample (using larger samples will eliminate this).

3.7 A 3D self-assembled block copolymer photonic crystal

3.7.1 Introduction

In the previous section it was demonstrated that adding equal amounts of homopolymer leads to a domain swelling this in turn was used to obtain a control over the spectral position of the band gap in a lamellar photonic crystal. In this section the relative amount of homopolymer is varied leading to the formation of a three dimensional photonic crystal.

3.7.2 Fabrication

The sample was prepared by adding 50% by weight homopolymer polystyrene (13k) to the PS-PI diblock copolymer (194k:197k) described in section 3.6.2. The sample was cast from a 10% weight solution in styrene onto two 25mm glass cover slides (VWR #2) which were rubbed with a velvet cloth to induce preferential orientation. After approximately 24h a blue/green color developed which did not change when viewed at different angles. The sample was annealed at 120°C for 72h the optical quality of the film did not change dramatically upon annealing (no cloudiness or surface defects observed).

3.7.3 Morphology

An SEM image of the cross section of the sample is presented in Fig. 3.22 (the sample was prepared according to the procedure outlined in 3.6.3).

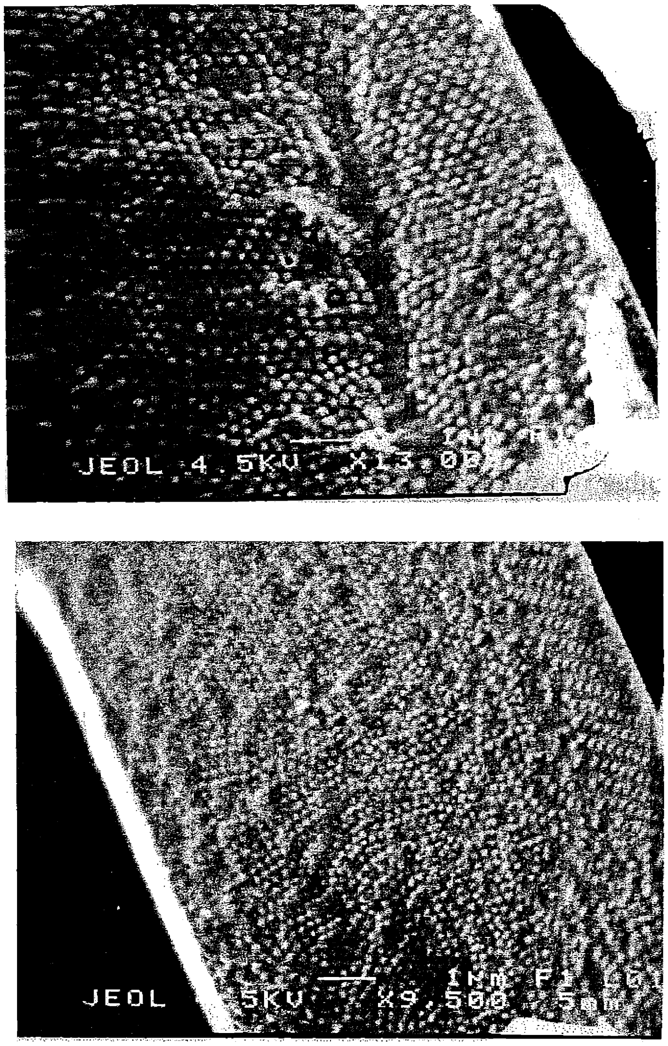

Figure 3.22 SEM micrographs of a cross section of an PS-PI diblock copolymer (194k:197k) swollen with 50% styrene homopolymer (13k) showing an array of spheres, the isoprene phase appears light is stained with osmium tetroxide for 20 minutes.

The images in Fig. 3.22 are of polyisoprene (stained with osmium and appear lighter due to enhanced electron scattering from the heavy osmium atoms) spheres in a polystyrene matrix. As shown there is a lack of long range order across the film, though short range ordering which appears to be on an FCC lattice is evident. This is a first demonstration of the ability to achieve morphologies other than the lamellar which interact with visible light by swelling a symmetric diblock with unequal amounts of homopolymer (in this case only homopolymer polystyrene was added). Using this approach work is currently in progress to achieve other morphologies using higher molecular weight homopolymers.

3.7.4 Optical response

The reflectivity of the sample as a function of wavelength is presented in Fig. 3.21 at near normal incidence as measured on a Cary5E spectrophotometer fitted with an integrating sphere.

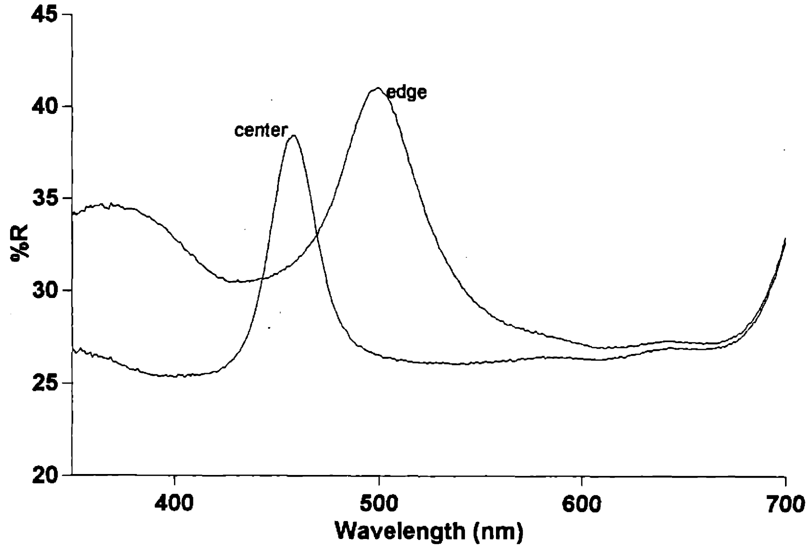

Figure 3.23 Reflectivity as a function of wavelength for the polyisoprene spheres structure at two different radial positions.

The reflectivity spectra exhibits the same characteristic shift to longer wavelengths as a function of radial position as the layered sample see Fig 3.14. The maximum reflectivity in this sample is substantially lower than in the layered structure which may be due to the abundance of defects seen in Fig. 3.22. and to the smaller total sample thickness which is approximately 10μm. An insensitivity of the reflectivity to angle of view was visually observed though not quantitatively measured for this sample. This is another indication of the higher dimensionality of periodicity and the existence of photonic gaps in more than one direction[1].

This structure is a first attempt at demonstrating the applicability of our approach to the fabrication of photonic crystals of higher dimensionality. Work is in progress to increase the long range order of this sample and better characterize the morphology.

---

[1] See Appendix F for band diagram of the 2D cylinders for similar index contrast and compare with Fig. 3.11.

3.8 Defects in BCP

Defects play a crucial role in photonic crystals, certain types of imperfections in a photonic band structure could lead to localized electromagnetic states, such that a point defect could act as a microcavity, a line defect like a waveguide (Mekis A., Chen J. C. *et al,* 1996).

Depending on the microdomain geometry, various point, line and surface defects can occur during the transformation from the homogeneous disordered state to the microphase separated state. For example, in spherical microdomain block copolymers planar stacking faults on {110} planes are commonplace as well as high angle grain boundaries. In cylindrical microdomain block copolymers, two types of edge dislocations are common. It is quite likely that some of these imperfections will have interesting photon transport and localization properties. By tuning the shape, size and topology of the defects, control over the symmetry properties of the electromagnetic modes is possible (P. R. Villeneuve, S. Fan, J. D *et al,* 1996). An example of a grain boundary surface imperfection in a cylindrical microdomain sample is shown in Fig. 3.8.

The challenge that remains is tailoring the dimensionality and position of the defects. One possible way to control the positions and structure of the defects is by creating heterogeneous nucleation sites such as by patterning a substrate to include ridges or elevated posts (Fasolka M., Harris D. J. *et al,* 1997). The self assembly process then leads to the formation of defects at such predetermined sites during the disorder to order transition.

Chapter 4: Guiding light through an all-dielectric hollow waveguide

4.1 Introduction

Guiding light in dielectric fibers has had a tremendous impact on many aspects of our life – we rely on fiber optics for communications as well as for illumination and a host of medical applications. The typical optical fiber has a high index core and a low index cladding such that the light is confined to the core by total internal reflection. Two inherent drawbacks exist in this approach: The first is absorption. Since the light is travelling through a dense medium for long distances, material absorption becomes significant even in low loss materials. To compensate for losses the fiber is doped with erbium which is used to amplify the signal. This in turn limits the effective band width of the fiber to that of the narrow erbium excitation lines. The other weakness follows from the confinement mechanism – total internal reflection which confines light only of a limited angle. Conventional optical fibers cannot guide light around sharp turns, which is especially important in optical integrated circuits. Light guided in a hollow waveguide lined with an omnidirectional reflecting film propagates primarily through air and will therefore have substantially lower absorption losses. In addition, the confinement mechanism does not have angular dependence allowing for guiding light around sharp bends with little or no leakage.

Most hollow waveguides fabricated to date (Miyagi M. *et al,* 1983, N. Croitoru *et al,* 1990, Y. Matsuura *et al*, 1997) have internal metallic and dielectric layers, it has been shown (Miyagi M., Kawakami S., 1984) that the addition of dielectric layers to a metallic waveguide could lower the losses significantly. In contrast our system, is an all dielectric waveguide which confines all frequencies contained in its omnidirectional range. In principle this type of structure can have lower losses than the combined metal and dielectric structure since the waves do not interact with a lossy metallic layer. Although our proof of concept demonstration involves a large diameter multimode waveguide, one can fabricate a much smaller tube that could in principle be made to support a single mode.

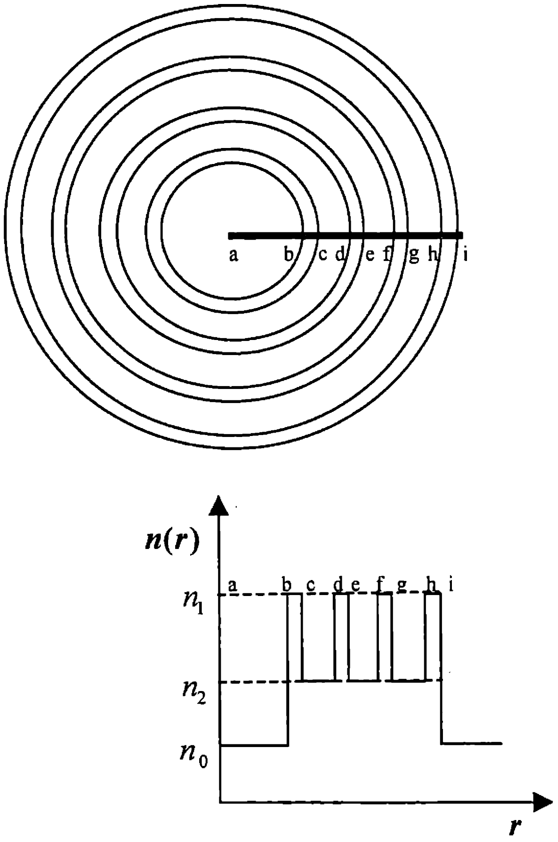

Figure 4.1 Cross section of the hollow waveguide showing the hollow core and the dielectric films, also shown is the index of refraction profile in the radial direction.

A schematic of the hollow tube is presented in Fig. 4.1, as well as the index of refraction profile. In a realistic light guiding scenario involving many bends there exist no global symmetries and thus one cannot distinguish between independent TE and TM modes. Locally one can define a plane of incidence with respect to the normal to the film surface and the incident wave vector. Light entering into such a tube will invariably hit the walls many times and explore a wide range of angle of incidence of both polarizations with respect to any local plane of incidence. Since the air region is bounded by a structure that has a gap which encompasses all angles and polarizations the wave will be reflected back into the tube and will propagate along the hollow core as long as $k_z \neq 0$.

4.2 Fabrication

A Drummond 1.92mm o.d. silica glass capillary tube was cleaned in concentrated sulfuric acid. The first tellurium layer was thermally evaporated using a LADD 30000 evaporator fitted with a Sycon Instruments STM100 film thickness monitor. The capillary tube was axially rotated to ensure uniformity during coating. The first polymer layer was deposited by dip coating the capillary tube in a solution of 5.7g polystyrene DOW 615APR in 90g toluene. The next layer is tellurium deposited in the same method outlined above. The subsequent polymer layers are made of polyurethane diluted in mineral spirits. The device has a total of 9 layers, 5 Te and 4 polymer and a total length of 10cm. The layer thickness are approximately 0.8μm for the tellurium layer (refractive index 4.6) and 1.6μm for the polystyrene and polyurethane layers (refrective index 1.59). An optimal design (Yeh P., Yariv A., 1978) will vary the layer thickness according to the zeros of the Bessel functions. Performance as well as the layer thickness was monitored by IR spectroscopy. The reflectivity of the deposited structure was measured in the radial direction using a Nicolet FTIR microscope and a variable size aperture, to ensure domination by radial reflection. The coated capillary tube was then inserted in a heat shrink tube which was filled with silicone rubber. Finally, the glass tube was dissolved using concentrated hydrofluoric acid (48%). The resulting hollow tube assembly is thus lined with the mirror coating and is both flexible and mechanically stable.

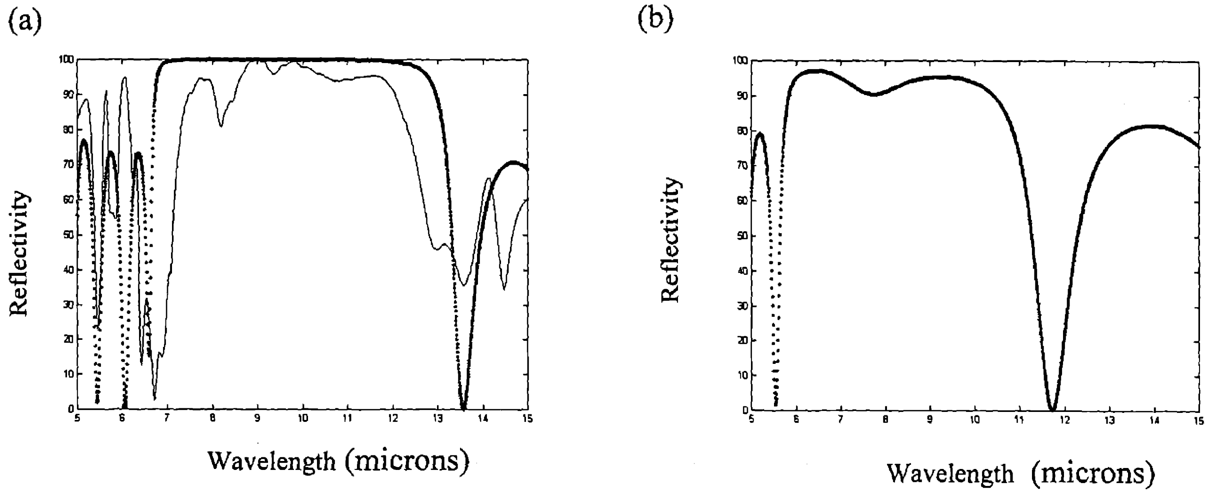

Figure 4.2 (A). Measured (dashed) and calculated (dots) normal incidence reflectance for hollow waveguide in the radial direction. (B) Calculated grazing incidence reflectance for the TM mode.

The reflectance measurements and simulations are shown for normal incidence in Fig. 4.2(A). The measured gap width is smaller than predicted, probably due to microdefects in the Te layers. In addition there are absorption (~8μm) peaks due to the polyurethane. Fig. 4.2(B) is the calculation of the reflectance at grazing incidence for the TM mode. Since the omnidirectional frequency range is defined from above (high frequency edge) by the normal incidence gap edge (arrow) and from below by the grazing incidence gap edge (arrow) the extent of the gap is completely defined by these two data points. The extent of the omnidirectional range for the parameters used in this experiment is approximately 40%.

4.3 Transmission measurement

The transmission through the tube was measured using a Nicolet Magna 860 FTIR bench with an MCT/A detector. The transmission was measured around a 90° bend at a radius of curvature of approximately 1cm, which was compared, to the straight tube transmission to correct for entrance and exit effects. A schematic of the measurement layout is presented in Fig. 4.3.

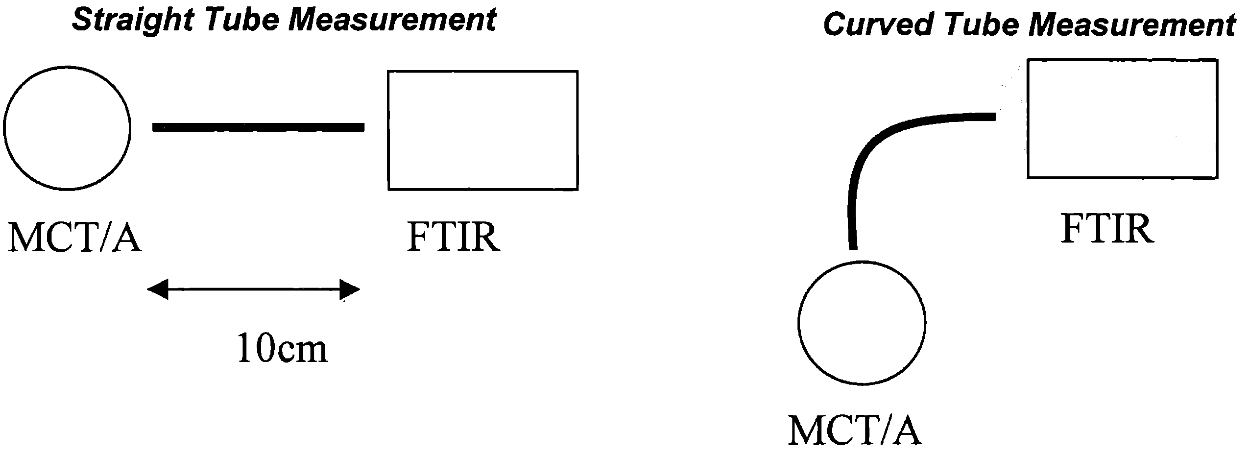

Figure 4.3 Hollow tube transmission measurement setup on the spectrophotometer (FTIR).

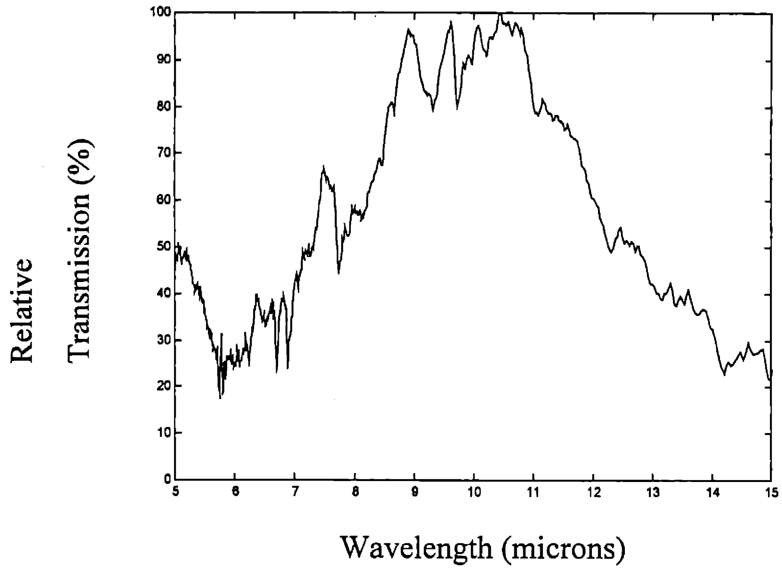

Figure 4.4 Transmission through the hollow waveguide around a 90 degree bend as a function of wavelength.

4.4 Discussion

The results shown in Fig. 4.4 indicate a high transmission around the 90° bend for a spectral band that corresponds to the omnidirectional gap. The relatively high noise level in the measurement is due to the lack of purge. This measurement provides a proof-of-principle indicating the low loss characteristics and guiding abilities of the all dielectric hollow waveguide.

These results open new opportunities for guiding light in a low dielectric media, or even in air. Which can be of importance in cases where material absorption is significant. Two examples are guiding of high power electromagnetic radiation which would otherwise tend to interact with a dense guiding media, or guiding of frequencies which have considerable material absorption – such as CO_2 lasers at 10.6μm.

By reducing the dimensions of the waveguide core single mode propagation is conceivable, which could be utilized for communication at frequencies where glass is not optimized. Other properties of the omnidirectional multilayer structure such as the possibility of obtaining a hierarchy of omnidirectional gaps (shown in Fig. 2.2(B)) allow for additional functionalities to be introduced to a waveguide.

Chapter 5 Confining light in self assembled microcavities

5.1 Introduction

In this chapter a method is outlined for introducing defects of controlled dimensions into a 1D self assembled photonic crystal. By tuning the period of the photonic crystal and the defect size a microcavity structure is constructed which is in resonance with a particular electromagnetic mode. A photoactive material is placed within the defect structure and a modified emission spectra is observed.

Previous studies on modifying the spontaneous emission of active media (K. H. Drexhage 1970, and more recently Tessler *et al* 1996) have focussed primarily on the nature of the active component. The optical confinement in these experiments is provided by conventional dielectric mirrors and metal layers or on processes which involve an elaborate deposition method. In contrast the approach presented here utilizes self assembled structures as the means for providing confinement which can be processed in a variety of ways are structurally conformal and allows for wavelength tunability.

5.2 Background

The system

The system consists of an excited atom placed in a medium. Under certain conditions determined by the electromagnetic mode structure of the medium and the interaction between the medium and the atom, the atom will undergo a transition to a state of lower energy by emitting a photon. First the case where the medium is characterized by a continuum of electromagnetic modes (such as a large vacuum volume) is considered. In the absence of any restrictions on the polarization and direction of the emitted photon the system is free to make a transition from the single initial state (the atom in an excited state) to any one of a continuum of final states (the atom in the lower energy state together with a photon of arbitrary direction). In an irreversible process characterized by a decay time.

The hamiltonian

In order to influence the rate or character of the emission one needs to first identify the basic processes that determine the transition probability.

We will assume that our system is described by a hamiltonian H_0, with no explicit time dependence and a perturbation W(t) which describes the interaction between the excited atom and the medium. H_0 has a spectrum of eigenstates, which include the system's initial discrete state $|\varphi_i\rangle$ associated with an eigenvalue E_i and a continuum of states $|\zeta\rangle$ with eigenvalues E.

$$H_0|\varphi_i\rangle = E_i|\varphi_i\rangle, \tag{5.1}$$

$$H_0|\zeta\rangle = E|\zeta\rangle, \tag{5.2}$$

The system is initially in the eigenstate $|\varphi_i\rangle$, at time t=0 a perturbation $W(t)$ is turned on.

$$H(t) = H_0 + W(t), \tag{5.3}$$

Since $|\varphi_i\rangle$ is not in general an eigenstate of the perturbed hamiltonian. The system is no longer in an eigenstate (if it were, it would stay indefinitely in that state) instead the state of the system is denoted by $|\psi(t)\rangle$ which is the initial state evolved in time under the influence of W.

The probability of the transition per unit time from $|\psi(t)\rangle$ to one of the final continuous states is given by (Cohen-Tannoudji, C. *et al* 1977)

$$\delta P\left(\varphi_i,\zeta_{\beta_f,E_f},t\right)=\int_{\substack{\beta\in\beta_f\\ E\in E_f}} dE\,\underbrace{d\beta\rho(E,\beta)}_{\substack{\text{\# of states}\\ \text{between}\\ \text{E}\to\text{E+dE}}}\underbrace{\left|\left\langle\zeta_{\beta,E}\middle|\psi(t)\right\rangle\right|^2}_{\substack{\text{transition probability}\\ \text{per state of }(\beta,\text{ E})}}, \tag{5.4}$$

where $\rho(E,\beta)$ is the density of final states, E and β are the labeling of the final states. Equation 5.4 states that the total probability of transition per unit time can be written as a product of the transition probability per state (probability density) times the number of final states between $\mathrm{E} \to \mathrm{E} + \mathrm{dE}$ summed over all possible final states.

Finding $|\psi(t)\rangle$ for an arbitrary perturbation strength is not simple, one needs to obtain the exact time evolution of the initial state under the effect of the perturbation $W(t)$. A significant simplification of the solution arises when the perturbation is taken to be small in comparison with the unperturbed hamiltonian such that,

$$\begin{aligned}&H_0 \sim \hat{W}(t)\\ &W(t)=\lambda\hat{W}(t)\ \ \lambda<<1\end{aligned}, \tag{5.5}$$

The emission probability per unit time depends on the number of available (number of allowed transitions) electromagnetic states in the atom, the number and type of available states in the medium and on the nature of the interaction between the atom and the medium in which it is placed. The total transition probability at time t (for short times $t << \frac{1}{\Gamma}$) is given for a constant perturbation by Fermi's golden rule[1],

---

[1] this leads to a transition probability $P_{i\to f}(t)=\Gamma t$ valid for very short times.

$$\Gamma = \frac{2\pi}{\hbar}\int d\beta \left|\langle \beta, E = E_i | W | \varphi_i \rangle\right|^2 \rho(\beta, E = E_i), \tag{5.6}$$

Perturbation of a two level atomic system in vacuum by an electromagnetic field

The electromagnetic modes of a radiation field in vacuum can be described as an infinite series of harmonic oscillators each having an energy,

$$\hbar\omega\left(n + \frac{1}{2}\right) \tag{5.7}$$

where n is the number of photons with $\hbar\omega$ energy. Each oscillator has a ground state of $\hbar\omega/2$, which is called the 'zero point' energy associated with quantum vacuum fluctuations. The rms vacuum electric amplitude for a mode of energy $\hbar\omega$ is

$$E_{vac} = \sqrt{\frac{\hbar\omega}{V2\varepsilon_0}}, \tag{5.8}$$

where, ε_0 is the permittivity of free space and V is the size of an arbitrary quantization volume.

The excited atom (2 level system e - g) interacts with the electric field modes of the vacuum through its electric dipole, the perturbation is of the form,

$$W = -\vec{E}_{vac} \cdot q\vec{d}, \tag{5.9}$$

where qd is the electric dipole moment.

The coupling is described by the matrix elements of the electric dipole of the atom between the two levels

$$\langle \varphi_g | W | \varphi_e \rangle = -\langle \varphi_g | \vec{E} \cdot q\vec{d} | \varphi_e \rangle, \tag{5.10}$$

The 'Rabi frequency' describes the frequency of energy exchange between the atom dipole and a hypothetical single mode field,

$$\Omega_{e\leftrightarrow g} = \frac{D_{eg}E_{vac}}{\hbar}, \tag{5.11}$$

where

$$D_{eg} = -\langle \varphi_g | qd | \varphi_e \rangle, \tag{5.12}$$

is the matrix elements of the electric dipole between the final and initial states.

The probability of a photon emission per unit time for an atom in its excited state is given by Fermi's Golden Rule,

$$\Gamma_0 = \frac{2\pi}{3}\Omega^2{}_{e\leftrightarrow g}\rho_0(\omega) = \frac{\omega^3 |D_{eg}|^2}{3\pi\hbar c^3 \varepsilon_0}, \tag{5.13}$$

where it is assumed that $V >> \lambda^3$.

The probability of finding an atom prepared in state e in the excited state after time t is

$$P_e(t) = e^{-\Gamma_0 t}, \tag{5.14}$$

This irreversible decay law is a result of the continuum of field modes resonantly coupled to the atom.

The mode structure of the vacuum field is altered in a cavity whose size is comparable to the wavelength. In the configuration below an atom is placed between two parallel mirrors. For an electric field polarized parallel to the mirrors (σ mode) no mode exists unless $\lambda < 2d$.

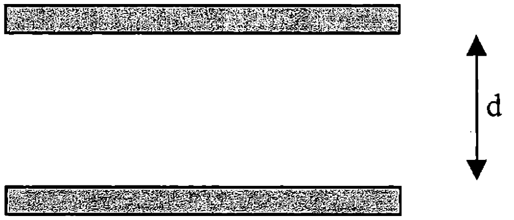

Figure 5.1 Parallel mirrors

Since the density of electromagnetic states for the parallel polarized light is zero the probability of transition Eq. 5.4 is zero. Consequently an excited atom which can emit only parallel polarized radiation in its decay process will have an infinite lifetime in this configuration, thus suppressing the spontaneous emission. If the distance between the mirrors is an integer number of wavlengths a peak in the density of states will form the cavity is at resonance with the emission wavelength leading to an enhanced emission.

The atom in the cavity sees a density of modes which is inversely proportional to the cavity bandwidth - $\Delta\omega_c$,

$$\sim 1/\Delta\omega_c \tag{5.15}$$

The quality factor is a dimensionless number which describes the cavity bandwidth and is defined as,

$$Q = \omega / \Delta\omega_c, \tag{5.16}$$

In a low Q cavity the emitted photon is damped rapidly much like it does in free space though at an enhanced rate

$$\Gamma_{cav} = \Gamma_0 \frac{Q\lambda^3}{V}, \tag{5.17}$$

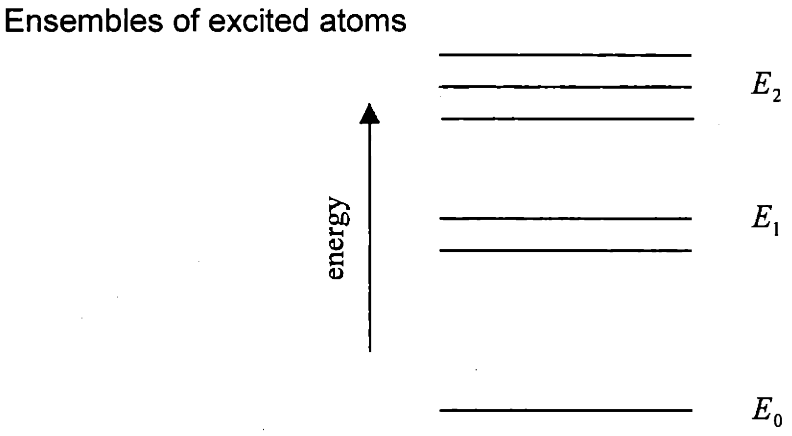

Figure 5.2 Energy levels for an atomic system

An ensemble of N_2 systems in energy level E_2 will decay to their lower energy state E_1 at a rate of $t_{spont}{}^{-1}$ per unit time,

$$-\frac{dN_2}{dt} = \Gamma_0 N_2 = \frac{1}{\tau_{spont}} N_2 , \tag{5.18}$$

t_{spont} is called the spontaneous lifetime associated with the $E_2 \to E_1$ transition.

Spectral characteristics of spontaneous emission

The emitted radiation associated with the $E_2 \to E_1$ transition is not strictly monochromatic, it is described by $g(\nu)$ which maps the frequency of the emitted radiation to the emitted intensity.

One distinguishes between two types of broadening homogeneous and inhomogeneous. In the homogeneous case the spectral broadening is associated with the finite lifetime of the excited state which can be due to the spontaneous lifetime of the excited state, or to changes in the phase between the field and atom due to collisions with phonons. Modeling the emission from the excited state as a damped harmonic oscillator with a damping coefficient of $1/\tau$ the radiated field is

$$E(t) = E_0 e^{-t/\tau} \cos \omega_0 t , \tag{5.19}$$

The spectral characteristics of the field are revealed upon taking the Fourier transform of E.

$$\begin{aligned} E(\omega) &= \int_0^\infty E(t) e^{-i\omega t} dt \\ &= \frac{E_0}{2}\left(\frac{i}{(\omega - \omega_0) + i/\tau} - \frac{i}{(\omega + \omega_0) + i/\tau} \right) \end{aligned} , \tag{5.20}$$

The spectral density distribution function in the vicinity of ω_0 is Lorentzian and is proportional to $|E(\omega)|^2$

$$|E(\omega)|^2 \propto \frac{1}{(\omega-\omega_0)^2+\tau^{-2}}, \tag{5.21}$$

The line width of a Lorentzian is given by,

$$\Delta\nu = \frac{1}{\pi\tau}, \tag{5.22}$$

The emitted intensity as a function of frequency is called the Lineshape function - $g(\nu)$ which is normalized,

$$\int_0^\infty g(\nu)d\nu = 1, \tag{5.23}$$

The shape of the line function for the homogeneous broadening as a function of the linewidth is given by,

$$g(\nu) = \frac{\Delta\nu}{2\pi\left((\nu-\nu_0)^2+(\Delta\nu/2)^2\right)}, \tag{5.24}$$

where the line width is made up of the sums of both finite lifetime of the states and the time between collisions. Both of these processes interrupt the temporal coherence length and minimize the coherent interaction of the atom (in both states) with the field.

$$\Delta\nu = \frac{1}{\pi}\left(\tau_2^{-1}+\tau_1^{-1}+\tau_{coll2}^{-1}+\tau_{coll1}^{-1}\right), \tag{5.25}$$

In contrast inhomogeneous broadening is due to induced changes in the electronic band structure of atoms due to their distinguishable environment or as a result of the velocity of the emitter (important in gases).

Induced transitions

When an excited system initially in state E_2 is placed in an electromagnetic field of energy

$$h\nu = (E_2 - E_1), \tag{5.26}$$

it will make a transition to state E_1 at a rate which is proportional to the intensity of the electromagnetic field which is given by (Yariv 1985),

$$W_{induced}(\nu) = \frac{c^2 I_\nu}{8\pi n^2 h \nu^3} \Gamma_{spont} g(\nu), \tag{5.27}$$

where I_ν is the intensity of the electromagnetic field at the transition frequency, n is the index of refraction of the medium, h is Planck's constant, Γ_{spont} is the spontaneous emission rate.

When an monochromatic wave of intensity I_ν and frequency ν propagates through a medium with N_2 atoms per unit volume in level 2 and N_1 atoms per unit volume in level 1 there will occur $N_2 W_{induced}(\nu)$ $2 \to 1$ transitions and $N_1 W_{induced}(\nu)$ $1 \to 2$ transitions. These will add coherently to the travelling wave leading to a increase in the intensity per unit length,

$$\frac{dI_\nu}{dz} = (N_2 - N_1) W_{induced}(\nu) h\nu = (N_2 - N_1) \frac{c^2}{8\pi n^2 \nu^2} \Gamma_{spont} g(\nu) I_\nu, \tag{5.28}$$

with the corresponding solution,

$$I_\nu(z) = I_\nu(0) e^{\gamma(\nu) z}, \tag{5.29}$$

where the gain coefficient is,

$$\gamma(\nu) = (N_2 - N_1) \frac{1}{8\pi} \left(\frac{c}{n\nu}\right)^2 g(\nu) \Gamma_{spont}, \tag{5.30}$$

which results in exponentially growing solutions in the case of a population inversion e.g $N_2 > N_1$.

Laser oscillation

The quality factor is defined as

$$Q = \omega \frac{\text{energy stored in cavity}}{\text{power dissipated in cavity}} = \frac{\omega \varepsilon}{-d\varepsilon / dt}, \tag{5.31}$$

where,

$$-\frac{d\varepsilon}{dt} = \frac{\varepsilon}{t_c}, \tag{5.32}$$

and,

$$t_c = \frac{2nl}{c\left[\frac{4\pi k}{\lambda} l - \ln\sqrt{R_1 R_2}\right]}, \tag{5.33}$$

l – is the cavity length, k is the imaginary part of the refractive index, R_1, R_2 are the mirror reflectivities.

$$Q = \omega t_c, \tag{5.34}$$

The lasing threshold condition for a gain medium - γ located between two parallel mirrors of reflectivities R_1 and R_2,

$$\gamma_t(\omega) \geq \frac{4\pi k}{\lambda} - \frac{1}{l} \ln R_1 R_2,, \tag{5.35}$$

The quality factor of the cavity can also be calculated from,

$$Q = \omega t_c = \frac{nl}{\lambda} \frac{2\pi}{\left[\frac{4\pi k}{\lambda} l - \ln\sqrt{R_1 R_2} \right]} , \tag{5.36}$$

Experimental determination of lasing threshold

(a) **Intensity Transition** - In cases where the gain medium is homogeneously broadened the laser emission above threshold should consist of a single mode, the output power for the lasing mode scales linearly as a function of the excitation energy while the emission from the other modes is constant (pinned).

$$\left. \frac{dI^{(output)}}{dI^{(input)}} \right|_{<threshold} < \left. \frac{dI^{(output)}}{dI^{(input)}} \right|_{>threshold} , \tag{5.37}$$

where $I^{(input)}$ is the input energy density (typically in $\mu J / cm^2$) and $I^{(output)}$ is the output energy.

If the inhomogeneous broadening is significant one may observe multimode operation.

(b) **Polarization** - When the laser cavity has a polarization dependent component the modes above threshold should have a well-defined polarization, or show an enhanced polarization dependence.

(c) **Spectral Narrowing** – If below threshold the spontaneous emission is distributed among a number of modes at lasing the emission will show a spectral narrowing.

Principle of operation of the self assembled microcavity structure

The system consists of a planar layer of well defined thickness which has in it an active material capable of optical transitions across a over a broad range of frequencies. The planar layer is designed to be of an optical length corresponding to half-wavelength. The optical confinement of the electromagnetic energy to the layer is provided by a self assembled dielectric stack (combined with a metalic layer in one case). As shown in Eq. (5.17) an enhancement of the emission rate over the spontaneous rate is possible in a resonant cavity structure which is proportional to the quality factor of the cavity. The cavity is optically pumped by a Ar ion laser at 457nm which is unaffected by the cavity structure, an high pump intensity may lead to a positive gain factor Eq. (5.30), and ultimately to the satisfaction of the lasing condition Eq. (5.35).

5.3 Microcavity design

The interaction between the cavity modes and the active media were explored for two different types active media in different mocrocavity designs. The first shown in Fig. 5.3(A) is a conjugated polymer placed at precise locations whithin the microcavity which is defined by a metallic mirror on one side and a self assembled polymeric reflector on the other. The second involves a laser dye (Coumarin 540) dispersed in an acrylic matrix confined between a silicon wafer and a self assembled PS-PI multilayer polymeric reflector on the other, in another case an acrylic matrix layer loaded with a coumarin dye was confined by two self assembled dielectric mirrors as shown in Fig. 5.3(B). Both of the microcavity structures illustrate important aspects of using self-assembled confining structures in conjunction with active materials. Such as; the high degree of control over the defect dimensions, the nature of the surface interactions between the defect layer and the self assembled mirror which determine the boundary conditions for the self assembly process, the need to couple charge into and out of the device in cases where electroluminescence is utilized.

The localization of the electromagnetic field in a defect is essentially a resonance phenomenon thus a high degree of control over the dimensions of the defect is required (as illustrated in later in Fig. 5.5). In contrast the self assembly process presents challenges to the control of any specific dimension though it offers a high degree of control on average. To accommodate this disparity a decoupling of the defect production process and the self-assembly process was introduced. The defect was produced as a separate entity in a process which affords precise thickness and composition control, subsequently the defect was incorporated into the confining structure. The ability to confine the electromagnetic energy in the defect region is very sensitive to boundary conditions at the edge of the defect, one needs to know what layer is in contact with the defect. By utilizing the difference in chemical character of the blocks one can design a surface which is energetically preferential to one of the BCP components, creating a high probability for its adsorption to the said surface. In both of the structures presented below the surface properties of the defect were adjusted to prefer the high dielectric component of the self assembled mirror.

For some applications it is necessary to position the defect in a precise location in the device (to attach electrodes for example) or to maximize the confinement efficiency. The metalo-dielectric structure is brought as an example where the defect layer location is known precisely, in fact by utilizing a layer by layer deposition technique of poly-electrolyte materials a control over the defect composition and nano-structure was acheived.

In other cases one can substantially simplify the production process by creating statistical defects exemplified by the all-dielectric structure where the position of the defect layer relative to the mirrors is not known precisely – in fact one can take this approach even further by dispersing defect platelets or spheres (or other geometries) loaded with active media in the BCP solution or melt.

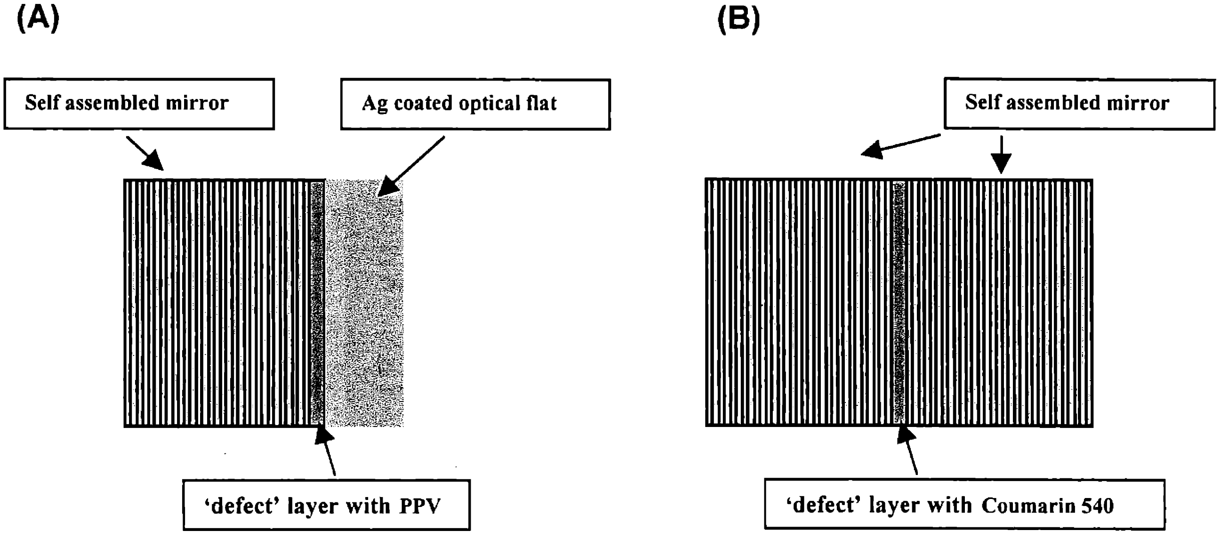

Figure 5.3 Two configurations of an optically confined defect layer: (A) PPV/PAA layer confined by a metal mirror (Ag or Al) on one side and a self assembled SI mirror on the other (B) A coumarin 540 dye dispersed in a photo-polymerized acrylic matrix confined on both sides by a self assembled SI mirror.

Fig. 5.3(A) is a schematic of the microcavity device where the optical confinement is provided by a metallic layer on one side of the cavity and a self assembled dielectric multilayer on the other. The active material in this structure is PPV((poly(p-phenylene vinylene) a conjugated polymer which has a broad photoluminescence spectra and an intensity peak located ~540nm (N. Tessler *et al* Nature 1996). The substructure of the defect layer is presented in Fig. 5.4. Fig. 5.3 (B) has a defect layer made of an acrylic UV cross-linked monomer with a coumarin dye dispersed in it.

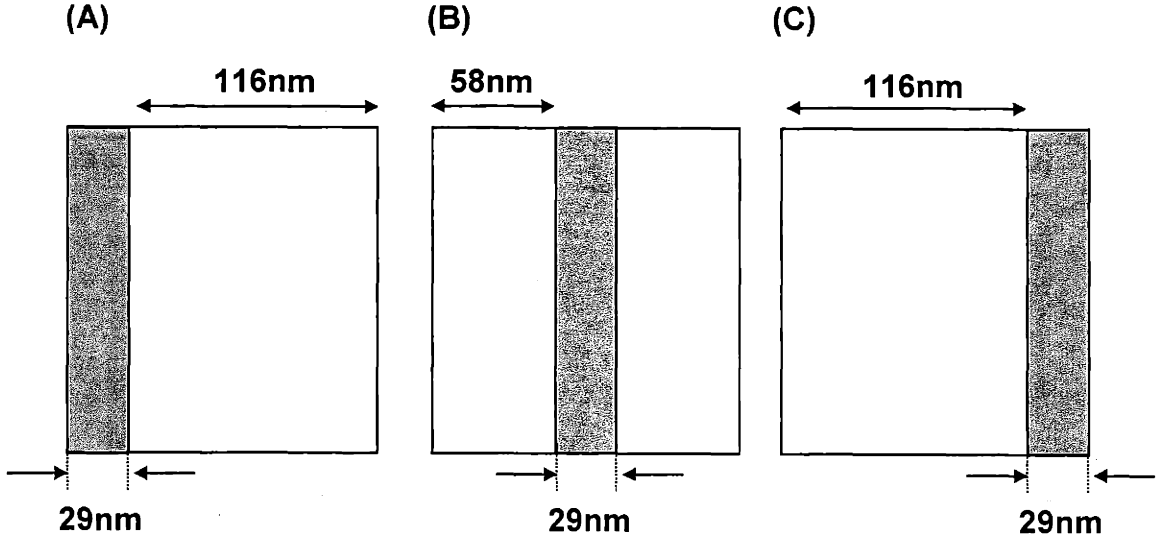

Figure 5.4 The defect layer sub-structure showing the active PPV/PAA 29nm thick layer in gray and a non-active layer (PAA/PAH) in white. The three diagrams depict different possibilities of positioning the active layer whithin the defect structure. Assuming that the silver layer is on the left and the self assembled stack is on the right; (A) active layer adjacent to the silver, (B) active layer in the center of the defect, (C) active layer adjacent to the dielectric stack.

The PPV/PAA layer is placed in the middle of a low index of refraction (1.55) layer because the PPV has a relatively (compared with the dielectric stack) high index of refraction (~1.9-2.3)[1] which would lead to a poor confinement if the entire defect layer was made of it. In addition by placing the emitting layer in different positions within the defect structure a mapping of the electric field is possible (S. E. Burns *et al* 1997). In order to determine the optimal defect layer thickness the electric field power density was calculated in the active region (divided by length) and compared to the power density in the first period of the dielectric stack as a function of the total defect layer thickness. The results of these calculations are presented in Fig. 5.5.

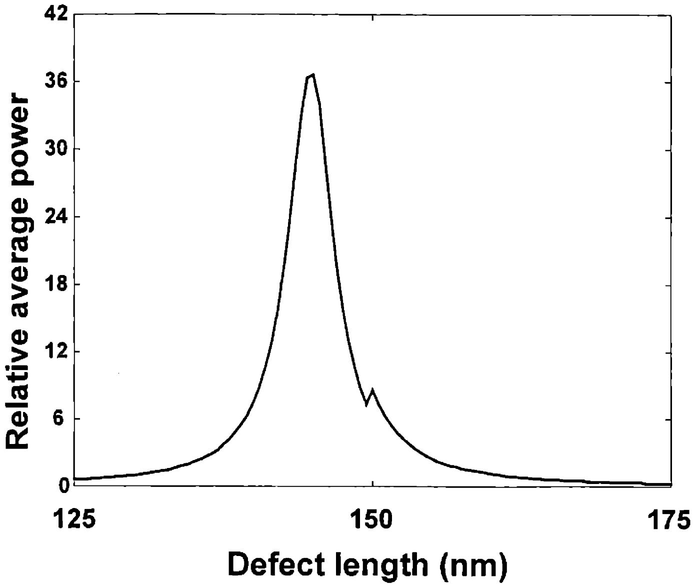

Figure 5.5 Power density in the active sublayer (29nm) divided by power density in the first period of dielectric stack (174nm) as a function of overall defect length.

The power density in the active sublayer which is positioned in the center of the defect layer and is 20% of its length, is sharply peaked (FWHM=4.9nm) around a thickness of 145nm. This requires great precision in the deposition process. The calculation was done for the confinement of a 540nm wave using a 30 period stack with a period of 174nm. In order to increase the probability of having the high index component (polystyrene) adjacent to the defect layer the surface of the defect layer was chosen to have a highly

---

[1] This value was obtained from ellipsometric measurements of the combined PPV/PAA layer which led to an index of 1.7-1.85 for ~50% volume PPV.

polar character which is expected to form a favorable interaction with the relativerly polar aromatic rings of the polystyrene.

In addition the dielectric mirror was cast from a solution and allowed to evaporate in a diffusion limited process such that a radially varying reflectivity band was established. This ensures the structure will confine the resonant wavelength.

5.4 Fabrication

The fabrication sequence of the self assembled microcavity structure is illustrated in Fig. 5.6. For sample A, a microscope cover slip (VWR #1 22x50mm) was coated with a 250nm thick film of silver (Ag) using vacuum evaporation fitted with a crystal thickness monitor.

Defect layer construction:

A microscope slide was baked in a vacuum oven for 4h at 150°C. The slide was then coated with 200nm silver using vacuum evaporation, the thickness of the deposited film was monitored by a crystal thickness monitor. Self-assembled multilayered films were fabricated on the silver-coated slide via the alternate adsorption of a polycation, and a polyanion. The polycations are a PPV(poly(p-phenylene vinylene) precursor and PAH(polyallylamine), while the polyanion is PAA(polyacrylic acid)). The PAA (Mw 90,000) and PPV(Mw~10^6) were provided by Polyscience and Lark Enterprises respectively while the PAH (Mw 70,000) was obtained from Polyscience. PAA was used at a 10^{-2}M concentration while the PPV precursor was used at 10^{-4}M. Both polyion solutions were pH adjusted with dilute NaOH to pH 4.5 and filtered with 0.45μm and 30μm filters respectively. A bilayer of PAA/PAH(polyallylamine) at pH 4.5/ 4.5 was deposited onto the silver-coated substrate it was used at 10^{-2}M concentration and filtered using 0.45μm size filter. In the electroststic adsorption process, the substrate was alternately dipped into the polycation(PPV precursor or PAH) and polyanion(PAA) solutions for 15 minutes with 3 rinsing steps totalling 6 minutes in between. The rinsing water as well as all water used in this process was de-ionized and and filtered.

The active regime whithin the defect strcuture is made of a 29nm thick film of alternating PPV/PAA layers which is placed in three different positions as shown in figure 5.4 (A-C), the rest of the defect strucutre is made of alternating layers of PAH/PAA the total thickness of 116nm.

The PPV precursor was converted under vacuum for 11h at 290°C.

A calibration curve monitoring the growth rate of the PAA/PPV multilayers was generated and is shown in Appendix E. The growth is generally linear after the first 10 bilayers have been deposited. Film thicknesses shown were measured using Profilometry followed by the Ellipsometry to measure the indices of refraction. Films of PAA/PPV multilayers of thicknesses varying from 11nm-16nm were prepared with the required number of bilayers determined from the growth curve.

Self assembled mirror:

A 0.1g/ml solution of styrene-isoprene (1947k:197k) block copolymer in toluene was prepared and mixed with two solutions of homopolymer styrene (13k) and homopolymer isoprene (13k) both in styrene (0.1g/ml) at a 3.8/1.75/1.75 ratio. The combined solution was stirred for 5h. 0.15ml of this solution was deposited on the defect layer. The solution was allowed to evaporate for 25 minutes and then covered with a 22mm glass microscope cover slide (VWR #1). The solution was allowed to evaporate over a period of 12h during which the reflectivity of the structure was monitored as a function of radial distance.

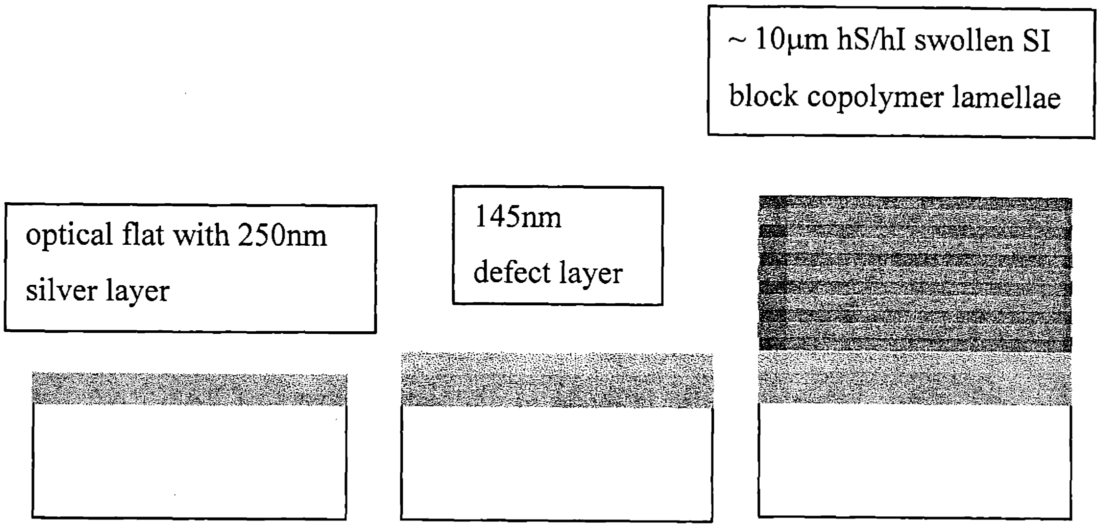

Figure 5.6 Resonant cavity fabrication sequence.

For sample B, a ~350nm[1] thick film made of an acrylate-methacrylate monomer (Norland #61) was spun coat at 4000RPM from a solution of the monomer in toluene (0.206g/1ml) containing Coumarin 540 dye (0,027g/17.64g of toluene). The layer was cured under a UV lamp for 6 minutes. A 10% by weight solution of SI (194k:197k) in toluene was prepared and then mixed with homopolymer styrene (13k) and homopolymer isoprene (13k) both in toluene at equal weight concentrations at a ratio of 3/1/1. The solution was then mixed for 5h, after which 0.13ml was deposited onto the Si substrate with the defect layer and was immediately covered with a glass cover slide (VWR #2 25mm diameter). The solvent was allowed to evaporate for 72h before beginning the optical measurements.

---

[1] the thickness of the cured film was determined by ellipsometer to be 354nn and by profilometer to be 344nm

5.5 Optical measurements

The resonant cavity measurement setup is illustrated in Fig. 5.7.

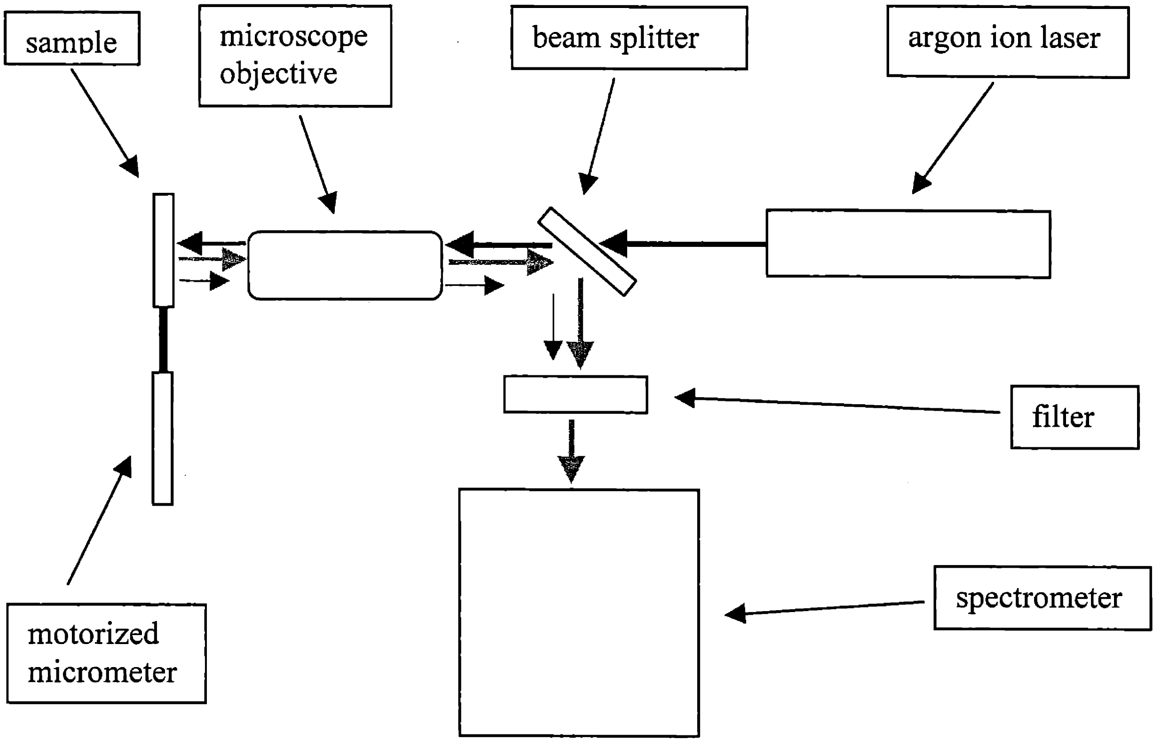

Figure 5.7 Resonant cavity emission optical measurement setup

An argon ion beam line of 457nm is emitted from the source, it then travels through a beam splitter and into a microscope objective which focuses it onto the sample which is mounted on a motorized micrometer translation stage. The microscope objective has a NA=0.7 and a focal length of 3mm. This implies a collection angle of 44.4°. A second objective that we used has a NA=0.1 and a collection angle of 5.7°. The depth of focus for the objectives are

$$D_f = \pm \frac{n\lambda}{2(NA)^2} = \begin{cases} 466nm_{NA=0.7} \\ 22850nm_{NA=0.1} \end{cases} \tag{5.38}$$

where n is the index of refraction of air, λ is 457nm the excitation line and NA is the numerical aperture. The emitted light is collected by the microscope objective and directed into a spectrometer after passing through a filter which prevents the excitation source from saturating the detector.

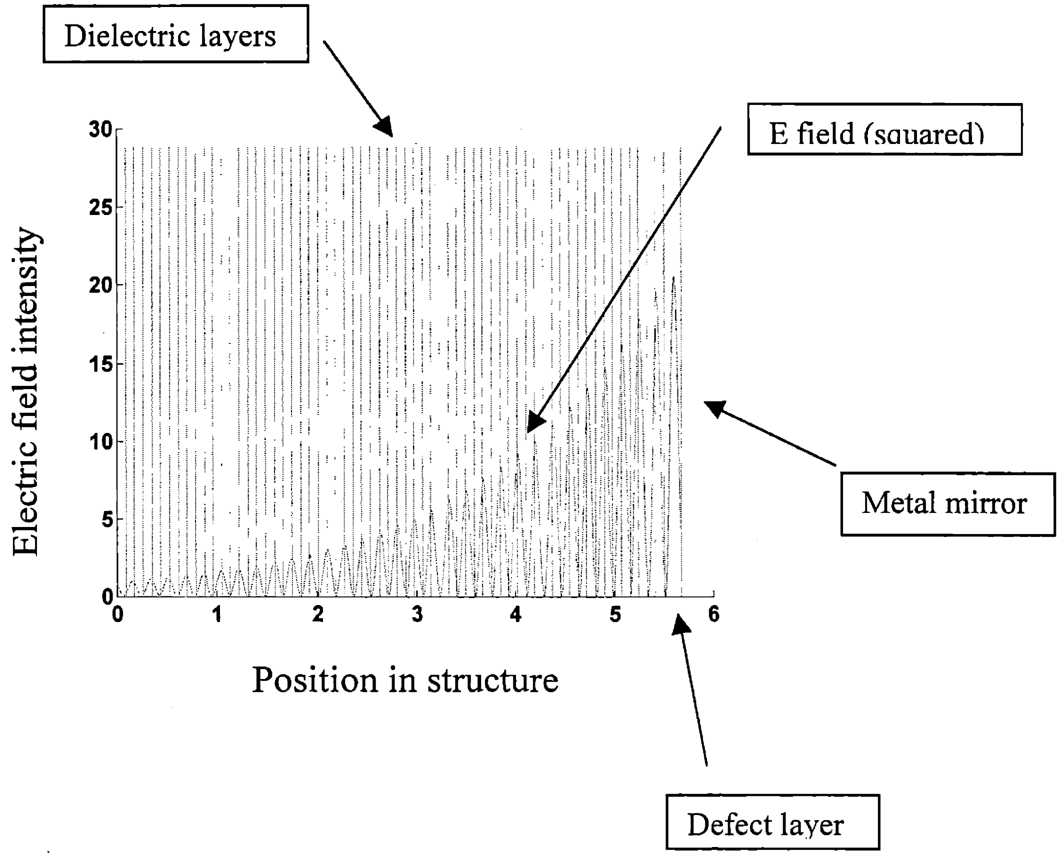

Figure 5.8 Simulation of the spacial distribution of the power density in a multilayer structure with a resonant defect confined by 30 periods of SI on the left and by an Ag mirror on the right.

A simulation of the electric field power density is shown in Fig. 5.8 which shows the buildup of the power density in the sample. The decay is exponential with a decay length of approximately 19 periods, the maximum power amplitude in the cavity is at its center and is approximately 20 time the maximum achieved in the first period.

5.6 Spectroscopic measurements and discussion

Cavity LED response

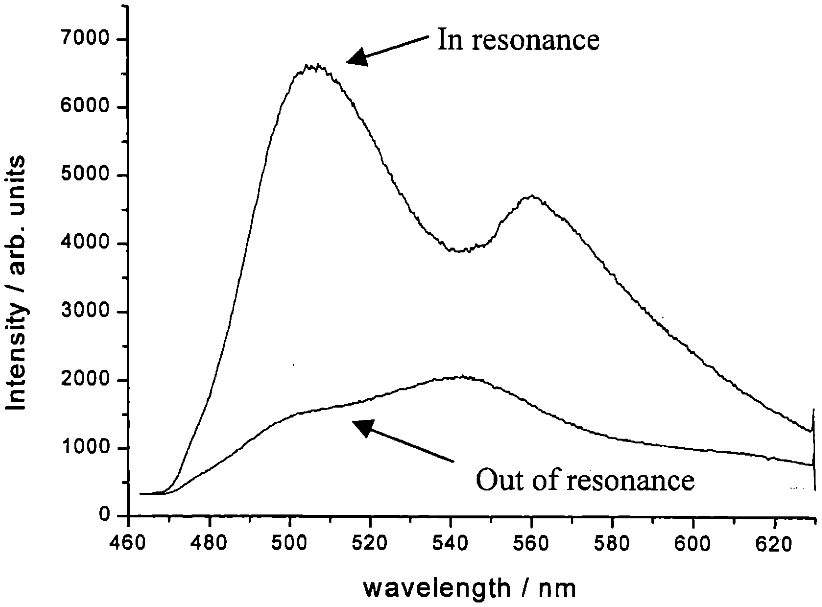

Figure 5.9 Normal emission from coumarin 540 dye in an acrylic matrix in a resonant cavity and in a non-resonant cavity.

The optical setup described in section 5.5 was used (with the 0.7NA objective) to excite the microcavity structure described above (sample B). The measure emission intensity was measured at different radial positions corresponding to different peak reflectivity values. The emission across the sample was relatively constant and had a lineshape which is exemplified by the lower curve in figure 5.9 with a peak emission around 540nm which is characteristic of the coumarin 540 dye. Towards the edge of the sample (at a radial distance of about 3mm from the edge) a transition of the emission spectra occurred shown in the upper trace in Fig 5.9. A peak narrowing and a shift of the maximum emission to around 500nm was observed as well as a substantial increase in the intensity. To eliminate the possibility of a filtering effect a reflectivity measurement at different radial positions of the structure was performed showing an edge reflectivity of 500nm which is precisely the position of the observed enhanced emission peak. The reflectivity measurements are presented in Fig. 5.10 at different radial positions.

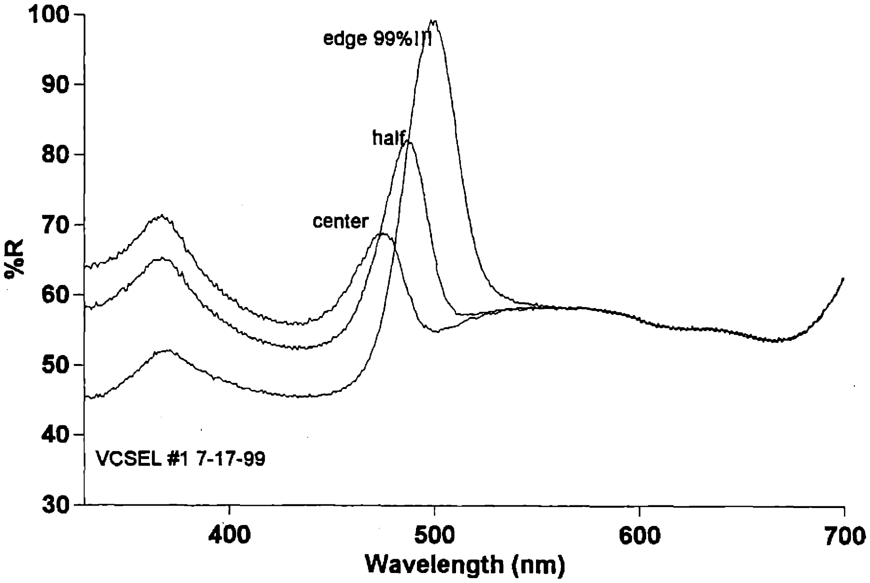

Figure 5.10 Reflectivity vs. wavelength for the Coumarin 540 defect layer sample.

The quality factor for this structure is calculated from Eq. (5.36) to be ~7.5 (because of the low reflectivity of the Si substrate) which is close to the observed peak to peak width ratio. These results are a first attempt in incorporating defects of well defined thickness into a self assembled 1D photonic crystal. It is shown that a shift of the dye maximum emission is achieved along with a line narrowing of the dye emission spectrum which cannot be attributed to a filtering effect. The corresponding maximum emission is enhanced by a factor of ~5 which is comparable to the calculated cavity quality factor.

In summary, this chapter presented two methods for the incorporation of defect of precise dimensions and well defined composition into 1D self assembled photonic crystals. Currently work is in progress on using the PPV/PAA layer approach to sample the electric field structure within the defect layer.

Summary

In this thesis work I tried to provide simple and practical methods for manipulating and confining light through the use of periodic dielectric structures aslo known as photonic crystals. I would like these methods to serve as basic tools which one can then apply to a variety of applications and real world problems some of which we have just barely begun to uncover. The advance of human knowledge has in many cases been associated with the ability to utilize new materials and create new tools. I hope that the simplicity of the approaches outlined in the thesis will make photonic crystals readily accessible to a broad spectrum of uses.

Two separate but related basic contributions were outlined in this thesis. The first is the definition of the simplest structure that can provide complete confinement of light – the omnidirectional reflector. The second is a general methodology for self-assembling photonic crystals of any dimensionality from block copolymers.

A design criterion that permits truly omnidirectional reflectivity for all polarizations of incident light over a wide selectable range of frequencies is derived and used in fabricating an all-dielectric omnidirectional reflector consisting of multilayer films. Because the omnidirectionality criterion is general, it can be used to design omnidirectional reflectors in many frequency ranges of interest. Potential uses depend on the geometry of the system. For example, coating of an enclosure will result in an optical cavity. A hollow tube will produce a low-loss, broadband waveguide, planar film could be used as an efficient radiative heat barrier or collector in thermoelectric devices.

A comprehensive framework for creating one, two and three dimensional photonic crystals out of self-assembling block copolymers has been formulated.

. In order to form useful band gaps in the visible regime, periodic dielectric structures made of typical block copolymers need to be modified to obtain appropriate characteristic distances and dielectric constants. Moreover, the absorption and defect concentration must also be controlled. This affords the opportunity to tap into the large structural repertoire, the flexibility and intrinsic tunability that these self-assembled block copolymer systems offer.

A block copolymer was used to achieve a self assembled photonic band gap in the visible regime. By swelling the diblock copolymer with lower molecular weight constituents control over the location of the stop band across the visible regime is achieved. One and three-dimensional crystals have been formed by changing the volume fraction of the swelling media. Methods for incorporating defects of prescribed dimensions into the self-assembled structures have been explored leading to the construction of a self assembled microcavity light-emitting device.

Appendix

A. Deposition technique for polystyrene tellurium multilayer structure

A $0.8 \pm 0.09\mu m$ thick layer of tellurium (99.99+%, Strem Chemicals) was vacuum evaporated at 10^{-6} torr and 7A (Ladd Industries 30000) onto a NaCl 25mm salt substrate (polished NaCl window, Wilmad Glass). The layer thickness and deposition rate were monitored in-situ using a crystal thickness monitor (Sycon STM100). A 10% solution of polystyrene (GoodYear PS standard, 110,000g/mol) in toluene was spin cast at 1000RPM onto the tellurium coated substrate and allowed to dry for a few hours, the polymer layer thickness is $1.65 \pm 0.09\mu m$.

B. Photonic band structure for the "knitting pattern"

A rectangular unit cell defines the "knitting pattern" structure. Repeating the unit cell at regular intervals, which are multiples of the primitive lattice vectors, reproduces the entire structure. The plane group includes symmetry elements, which are translational, and point operations under which the unit cell stays invariant.

The unit cell

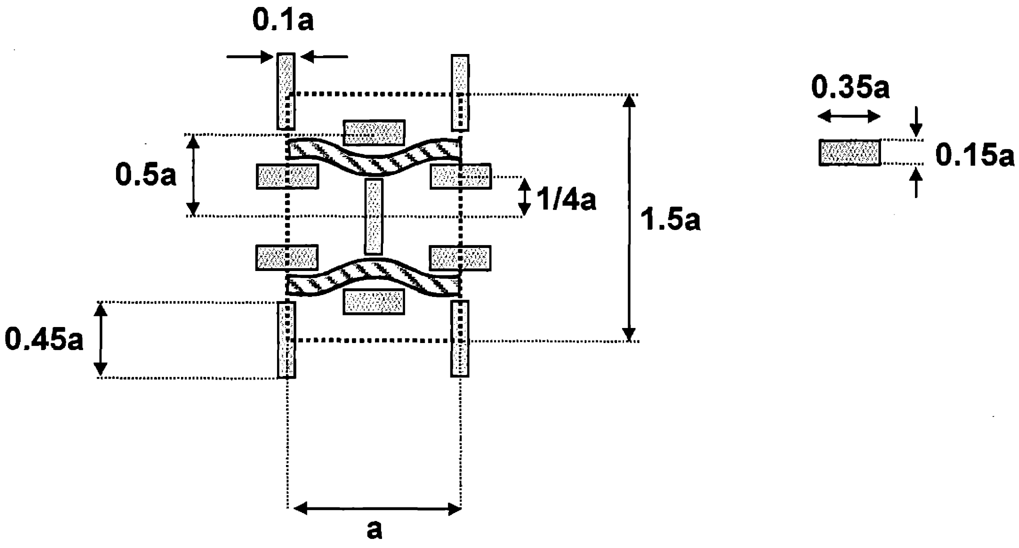

Figure B.1 The unit cell of the knitting pattern structure.

The primitive lattice vectors for this structure are,

$$\begin{aligned} \vec{a}_1 &= a(1,0) \\ \vec{a}_2 &= a\left(0,\frac{3}{2}\right), \end{aligned} \tag{B.1}$$

The point group symmetry elements

The point group of the crystal is C_{2v} has the following symmetry elements $\{E,\ \mathrm{C}_2,\ \sigma,\ \sigma'\}$ E is the identity operator, C_2 is a π rotation about the z axis, σ is a mirror operation about the x-z plane, σ' is a mirror operation about the y-z plane.

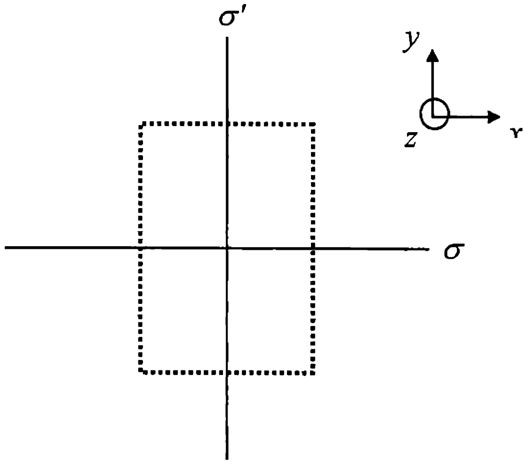

Figure B.2 The symmetry elements of the C_{2v} plane group.

The Brillouin zone

The reciprocal lattice vectors are,

$$\begin{aligned}\vec{b}_1 &= 2\pi\frac{\vec{a}_2\times\vec{a}_3}{\vec{a}_1\cdot(\vec{a}_2\times\vec{a}_3)} = \frac{2\pi}{a}(1,0,0)\\ \vec{b}_2 &= 2\pi\frac{\vec{a}_3\times\vec{a}_1}{\vec{a}_1\cdot(\vec{a}_2\times\vec{a}_3)} = \frac{4\pi}{3a}(0,1,0)\end{aligned}, \qquad \text{(B.2)}$$

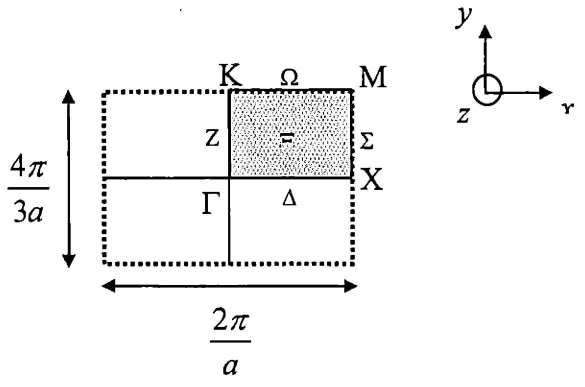

Figure B.3 The first Brillouin zone and the *irreducible* Brillouin zone (shaded in grey).

There are 8 types of k points:

$$\Gamma{:}(0,0),\quad \mathrm{X}{:}\left(\frac{1}{2},0\right),\quad \mathrm{M}{:}\left(\frac{1}{2},\frac{1}{3}\right),\quad K{:}\left(0,\frac{1}{3}\right)$$

$$\Delta{:}(\delta,0),\quad \Sigma{:}\left(\frac{1}{2},\gamma\right),\quad \Omega{:}\left(\delta,\frac{1}{3}\right),\quad \mathrm{Z}{:}(0,\gamma),\quad \Xi{:}(x,y)$$

$$0\le\delta,\ \mathrm{x}\le\frac{1}{2},\ 0\le\gamma,\ \mathrm{y}\le\frac{1}{3}.$$

Since the plane group is symmorphic (no fractional translations), any representation of the plane group can be written as a product of a corresponding representation of the point group and the representation of the translational group which is Abelian[1] and therefore is of dimension one. The point group and plane group are homomorphic.

$$D^{(\vec{k},\,\alpha)}\left(\left\{U_{\vec{k}}\middle|\vec{R}\right\}\right)=\underbrace{e^{-i\vec{k}\cdot\vec{R}}}_{\substack{\text{representation of the}\\ \text{Abelian discrete}\\ \text{translation group}}}\ \underbrace{D^{(\alpha)}\left(\left\{U_{\vec{k}}\right\}\right)}_{\substack{\text{representation of the}\\ \text{point group}}}\,, \qquad \text{(B.3)}$$

It is sufficient therefore to consider the point group representations. With each distinct k point one can associate a subgroup of the point group which leaves it invariant.

$\Gamma,\mathrm{X},\mathrm{M},K$: $\{\mathrm{E},\ \mathrm{C}_2,\ \sigma,\ \sigma'\}$

Δ: $\{\mathrm{E},\ \sigma\}$, Σ: $\{\mathrm{E},\ \sigma'\}$, Ω: $\{\mathrm{E},\ \sigma\}$, Z: $\{\mathrm{E},\ \sigma'\}$

These are the point groups of k.

---

[1] The elements of an Abelian group are $\{\mathrm{E},\ \mathrm{a},\ \mathrm{a}^2,\ \mathrm{a}^3\ldots\}$.

The character tables for the point groups of k

Δ, Ω	E	σ
$\Delta^{(1)},\Omega^{(1)}$	1	1
$\Delta^{(2)},\Omega^{(2)}$	1	-1

Z, Σ	E	σ
$Z^{(1)},\Sigma^{(1)}$	1	1
$Z^{(2)},\Sigma^{(2)}$	1	-1

Γ,X,M,K	E	C_2	σ	σ'
$\Gamma^{(1)},X^{(1)},M^{(1)},K^{(1)}$	1	1	1	1
$\Gamma^{(2)},X^{(2)},M^{(2)},K^{(2)}$	1	1	-1	-1
$\Gamma^{(3)},X^{(3)},M^{(3)},K^{(3)}$	1	-1	1	-1
$\Gamma^{(4)},X^{(4)},M^{(4)},K^{(4)}$	1	-1	-1	1

Table B.1 Character tables for the various special k points.

Consequences

- All of the irreducible representations are one-dimensional there are no essential degeneracies.
- These tables tell us how the eigenfunctions transform under the symmetry operations at very k point.
- These are the only allowed symmetries for the energy bands.

Compatibility

$$D^{(\alpha)}(A_s)=\sum_{\beta} n_\beta D^{(\beta)}(A_s), \tag{B.4}$$

where the (β) are the irreducible representations of $\{A_s\}$.

$$n_\beta=\frac{1}{h_\beta}\sum_{A_s}\chi^{(\beta)}(A_s)^*\chi^{(\alpha)}(A_s), \tag{B.5}$$

(α) and (β) are said to be compatible if $n_\beta \neq 0$.

Since we have only two distinct irreducible representation character tables the compatibility relations are

$$\begin{aligned} n_{\Delta^{(1)}} &= \frac{1}{2}\left(1\cdot\chi^{(\Gamma)}(E)+1\cdot\chi^{(\Gamma)}(\sigma)\right) \\ n_{\Delta^{(2)}} &= \frac{1}{2}\left(1\cdot\chi^{(\Gamma)}(E)-1\cdot\chi^{(\Gamma)}(\sigma)\right) \end{aligned}, \tag{B.6}$$

The following transitions are compatible,

$$\begin{aligned} &\Gamma^{(1)} \rightarrow \Delta^{(1)},\ \mathrm{Z}^{(1)} \\ &\Gamma^{(2)} \rightarrow \Delta^{(2)},\ \mathrm{Z}^{(2)} \\ &\Gamma^{(3)} \rightarrow \Delta^{(1)},\ \mathrm{Z}^{(2)} \\ &\Gamma^{(4)} \rightarrow \Delta^{(2)},\ \mathrm{Z}^{(1)} \end{aligned}, \tag{B.7}$$

where Γ, Δ, and Z were chosen as representative examples.

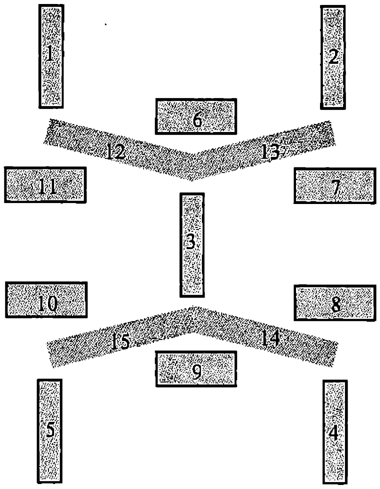

Figure B.4 The unit cell used in the "knitting pattern" band gap calculation.

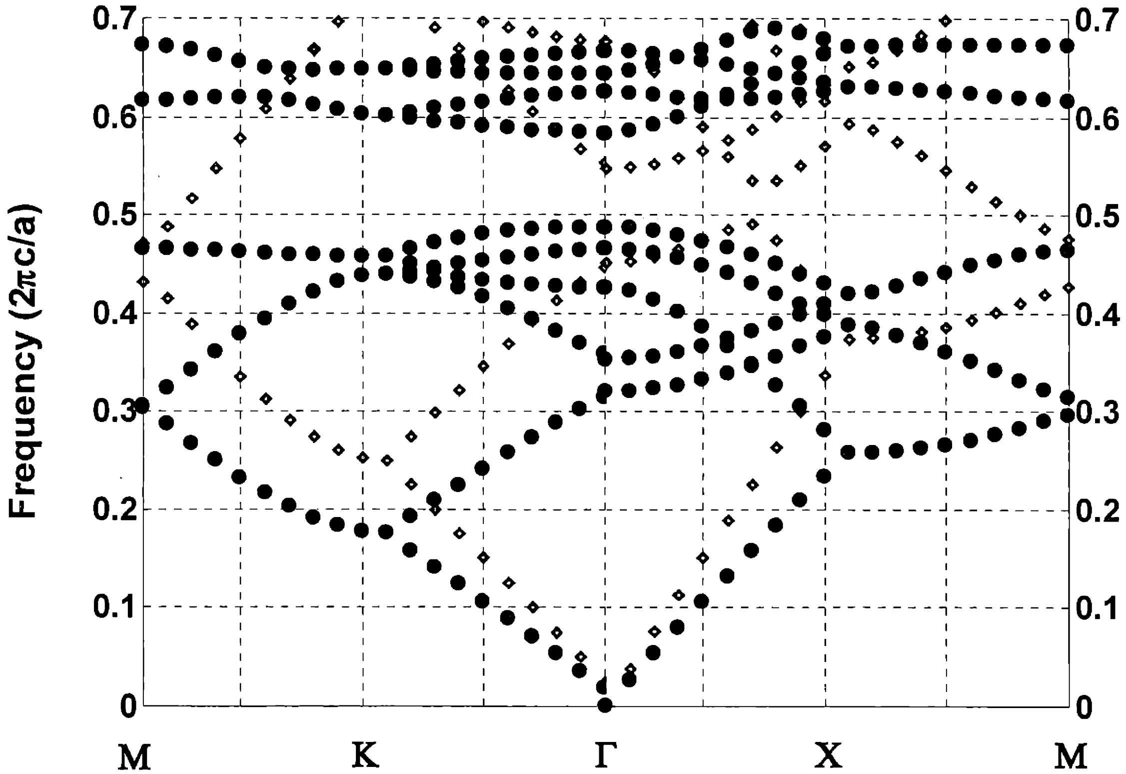

Figure B.5 The photonic band structure for the "knitting pattern" the directions correspond to the reduced Brillouin zone in Fig B.3.

C. Analytic expression for the decay length in a multilayer structure

$$\vec{E}_n^a(x,z,t) = \left(a_n e^{ik_{1x}(x-n\Lambda+b)} + b_n e^{ik_{1x}(x-n\Lambda+b)}\right) e^{i(\omega t-\beta z)}$$

$$\vec{E}_n^b(x,z,t) = \left(c_n e^{ik_{1x}(x-n\Lambda)} + d_n e^{ik_{1x}(x-n\Lambda)}\right) e^{i(\omega t-\beta z)}$$

$$E_K(x+\Lambda) = E_K(x) \rightarrow \vec{E}(x+\Lambda,z,t) = \vec{E}(x,z,t)e^{-iK\Lambda}$$

$$\begin{pmatrix} a_n \\ b_n \end{pmatrix} = \begin{pmatrix} a_{n-1} \\ b_{n-1} \end{pmatrix} e^{-iK\Lambda}$$

$$\begin{pmatrix} A & B \\ C & D \end{pmatrix}\begin{pmatrix} a_n \\ b_n \end{pmatrix} = e^{iK\Lambda}\begin{pmatrix} a_n \\ b_n \end{pmatrix}$$

$$\text{TE: } \mathrm{A}_{\mathrm{TE}} = \mathrm{e}^{-\mathrm{i}k_{1x}a}\left(\cos k_{2x}b - \frac{1}{2}\mathrm{i}\left(\frac{k_{2x}}{k_{1x}} + \frac{k_{1x}}{k_{2x}}\right)\sin k_{2x}b\right),$$

$$\mathrm{D}_{\mathrm{TE}} = \mathrm{e}^{\mathrm{i}k_{1x}a}\left(\cos k_{2x}b + \frac{1}{2}\mathrm{i}\left(\frac{k_{2x}}{k_{1x}} + \frac{k_{1x}}{k_{2x}}\right)\sin k_{2x}b\right)$$

$$\text{TM: } \mathrm{A}_{\mathrm{TM}} = \mathrm{e}^{-\mathrm{i}k_{1x}a}\left(\cos k_{2x}b - \frac{1}{2}\mathrm{i}\left(\frac{n_1^2k_{2x}}{n_2^2k_{1x}} + \frac{n_2^2k_{1x}}{n_1^2k_{2x}}\right)\sin k_{2x}b\right),$$

$$\mathrm{D}_{\mathrm{TM}} = \mathrm{e}^{\mathrm{i}k_{1x}a}\left(\cos k_{2x}b + \frac{1}{2}\mathrm{i}\left(\frac{n_1^2k_{2x}}{n_2^2k_{1x}} + \frac{n_2^2k_{1x}}{n_1^2k_{2x}}\right)\sin k_{2x}b\right)$$

$$k_{\alpha x} = \frac{\omega}{c}\sqrt{n_\alpha^2 - \mathrm{snell}(\theta)^2}$$

$$Tr(M) \in \mathrm{Re}$$

$$K_i = \mathrm{Re}\left(\frac{1}{\Lambda}\cosh^{-1}\frac{A+D}{2}\right)$$

D. Increasing the solubility of CdSe nanocrystals in polymers with functionalized oligomers

Trioctyl phosphine Oxide capped nanocrystals tend to phase separate and form large (~1 μm) aggregates in solutions containing polymers. The aggregation is due probably to the highly polar nature of the nanocrystal surface and the positive enthalpic interaction with the hydrophobic polymers. The TOPO molecules apparently do not provide an effective screening of the polar surface while in solution. Incomprehensive studies of the solubility of the TOPO in polystyrene, polyisoprene, polymethylmethacralate of variuos molecular weight have shown that solutions of the polymers turn opaque upon the addition of nanocrystals even at fairly low concentrations (typically 2% by volume polymer in toluene, 0.2mol/l CdSe in toluene, at a ratio of 4:1). Evidence of the aggregation has been observed by TEM microscopy (see Fig. D.1).

Two approaches have been explored to increase the solubility of the nanocrystals in polymers. The first involves the addition of end functionalized oligomers which have a head group such as a Lewis base which coordinates effectively to the nanocrystal surface, and a long tail which is similar to the chemical character of the polymer. The other is using polymers which themselves have groups that form favorable interactions with the nanocrystal surface.

An increase of the solubility of TOPO capped nanocrystals in a solution of polystyrene was obtained by using three different end functionalized oligomers, two of which had an amine group (P62NH2 Mn2600, and P1211-NH2 Mn 1700 Polymer Source Inc.) and one which was thiol terminated (Fetters Mn 1300). The solution of CdSe nanocrystals in polystyrene was optically clear vs. a very cloudy solution obtained when the compatibilizers were not added. The most favorable solubility results were obtained using the P62NH2[1].

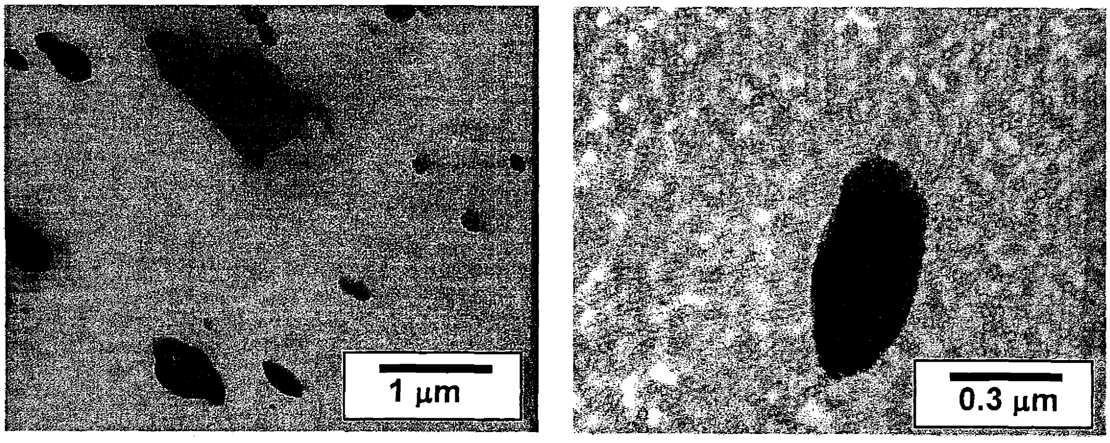

Figure D.1 A bright field TEM micrograph of CdSe nanocrystals aggregates in an cylindrical morphology poly(styrene-b-butadiene-styrene) triblock copolymer with no end functionalized oligomer added.

The sample in Fig. D.1 was prepared by adding 2ml of CdSe nanocrystals (0.078mol/l) in toluene to 0.7g of poly(styrene-b-butadiene-styrene) triblock copolymer (DOW 8550-D). The solution was stirred for 12h and roll cast at 40RPM, upon casting the solution turned opaque. The sample was then cryo microtomed and stained in OsO_4. Large aggregates are evident in the TEM micrograph as well as the cylindrical morphology of the block copolymer. This should be contrasted with Fig. 3.5 and 3.9 showing the nanocrystals incorporated into the block copolymer structure.

---

[1] The solubility was compared by adding equimolar amounts of the end-functionalized oligomers to a fixed amount of TOPO capped CdSe in toluene, and comparing the optical transparency upon solvent removal.

E. PPV thickness calibration protocol

The calibration curve for the converted PPV thickness as a function of the number of bilayers is presented in Fig. E.1. The PAA-pPPV bilayers were deposited on a silicon substrate which was cleaned by immersion in a chromerge solution. The thickness of the converted film was measured on a P10 Tencor profilometer and a Geartner ellipsometer. The value of the index of refraction was fitted such that the calculated value of the intensity equaled the measured. The thickness for the value of the index of refraction (1.85-0.015i) varied from the profilometer

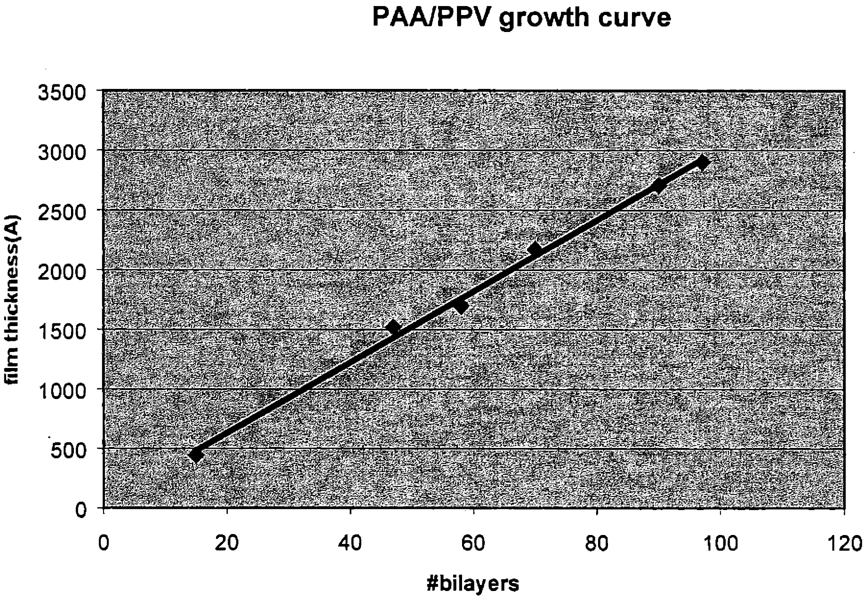

Figure E.1 Thickness calibration curve for PPV/PAA bilayers after conversion.

F. Band calculations for common block copolymer systems with realistic dielectric contrast.

F.1 Band calculation for 2D PS/PI like system.

Figures F.1 and F.2 represent the photonic band structure for a triangular array of PS cylinders in a PI matrix. The volume of the minority phase is taken to be 29%, and the indices of refraction are $n_{cylinders} / n_{matrix} = 1.59 / 1.51$.

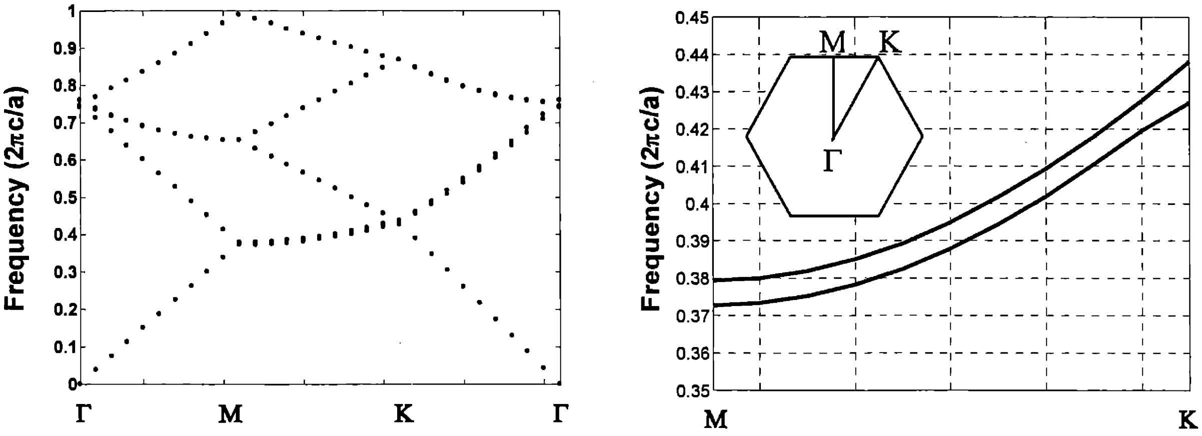

Figure F.1 TM mode photonic band structure for cylinders on hexagonal lattice with r/a=0.29 and $n_{cylinders} / n_{matrix} = 1.59 / 1.51$

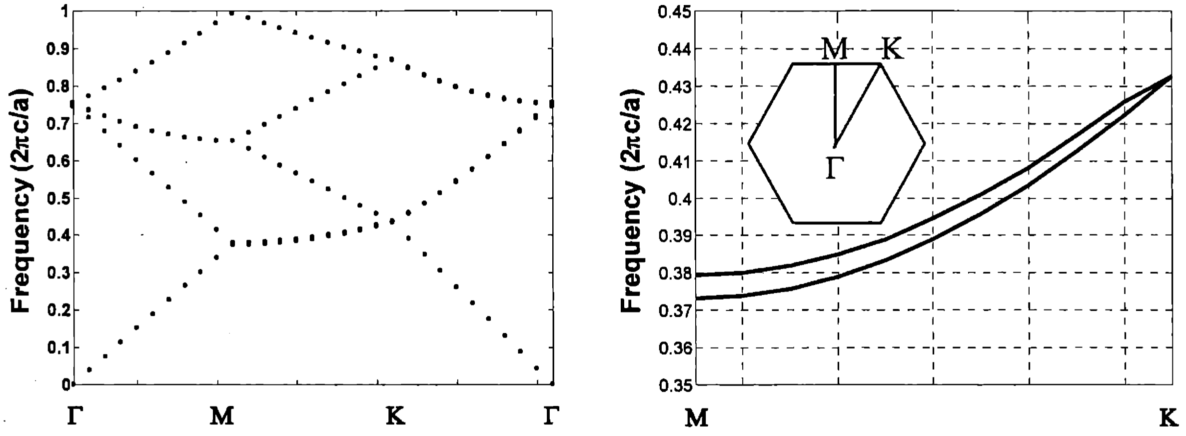

Figure F.2 TE mode photonic band structure for cylinders on hexagonal lattice with r/a=0.29 and $n_{cylinders} / n_{matrix} = 1.59 / 1.51$

The photonic band structure for the two independent electromagnetic modes (TM and TE) are presented on the left of Fig. F.1 and F.2 on the right is an enlarged view of the band structure in the M-K directions.

The directions in the reduced Brillouin zone are presented in the enlarged figures.

F.2 Extent of gap as a function of dielectric contrast.

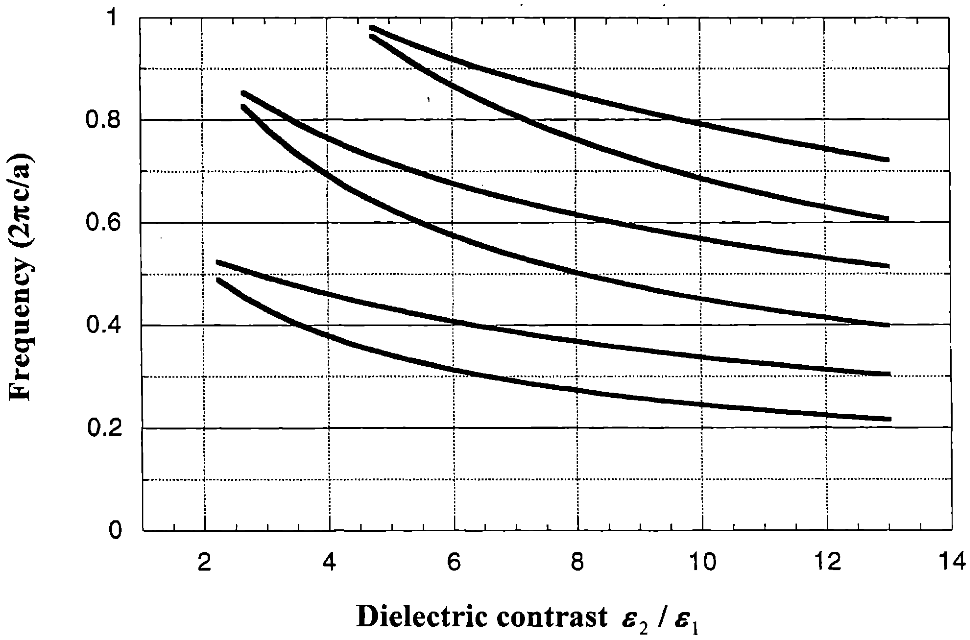

F.3 The TM gap as a function of dielectric contrast for an r/a value of 0.3.

In Fig. F.3 the extent of the TM gap for a triangular array of high dielectric cylinders in a low dielectric matrix is plotted for as a function of the dielectric ratio of the cylinders to the matrix. The first band open at a value of the dielectric ratio that is slightly higher than 2 corresponding to an index ratio of $\sqrt{2}$, a value which is definitely within the range of a polymer/air structure (i.e a polymeric structure with the columns etched out)

G. Block copolymer photonic crystals: Research road map

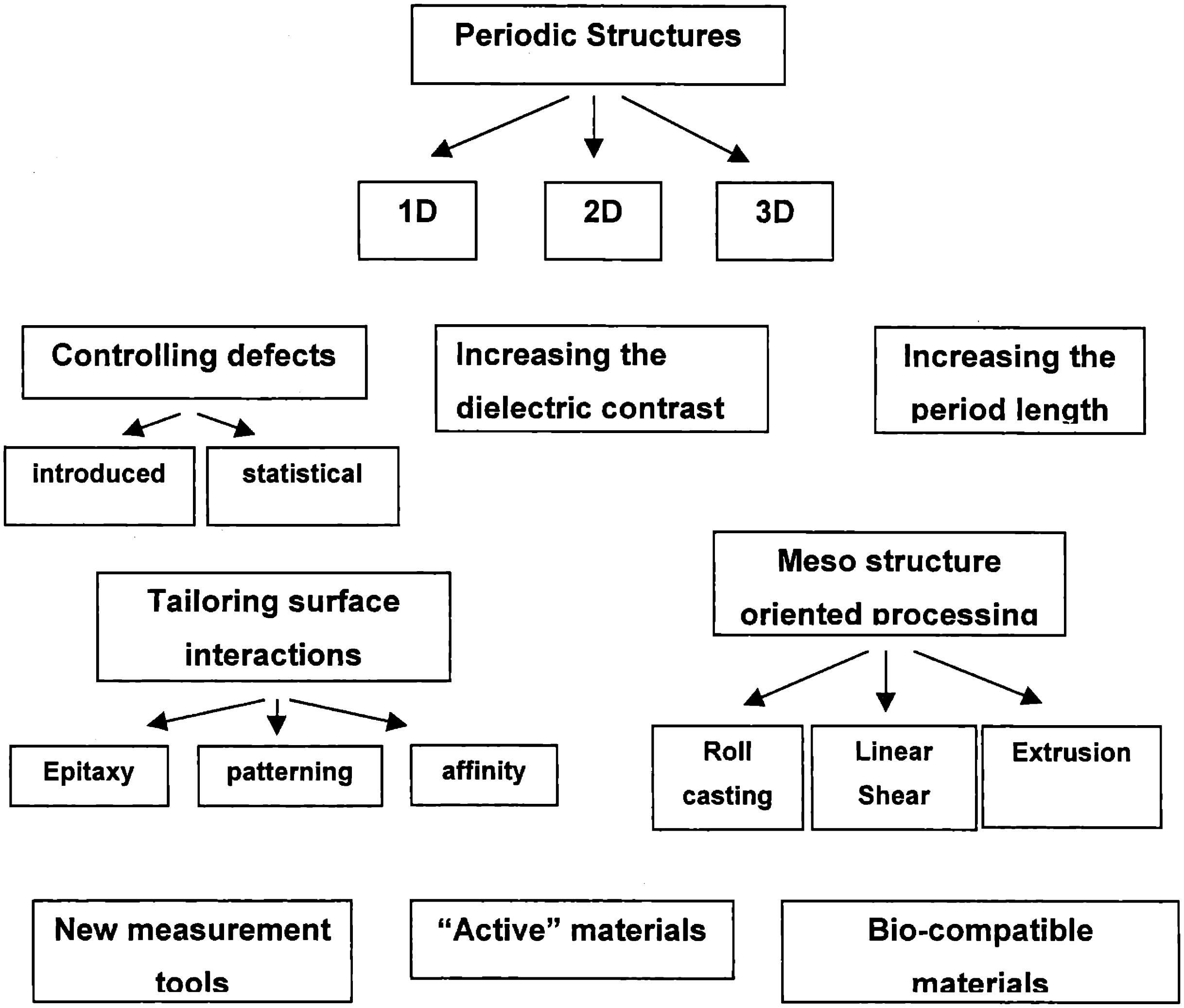

H. Future projects and applications

1. developing edible and bio-compatible PBG's for edible dye-less colorants (see Fink *et al* provisional patent application).
2. Controlling emissivity through omnidirectional coatings.
3. Providing methods for spatially and temporally electromagnetically actuated controlled release of chemicals (see Fink *et al* provisional patent application).
4. Patterning the surface via silane chemistry for control of surface affinity.
5. Self assembled optical circuits via surface patterning and control of affinity as well as epitaxy.
6. Incorporating high index materials into the structures either in the form of blends, or actually designing block copolymers with high index blocks such as conjugated polymers.

Bibliography

1. Abeles, F., Ann. De Physique **5,** 706 (1950).
2. Abromowitz, M., Stegun, I. A., "*Handbook of Mathematical Functions*", 9th Ed., Dover, New York
3. Albalak, R. J., Thomas, E. L., "Microphase separation of block copolymer solutions in a flow field", J. Poly. Sci. **31,** 37-46 (1993).
4. Becker H, Burns SE, Tessler N, Friend RH, "Role of optical properties of metallic mirrors in microcavity structures", J. App. Phys. 81, 2825-2829, (1997).
5. Becker H, Wilkinson TD, Friend RH, "Resonance wavelength-tunable microcavities" Adv. Matl. **9**, 9-14, (1999).
6. Born, M., Wolf, E., *Principles of Optics 6th* ed., 67 (Pergamon Press, sixth edition, 1980).
7. Breiner, U., Krappe, U., Thomas, E. L., Stadler, R., "Structural characterization of the 'Knitting Pattern' in SEBM triblock copolymers", Macromolecules **31,** 135-141 (1998).
8. Burns SE, Denton G, Tessler N, Stevens MA, Cacialli F, Friend RH, "High finesse organic microcavities", Opt. Matl **9**, 18-24 (1998).
9. Burns SE, Pfeffer N, Gruner J, Neher D, Friend RH, "Microcavity optical mode structure measurements via absorption and emission of polymer thin films", Syn. Met. **84**, 887-888, (1997).
10. Chan, V. Z-H., Hoffman, J., Lee, V. Y., Iatrou, H., Avgeropoulos, A., Hadjichristidis, N, Miller, R. D., Thomas, E. L., "3-D Ceramic nanostructures from silicon containing block copolymers", Science, **286**, 1716-1719 (1999).
11. Chen, J. T., Thomas, E. L., Ober, C. K., Mao, G.-P , "Self assembled smectic phases in rod-Coil block copolymers", Science **273,** 343-346 (1996).
12. Chigrin, D.N., Lavvrinenko, A.V., Yarotsky, D.A., Gaponenko, S.V., "Observation of total omnidirectional refelction from a one-dimensional dielectric lattice", Appl. Phy. A, **68**, 25-28 (1999).
13. Cohen-Tannoudji, C., Diu, B., Laloe, F., "*Quantum Mechanics*", John Wiley (1977).
14. Cleave V, Yahioglu G, Le Barny P, Friend RH, Tessler N, "Harvesting singlet and triplet energy in polymer LEDs", Adv. Matl. **11**, 285-288, (1999).
15. Croitoru, N., Dror, J., Gannot, I., "Characterization of hollow fibers for the transmission of infrared radiation," Appl. Opt. **29,** 1805-1809 (1990).
16. Dabbousi, B. O., Rodriguez-Viejo, J., Mikulec, F. V., Heine, J. R., Mattoussi, H. , Ober, R., Jensen, K. F., Bawendi, M. G., "(CdSe)ZnS core-shell quantum dots: synthesis and characterization of a size series of highly luminescent nanocrystallites", J. of Phys. Chem. B **101**, no.46, 9463-9475 (1997).
17. Díaz-García, M. A., Hide, F., Schwartz B. J., McGehee, M. D., Andersson, M. R., Heeger, A. J., "Plastic" lasers: Comparison of gain narrowing with a soluble semiconducting polymer in waveguides and microcavities", App. Phys. Lett., **70**, 24 3191-3193 , (1997).
18. Dodgson, C. L., "*Through the Looking Glass*", (1871).
19. Drexhage, K. H., "*Progress in Optics*", E. Wolf ed., **7**, p165, North Holland, Amsterdam (1974).

20. Drexhage, K. H., "*Progress in Optics*", E. Wolf ed., **7**, p165, North Holland, Amsterdam (1974).
21. Fasolka, M. , Harris, D. J. , Mayes, A. M., Yoon, M., Mochrie, S. G. J., " Observed substrate topography-mediated lateral patterning of diblock copolymer films" Phy. Rev. Lett. **79**, 3018-3021(1997).
22. Fink, Y., Winn, J. N., Fan, S., Chen, C., Michel, J., Joannopoulos, J. D., Thomas, E. L., "A dielectric omnidirectional reflector", Science **282,** 1679-1682 (1998).
23. Fink, Y., Ripin, D. J, Fan, S., Chen, C., Joannopoulos, J. D., Thomas, E. L., "Guiding Optical Light in Air Using an All-Dielectric Structure", J. Lightwave Technology, **17,** 11, 2039-2041, (1999).
24. Fink, Y., Urbas, A. M., Bawendi, M. G., Joannopoulos, J. D., Thomas, E. L., "Block Copolymers as Photonic Band Gap Materials", J. Lightwave Technology, **17,** 11, 1963-1969, (1999).
25. Fink, Y., Ibanescu, M., Thomas, E. L., Joannopoulos, J. D., "All dielectric coaxial waveguide – The Coaxial OmniGuide", provisional patent filing (April 1999).
26. Fink, Y., Joannopoulos, J. D., Thomas, E. L., "A biocompatible photonic bandgap material", MIT case 8412 (March 1999).
27. Fink, Y., Fan, S., Chen, C., Thomas, E. L., Joannopoulos, J. D., "Omnidirectional multilayer coating for enhanced optical waveguiding: The Omniguide", MIT case 8249.
28. Fink, Y., Thomas, E. L., "Polymeric photonic band pap materials", MIT case 7532 PCT/US98/02974.
29. Fink, Y., Winn, J. N, Fan, S., Joannopoulos, J. D., "An omnidirectional 1D photonic crystal", MIT case 7953.
30. Fink, Y., Winn, J. N., Fan, S., Chen, C., Joannopoulos, J. D., Thomas, E. L.,"A polymer-inorganic multilayer film", MIT case 8005.
31. Fogg, D. E., Radzilowski, L. H., Dabbousi, B. O., Schrock, R. R., Thomas, E. L., Bawendi, M. G.,"Fabrication of quantum dot-polymer composites: semiconductor nanoclusters in dual function polymer matrices with electron-transporting and cluster-passivating properties", Macromolecules **30**, 8433-8439 (1997).
32. Friend, R. H., Gymer, R. W., Holmes, A. B., Burroughes, J. H., Marks, R. N., Taliani, C., Bradley, D. D. C., Dos Santos, D. A., Bredas, J. L., Logdlund, M., Salaneck, W. R., "Electroluminescence in conjugated polymers", Nature **397**, 121-128, (1999).
33. Granlund, T., Theander, M., Berggren, M,. Andersson, M., Ruzeckas, A., Sundstrom, V., Bjork, G., Granstrom, M., Inganas, O., "A polythiophene microcavity laser" Chem. Phys. Lett. **288,** 879-884 (1998).
34. Ho, P. K. H., Thomas, D. S., Friend, R. H., Tessler, N., "All-polymer optoelectronic devices", Science **285**, 233-236, (1999).
35. Honeker, C. C. , Thomas, E. L. , "Impact of morphological orientation in determining mechanical properties in triblock copolymer systems", Chem. of Materials, **8,** 1702-1714 (1996).
36. Jenekhe, S. A., Chen, X. L., "Self-assembly of ordered microporous materials from rod-coil block copolymers", Science **283,** 372-375 (1999).
37. Joannopoulos, J.D., Meade, R., Winn, J.N., *Photonic Crystals: Molding the Flow of Light*. (Princeton Press, Princeton, NJ, 1995).
38. John, S., Phys. Rev Lett. **58**, 2486 (1987).

39. Martín-Moreno, L., García-Vidal, F. J., Somoza, A. M., "Self-Assembled Triply Periodic Minimal Surfaces as Molds for Photonic Band Gap Materials", Phys. Rev. Lett. **83**, pp. 73-75 (1999).
40. Matsuura, Y., Harrington, J., "Hollow glass waveguides with three-layer dielectric coating fabricated by chemical vapor deposition" J. Opt. Soc. Am. **14,** no. 6 (1997).
41. McGehee, M. D, Díaz-García, M. A., Hide, F., Gupta, R., Miller, E. K., Moses, D., Heeger, A. J., "Semiconducting polymer distributed feedback lasers", App. Phys. Lett., **72,** 13 1536-1538 , (1998).
42. Meade, R., Brommer, K., Rappe, A., Joannopoulos, J. D., "Existence of a photonic band gap in two dimensions", Appl. Phys. Lett. **61**, 495-497 (1992).
43. Mekis, A., Chen, J. C., Kurland, I., Fan, S., Villeneuve, P. R., Joannopoulos, J. D., " High transmission through sharp bends in photonic crystal waveguides", Phys. Rev. Lett. **77**, 3787-3790 (1996).
44. Mie, G., Ann. D. Physik (4), **25** 377 (1908).
45. Miyagi, M., Hongo, A., Aizawa, Y., Kawakami, S., "Fabrication of germanium-coated nickel hollow waveguides for infrared transmission," Appl. Phys. Lett. **43,** 430-432 (1983).
46. Miyagi, M., Kawakami, S., "Design theory of dielectric coated circular metallic waveguides for infrared transmission", J. Lightwave Technol. LT-2, 116-126 (1984).
47. Murray, C. B., Norris, D. J., Bawendi, M. G., "Synthesis and characterization of nearly monodisperse CdE (E = S, Se, Te) semiconductor nanocrystallites." J. Am. Chem. Soc. **115**, 8706 (1993).
48. Palik, E. D., "Handbook of optical constants of solids", Academic Press (1998).
49. Prasman, E., Thomas, E. L., "High strain tensile deformation of a sphere forming triblock copolymer-mineral oil blend", J. Poly. Sci. **42,** 1625-1636 (1998).
50. Robertson, W. M., Arjavalingam, G., Meade, R. D., Brommer, K.D., Rappe, A. M., Joannopoulos, J. D., "Measurement of photonic band structure in a two-dimensional periodic dielectric array", Phys. Rev. Lett., **68,** 2023-2026 (1992).
51. Russell, P.S.J., Tredwell, S., Roberts, P. J., "Full photonic bandgaps and spontaneous emission control in 1D multilayer dielectric structures", Opt Comm., **160**, (1-3) 66-71 (1999).
52. Skoulios, A. E., "Organizational and structural problems in block and graft copolymers", Block and graft copolymers conference proceedings, Sagamore Army Materials Research Conference, 19th, Raquette Lake, N.Y (1972).
53. Shibayama, M., Hashimoto, T., Hasegawa, H., "Ordered structure in block copolymer solutions 3. Concentration dependence of microdomains in nonselective solvents", Macromolecules **16,** 9, 1427-1433, (1983).
54. Tessler N, Denton GJ, Friend RH, "Lasing characteristics of PPV microcavities" Syn. Met. **84**, 475-476, (1997).
55. Tessler, N., Denton, G. J., Friend R. H., "Lasing from conjugated polymer microcavities", Nature **382,** 695-697 (1996).
56. Tessler, N., "Lasers based on semiconducting organic materials", Adv. Mat. **11,** no. 5, 363-370, (1999).
57. Tessler, N., Friend, R. H., "Polymer LEDs as laser media ?" Synthetic Metals **102,** 1122-1123, (1999).

58. Thomas, E. L., Lescanec, R. L., "Phase morphology in block copolymer systems", Phil. Trans. R. Soc., London, A **348**, 149-166 (1994).
59. Urbas, A. M., Fink, Y., Thomas, E. L., "Self assembled one dimensionally periodic dielectric reflectors from block copolymer-homopolymer blends" Macromolecules **32,** 4748-4750 (1999).
60. Villeneuve, P. R., Fan, S., Joannopoulos, J. D., "Microcavities in photonic crystals: mode symmetry, tunability, and coupling efficiency ", Phys. Rev. B **54**, 7837-7842 (1996).
61. Winey, K. I., Thomas, E. L., Fetters, L. J., "Swelling a lamellar diblock copolymer by homopolymer concentration and molecular weight", Macromolecules, **24,** 6182-6188 (1991).
62. Wijnhoven, J., Voss, W. L., "Preparation of photonic crystals made of air spheres in titania ", Science **281**, 802 (1998).
63. Winn, J. N., Fink, Y., Fan, S., Joannopoulos, J. D., "Omnidirectional reflection from a one-dimensional photonic crystal", Optics Letters **23,** No. 20, 1573-1575 (1998).
64. Yablonovitch, E. , Phys Rev Lett. **58,** 2059 (1987).
65. Yariv, A., "*Optical Electronics*", 3ed Holt, Rinehart and Winston (1985).
66. Yeh, P., Yariv, A. Hong, C-H., J. Opt. Soc. Am. **67** no. 4, 423 (1977).
67. Yeh, P., Yariv, A., Marom, E., "Theory of a bragg fiber", J. Opt. Soc. Am., **68** vol. 9, (1978).